Fermi National Accelerator Laboratory

FERMILAB-Conf-92/103

$\bar{P}P$ Collider Physics

M. Demarteau

State University of New York at Stony Brook
Stony Brook, NY 11794

Fermi National Accelerator Laboratory
P.O. Box 500, Batavia, Illinois 60510

April 1992

Lectures given at the *1991 Joint Belgian - Dutch - German (Aachen) School of Particle Physics,* Aachen, Germany, September 9 - 20, 1991.

Operated by Universities Research Association Inc. under Contract No. DE-AC02-76CHO3000 with the United States Department of Energy

Disclaimer

$\bar{P}P$ COLLIDER PHYSICS *

Marcel Demarteau
State University of New York at Stony Brook
Stony Brook, NY 11794

*Lectures given at the 1991 Joint Belgian - Dutch - German (Aachen) School of Particle Physics, Aachen, Germany, September 9 - 20, 1991

Contents

$\bar{P}P$ COLLIDER PHYSICS

Abstract

A brief introduction to $\bar{p}p$ collider physics is given. Selected results from the collider experiments at the CERN S$\bar{p}p$S and the Tevatron collider are described. The emphasis is on experimental aspects of $\bar{p}p$ collisions. Minimum bias physics and the production of jets, Intermediate Vector Bosons and heavy flavors is reviewed. The outlook for physics at hadron colliders for the near future is briefly discussed.

1 Introduction

Collider experiments will most likely evolve along two major "frontiers", the "high precision frontier" and the "high energy frontier". The high precision approach is the line pursued today by LEP, SLC and other machines and in future will require dedicated particle-factories. Barring any major breakthrough in accelerator technology, the second, complementary approach, will be the domain of hadron colliders. Hadron colliders will be the machines that will have the unique opportunity to probe the fundamental interactions at the shortest possible length scale, to look for new massive particles predicted by current theoretical models and to look for deviations from the expected behavior. A window on the high energy behavior of particle interactions will be provided, most likely exclusively, by collider experiments at hadron colliders which underlines the importance of the physics at hadron colliders.

The objective of these lectures was to discuss some experimental aspects of physics at hadron colliders. Obviously, only some selected topics of the extensive physics program of the collider experiments could be covered. For other aspects of the material discussed here and for complementary information the reader is referred to many excellent reviews. In the lecture notes from the CERN Schools of Physics, the Cargèse and SLAC Summer Institutes on Particle Physics and the Advanced

Study Institute on techniques and concepts of high energy physics many superb reviews can be found on almost any aspect of particle physics.

In these notes first low momentum transfer processes will be described briefly. Then the physics of large momentum transfer processes will be addressed. The latter part comprises jet physics and QCD, Intermediate Vector Boson and heavy flavor production.

2 $\bar{p}p$ Collisions and Experiments

Most $\bar{p}p$ interactions involve low momentum transfers between the constituents. In these soft processes the partons interact collectively producing many particles with low transverse momentum, p_t, with respect to the incoming (anti-)proton direction. These soft processes cannot be described by perturbative Quantum Chromodynamics (QCD) and phenomenological models are used to describe the interactions. Sometimes, actually very rarely compared to the occurrence of a soft interaction, a hard scattering occurs where there is a large momentum transfer between two partons, producing particles with large p_t in the final state. Since the coupling constant of the strong interaction, α_s, becomes small at high momentum transfers, high p_t scattering is well described by perturbative QCD. One should note, though, that every hard collision is accompanied by a soft collision due to the interaction of the remaining partons in the hadron which do not participate in the hard collision (spectators). The soft collision in a hard scattering process is generally referred to as the "underlying event".

Detectors have been designed and constructed with the emphasis specifically on the study of either soft collisions or hard collisions. The experiments UA4 and UA5 at CERN and experiment E710 in the EØ interaction region at Fermilab were designed to study processes with low momentum transfer. The experiments UA1 and UA2 at CERN and CDF and DØ at Fermilab concentrate on the study of large momentum transfer processes. In the remainder of this section the experiments designed to study soft collisions will be described briefly. The discussion of the experiments for large p_t physics will be relegated to section 4.

The UA4 experiment at CERN was specifically designed to measure the $\bar{p}p$ total cross section and elastic scattering. Its counterpart at FNAL is E710 installed in the interaction region EØ. As will be clear from the discussion in the next section, a crucial aspect of the measurement of the total cross section is the measurement of the deflection of the scattered proton and anti-proton down to very small angles. With sets of mini high precision tracking chambers installed in so-called Roman pots on both sides of the interaction region the direction of the scattered proton and anti-proton is measured. The Roman pots are installed at about 35 m and 125 m on either side of the interaction point for UA4 and E710, respectively. A schematic outlay of experiment E710 is shown in figure 1.

The streamer chamber experiment UA5 (Fig. 2) has been designed to study

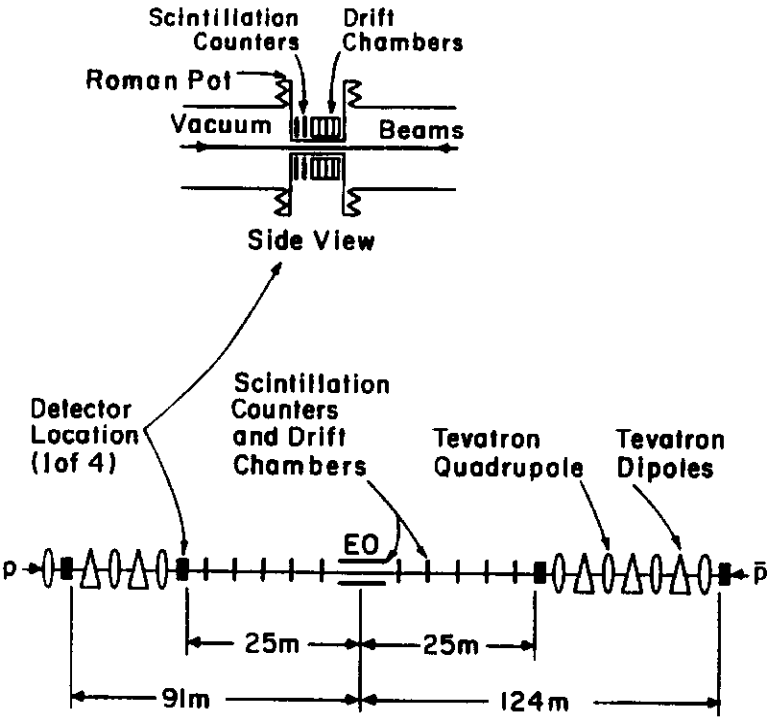

Figure 1: Schematic layout of experiment E710 and the Tevatron lattice on both sides of the EØ straight section.

characteristics of particle production in $\bar{p}p$ collisions. It essentially consists of two 6 m long streamer chambers above and below the intersection region incorporating lead-glass plates to allow for photon identification. A calorimeter segment has been added to detect neutral hadrons and to give a rough energy measurement for both charged and neutral hadrons.

3 Low Momentum Transfer Processes

3.1 Total Cross Section

The total $\bar{p}p$ cross section can be obtained by measuring simultaneously the forward elastic scattering rate at low four-momentum transfers t, and the total inelastic rate. Using the optical theorem the differential elastic rate at low t is given by

$$\frac{dN_{el}}{dt} = \mathcal{L}\,\frac{\sigma_{tot}^2(1+\rho^2)}{16\pi(\hbar c)^2}\,e^{-bt} \tag{1}$$

Here ρ is the ratio of the real to imaginary part of the forward elastic scattering amplitude, $\mathcal{L}$ the integrated machine luminosity and t the four-momentum transfer, $t = (p_1 - p_3)^2$. The slope parameter b gives the experimental parametrization of the t-dependence of the elastic rate. Obviously, the sum of the elastic and inelastic rate is also proportional to the total cross section:

$$N_{el} + N_{inel} = \mathcal{L}\,\sigma_{tot} \tag{2}$$

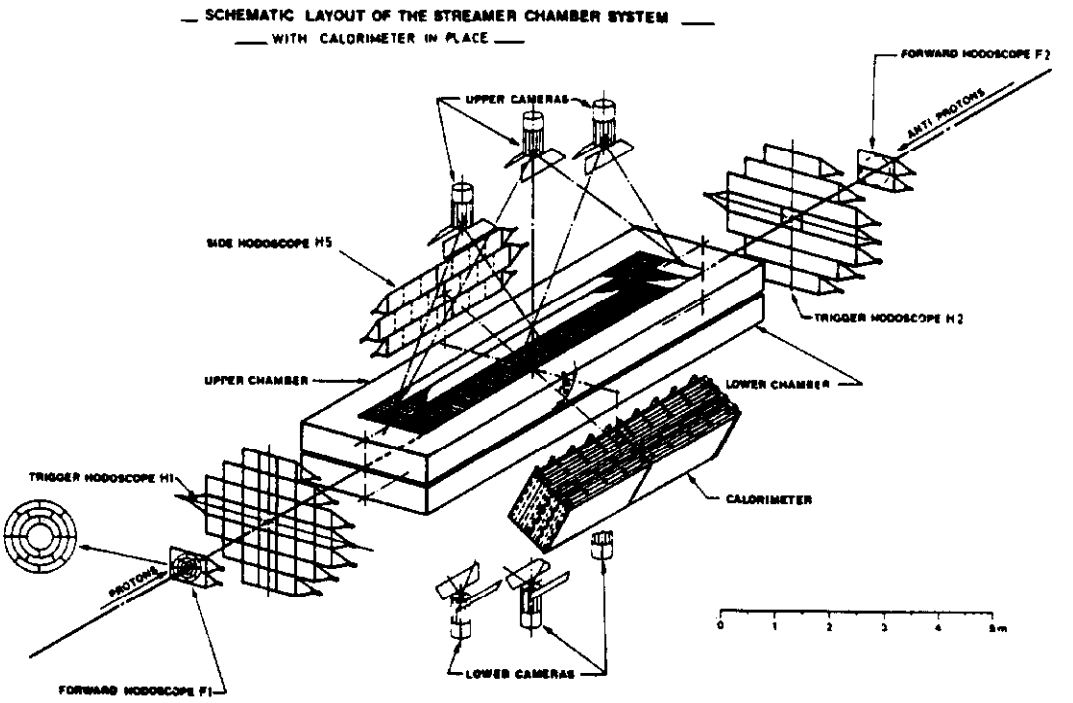

Figure 2: Schematic overview of the streamer chamber experiment UA5.

Combining expressions 1 and 2 gives

$$\sigma_{tot} = \frac{16\pi\,(\hbar c)^2}{1+\rho^2}\,\frac{dN_{el}/dt\,|_{t=0}}{N_{el}\,+\,N_{inel}} \tag{3}$$

Thus, the total cross section can be measured independently of the machine luminosity if the total elastic rate at $t = 0$ and the inelastic rate is measured simultaneously. Measuring the total elastic rate at $t = 0$ implies measuring precisely the t-dependence down to the smallest momentum transfers before reaching the Coulomb interference region and extrapolating to $t = 0$. At the Tevatron the elastic cross section is measured down to $t = -0.04\ GeV^2$, which means measuring the outgoing particles down to angles of $0.2\ mrad$ with respect to the beam line. The parameter ρ, the ratio of the real to imaginary part of the forward elastic scattering amplitude, is measured independently by extending the elastic scattering detection to smaller angles, called the Coulomb interference region, where the hadronic amplitude interferes with the Coulomb scattering. The ratio ρ as measured by UA4 and E710 is $\rho = 0.24 \pm 0.04$ [1] and $\rho = 0.140 \pm 0.069$ [2], respectively. The rather large value for ρ measured by UA4 is not readily understood in the framework of the current phenomenological models for low p_t-scattering.

The total $\bar{p}p$ cross section at a center of mass energy of $\sqrt{s} = 546\ GeV$ as measured by UA4 is $\sigma_{tot} = 61.9 \pm 1.5\ mb$ [3]. The UA5 collaboration has determined σ_{tot} at $\sqrt{s} = 900\ GeV$ from the total inelastic cross section alone by measuring the ratio of the inelastic rates at $\sqrt{s} = 200$ and $900\ GeV$ when the CERN $\bar{p}p$ collider was operated in pulsed mode. The cross section has been evaluated to be $\sigma_{tot} = 65.3 \pm 0.7 \pm 1.5\ mb$ at $\sqrt{s} = 900\ GeV$ [4]. E710 has measured the total cross

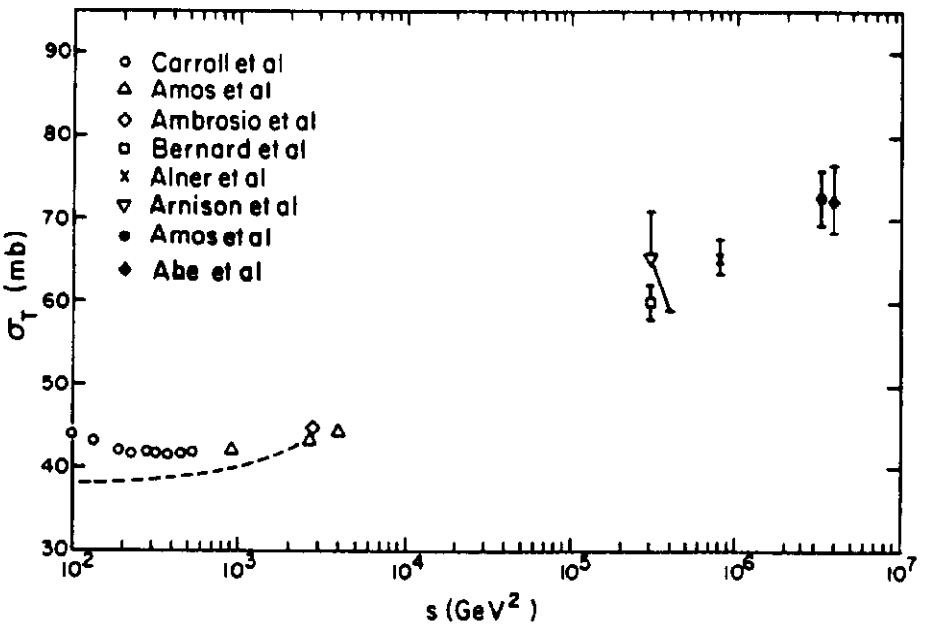

Figure 3: Total $\bar{p}p$ cross section as function of $\sqrt{s}$.

section at $\sqrt{s} = 1.8\ TeV$ to be $\sigma_{tot} = 72.1 \pm 3.3\ mb$ [5]. The CDF measurement yields a comparable value of $\sigma_{tot} = 72.0 \pm 3.6\ mb$ [6]. Figure 3 shows all the measurements of the total $\bar{p}p$ cross section as function of $\sqrt{s}$. The measurements tend to favor a $ln(s)$ dependence of the total cross section.

3.2 Minimum Bias Physics

Another topic of soft physics is the physics of minimum bias events. Ideally the study of soft collisions would be unbiased, including all types of events. In practice, though, it is necessary to apply a trigger to signal that an interaction has occurred. Events recorded with a trigger that has the least bias with respect to the event topology are called minimum bias events. Particle production in minimum bias events has been extensively studied by both UA5 and UA1. The UA1 data has been recorded when the CERN $\bar{p}p$ collider was operated in pulsed mode [14]. To minimize systematic effects the UA1 collaboration has collected the events with a low magnetic field in order to reduce the beam displacement in the center of the detector.

Since their are no real dynamical constraints in soft particle production, the distribution of particles is mainly determined by phase space. The three dimensional phase space is given by

$$\frac{d^3p}{E} = \frac{dp_x\, dp_y\, dp_z}{E} = d\varphi \frac{dp_t^2}{2} \frac{dp_z}{E}$$

Defining rapidity y as

$$y \equiv \frac{1}{2} ln \frac{E + p_L}{E - p_L} \tag{4}$$

it is straightforward to show that $dy = dp_L/E = dp_z/E$. The invariant cross section then reads

$$E\frac{d^3\sigma}{d^3p} = \frac{1}{\pi}\frac{d\sigma}{dp_t^2\,dy} \tag{5}$$

Rapidity is thus a natural phase space element.

Note that rapidity, defined in equation 4, has two limits. First there is the kinematic limit. The rapidity can be written as

$$y \equiv \frac{1}{2}ln\frac{E+p_L}{E-p_L} = ln\frac{E+p_L}{m_T} \tag{6}$$

where the transverse mass m_T is defined as $m_T = \sqrt{p_T^2 + m^2}$. The maximum longitudinal momentum a particle can obtain in a collision in the center of mass system is half the center of mass energy. The rapidity range available is thus restricted to

$$(y_{max})_{CMS} \approx \frac{1}{2}ln\frac{s}{{m_T}^2} \tag{7}$$

and rises logarithmically with s.

The second limit is the high momentum limit. When the masses of the particles can be neglected, the argument of the logarithm can be directly related to the angle ϑ the particle's momentum makes with respect to the beamline

$$y \equiv \frac{1}{2}ln\frac{E+p_L}{E-p_L} \approx \frac{1}{2}ln\frac{cos^2(\vartheta/2)}{sin^2(\vartheta/2)} = ln\,\cot(\vartheta/2) \equiv \eta \tag{8}$$

The angular variable η is called pseudorapidity. Because it involves only an angular measurement and is independent of mass, η rather than y is the variable most commonly used in $\overline{p}p$ collisions.

3.2.1 Pseudorapidity density distribution

One of the studies of particle production in minimum bias events is the measurement of the charged particle density distribution, $\rho(\eta) = dN_{ch}/d\eta$. Figure 4a shows $dN_{ch}/d\eta$ as function of pseudorapidity obtained by UA5 at ISR and $\overline{p}p$ collider energies [7]. Four features of the pseudorapidity density distribution should be noted from figure 4a. First, since rapidity is a natural phase space element, the distribution in the central region is essentially flat in this variable. Secondly, the rapidity "plateau" ends at some value η_{max} because of the kinematically limited available rapidity range. The endpoints of the rapidity plateau increase logarithmically with center of mass energy, as expected from equation 7. The last feature apparent from this figure is the rise of the value of the rapidity plateau with $\sqrt{s}$, reflecting the increase in total charged multiplicity with increasing center of mass energy. Figure 4b shows the charged particle multiplicity as measured by CDF [8], compared to the UA5 measurement. CDF does not see the falloff at the kinematic limit, since their

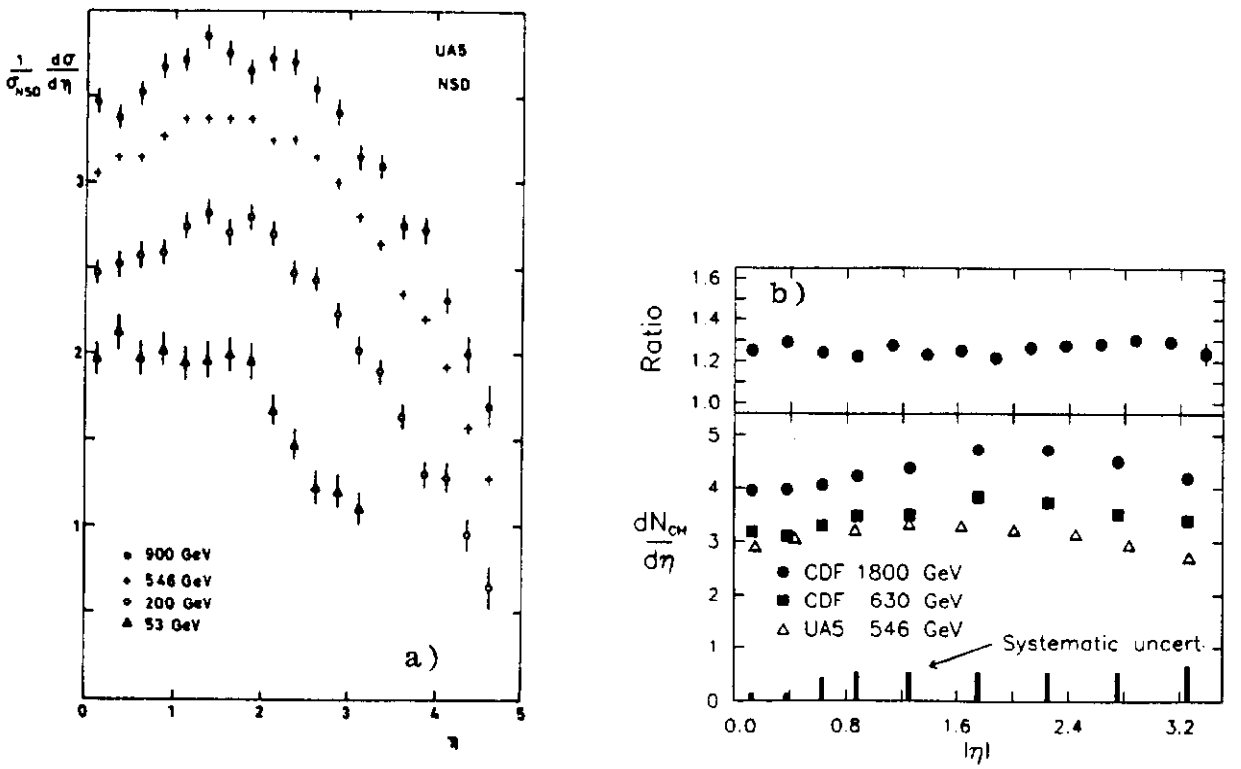

Figure 4: (a) Pseudorapidity density distributions obtained by UA5 at various center of mass energies for non-single-diffractive events. (b) $dN_{ch}/d\eta$ as function of η in minimum bias events as measured by CDF. The upper half of the figure shows the ratio of $dN_{ch}/d\eta$ at $\sqrt{s} = 1.8\ TeV$ to that at $\sqrt{s} = 0.63\ TeV$.

tracking chambers do not extend to small enough angles. The ratio of $dN_{ch}/d\eta$ at $\sqrt{s} = 1800\ GeV$ to that at $\sqrt{s} = 630\ GeV$ is shown in the upper half of the figure. It is expected that most of the systematic errors, indicated along the lower edge of the plot, cancel in taking the ratio. The dependence on $\sqrt{s}$ of the multiplicity density distribution at $\eta = 0$, $(dN_{ch}/d\eta)_{\eta=0}$, is shown in figure 5 [9]. A fit by UA5 to a $ln(s)$ energy dependence yields $\rho(0) = (0.01 \pm 0.14) + (0.22 \pm 0.02)\, ln(s)$. The fit is shown as the dashed line in the figure. The data from CDF seems to favor a $ln^2(s)$ dependence of the charged particle pseudorapidity density distribution at $\eta = 0$. However, due to the relatively large systematic errors on the CDF measurement this result is not conclusive.

Integrating the multiplicity density distribution yields the total charged multiplicity in the event. Figure 6 shows the dependence of the average charged multiplicity in inelastic events versus center of mass energy as measured by UA5 [9]. The solid curve is the result of a $ln^2(s)$ fit to the data and yields $\langle N_{ch} \rangle = 2.99 - 0.23\, ln(s) + 0.168\, ln^2(s)$. The $ln^2(s)$ dependence is readily understood from the energy dependence of the pseudorapidity density distribution at $\eta = 0$ and the kinematically allowed pseudorapidity range. The total charged multiplicity in an event is the area under the charged particle density distribution: $N_{ch} = \int (dN_{ch}/d\eta)\, d\eta$ (cf. figure 4). Since the density distribution is essentially flat, the area is simply the product of the charged particle density distribution at $\eta = 0$, $(dN_{ch}/d\eta)_{\eta=0}$, and

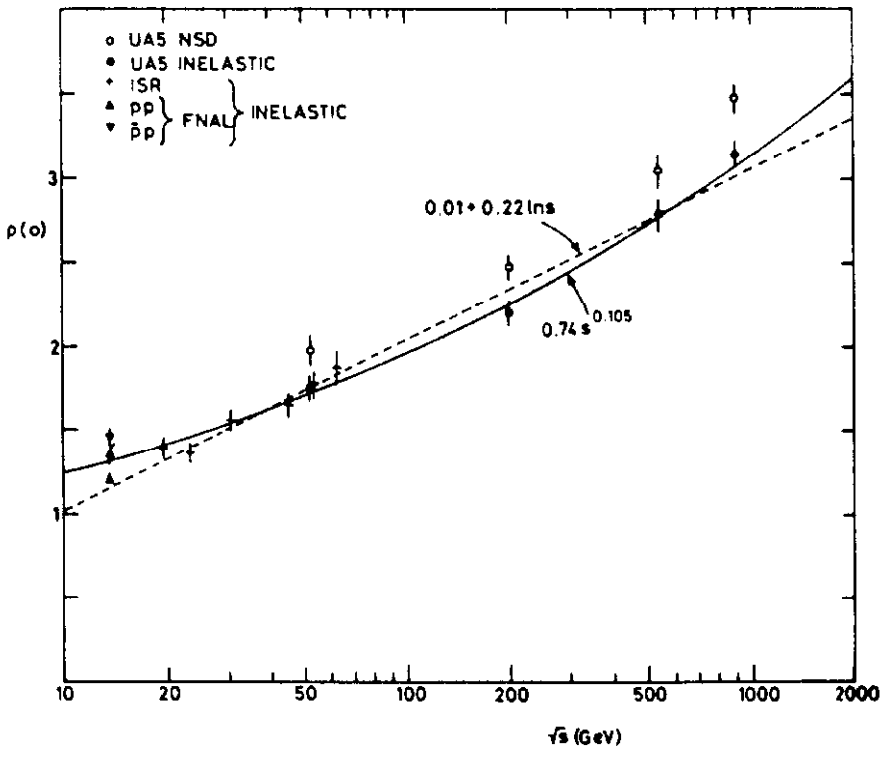

Figure 5: $dN_{ch}/d\eta$ at $\eta = 0$ versus center of mass energy

the pseudorapidity endpoint of the distribution, both of which have a $ln(s)$ energy dependence.

The physics of soft collisions, also called $ln(s)$ physics, is an essential part of $\overline{p}p$ collider physics. Besides providing insight in low momentum transfer processes, this physics is extremely important from an experimental point of view. Even though, in general, experiments interested in large p_t physics do not trigger on soft collisions, the experimental devices are still exposed to the soft interactions and one needs a way of extrapolating the characteristics of soft collisions to higher energies. Suppose one is designing, for example, a conventional wire chamber for an SSC experiment which has to operate at a center of mass energy of $\sqrt{s} = 40\ TeV$ at a luminosity of $\mathcal{L} = 10^{33} cm^{-2} s^{-1}$. An important parameter with regard to the lifetime of the chamber is the amount of charge the chamber will collect over a given period of time. Using the energy dependencies given above, one can readily show that for this particular example the device would be exposed to an average of $\sim 3\ 10^{17}$ charged particles during one year of running, an integrated charge very close to one Coulomb.

3.2.2 Single particle p_t spectrum

The transverse momentum spectrum for unidentified charged hadrons in minimum bias events measured at different center of mass energies is shown in figure 7a [10, 11, 12, 13]. As can be seen, for higher center of mass energies there are non-exponential tails at high transverse momenta which indicate the onset of hard scat-

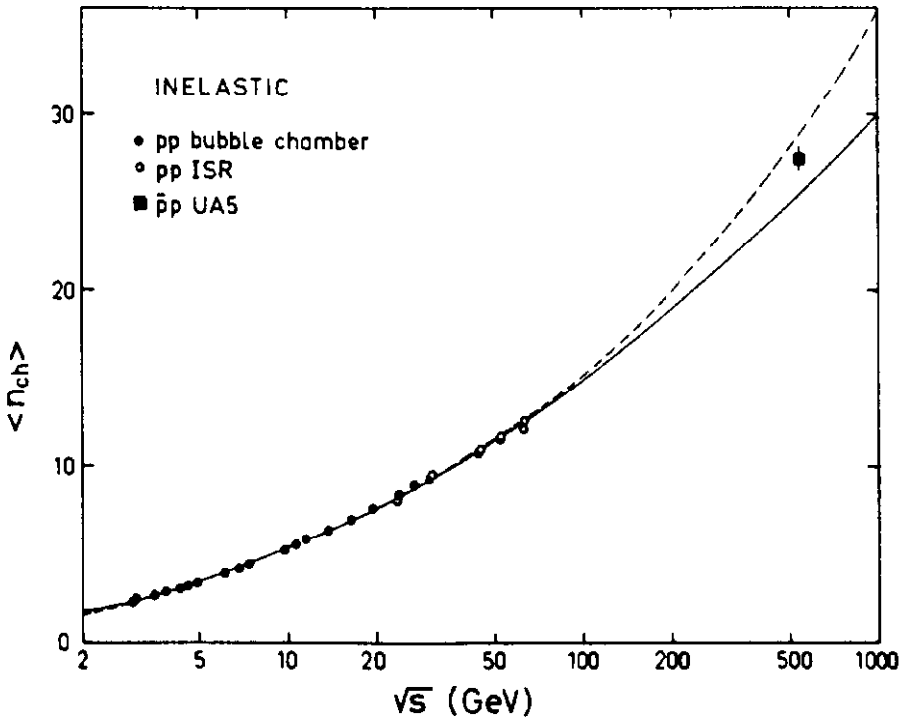

Figure 6: Average number of charged particles $\langle N_{ch} \rangle$ in inelastic events versus center of mass energy as measured by UA5.

tering contributing to the cross section. A power law of the form

$$E \frac{d^3\sigma}{d^3p} = \frac{A\, p_0^n}{(p_t + p_0)^n} \tag{9}$$

is fitted to the invariant cross section as function of p_t, where the power law is reminiscent of Rutherford scattering. At a center of mass energy of 1.8 TeV CDF obtains for these parameters, $A = 0.45 \pm 0.01$, $p_0 = 1.29 \pm 0.02$ and $n = 8.26 \pm 0.07$, resulting in an average p_t in minimum bias event of $\langle p_t \rangle = 0.495 \pm 0.014$ GeV/c [10]. The energy dependence of $\langle p_t \rangle$ is shown in figure 8a [14]. The data, spanning an energy range from 25 GeV to 1800 GeV, is well fitted with a quadratic logarithmic law of the form $\langle p_t \rangle = 0.40 - 0.030\, ln(\sqrt{s}) + 0.0053\, ln^2(\sqrt{s})$.

It is instructive to extrapolate again the observed energy dependence to higher energies, as was done in the previous section. At LHC center of mass energies of 20 TeV, for example, the average charged particle transverse momentum is $\langle p_t \rangle = 0.62$ GeV/c. Assuming a charged particle multiplicity at zero rapidity $(dN_{ch}/d\eta)_{\eta=0}$ of 6.57, the average transverse energy deposited in the detector by minimum bias events in a pseudorapidity range of $|\eta| < 3$ will be 24 GeV.

The correlation between the average charged particle transverse momentum and the multiplicity of the event is shown in figure 7b. Plotted is the invariant cross section obtained by UA1 at $\sqrt{s} = 0.9$ TeV for three different ranges of multiplicity, $dN_{ch}/d\eta = 0.8 - 4$, $dN_{ch}/d\eta = 4 - 8$ and $dN_{ch}/d\eta > 8$, all measured at

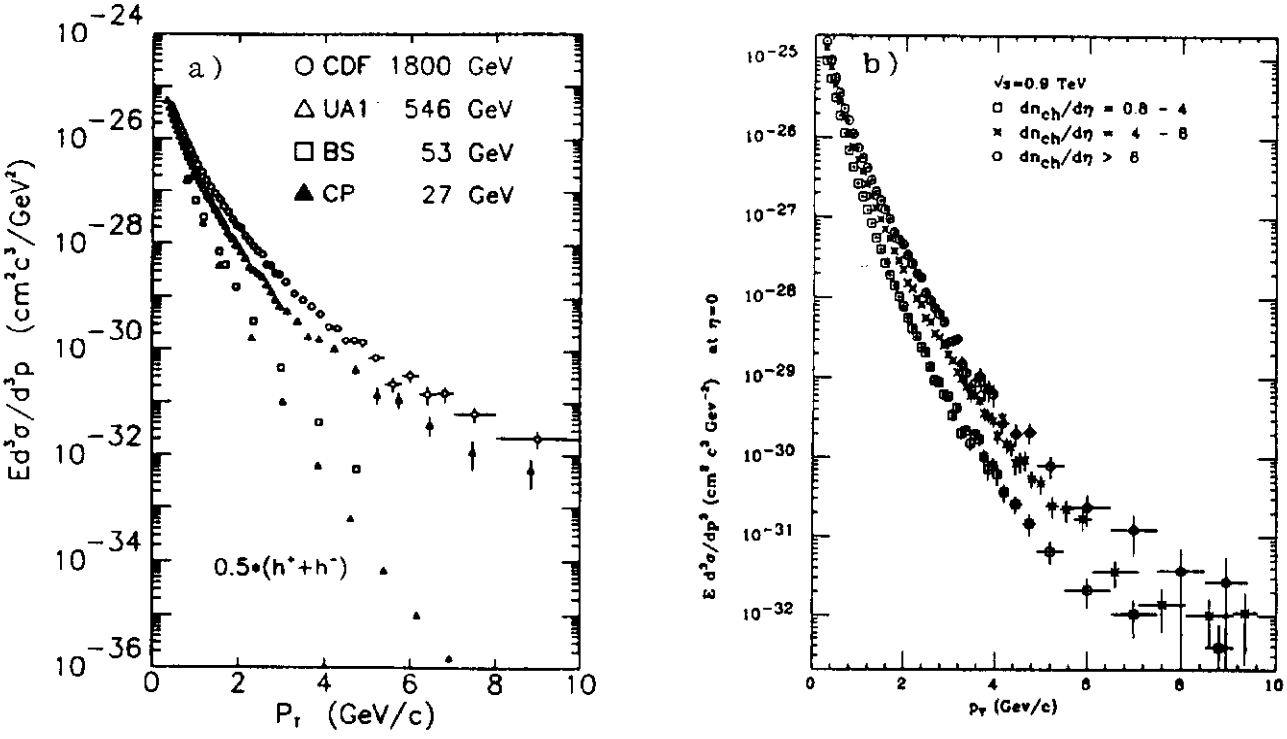

Figure 7: (a) Single charged particle invariant differential cross section $Ed^3\sigma/d^3p$ as function of p_t as measured by CDF, UA1, the British-Scandinavian and the Chicago-Princeton collaboration. (b) Single charged particle invariant differential cross section at $\eta = 0$ for different ranges of multiplicity at $\sqrt{s} = 0.9\ TeV$ as measured by UA1. The curves are normalized to the same value at $p_t = 0.2\ GeV/c$.

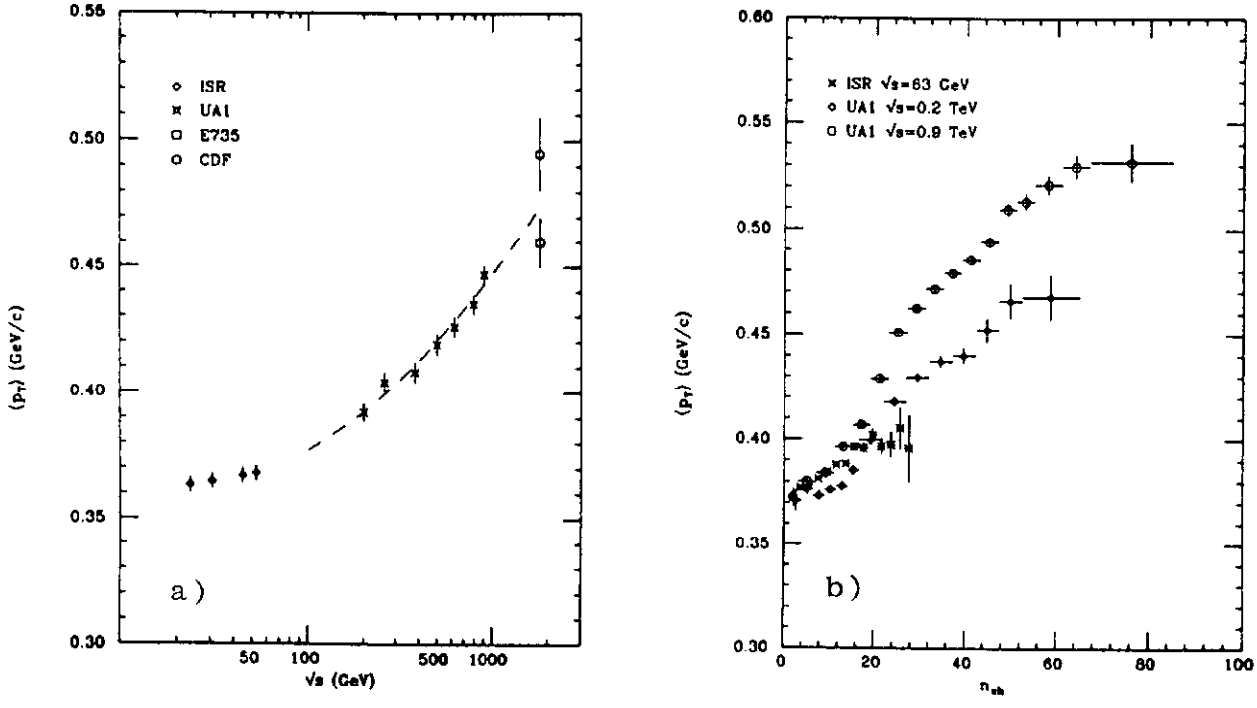

Figure 8: (a) Dependence of $\langle p_t \rangle$ of charged particles in minimum bias events on the center of mass energy. (b) $\langle p_t \rangle$ as function of the charged particle multiplicity.

$\eta = 0$ [14]. It is clear that the average p_t increases with increasing multiplicity. Figure 8b shows this correlation for three different center of mass energies as measured by UA1 at $\sqrt{s} = 0.2$ and $0.9\ TeV$ [14] and by the Split Field Magnet at the ISR at $\sqrt{s} = 63\ GeV$ [15]. For low multiplicities the average p_t is the same over a large variation of center of mass energies. For higher multiplicities there is a clear dependence on the center of mass energy. This behavior could be attributed to a phase transition to a quark-gluon plasma [16, 17].

4 Detectors for Large Momentum Transfer Processes

Because of the very different event characteristics of large momentum transfer processes, dedicated detectors have been built to study high p_t interactions. Two collider detectors were built for each of the two high energy $\bar{p}p$ colliders: the UA1 and UA2 detectors at the CERN S$\bar{p}p$S collider, and the CDF and DØ detector at the Fermilab Tevatron. Collider detectors are expected to perform a wide range of measurements. For a general purpose detector it is necessary to measure hadrons, leptons and gauge bosons over a large range of momenta. These particles manifest themselves in very distinctive ways. Quarks and gluons are observed as jets, whereas neutrinos escape detection and are observed as missing energy. Once an experiment has set its physics priorities stringent requirements are placed on the detector design. The nature of $\bar{p}p$ collisions, however, places some general requirements on any multipurpose detector designed to run at a hadron collider and these will be discussed in the next section.

4.1 Generalities

Because of the high energies reached in hadron collisions, detectors at $\bar{p}p$ colliders are calorimetric detectors. Good calorimetry is a real necessity for being a successful experiment. There are many aspects, though, that enter the definition of good calorimetry and in general a compromise needs to be made. Good energy resolution, containment of particle showers and the absence of cracks are necessities to eliminate fake sources of missing transverse energy. The high multiplicity of $\bar{p}p$ events, the position resolution and the multi-particle and multi-jet separation set the scale for the transverse segmentation of the calorimeter. For precision measurements an accurate understanding of the absolute energy scale is crucial. The accuracy to which the absolute energy scale can be determined is affected by the stability of the calorimeter, the uniformity of its response and the ease and precision to which the device can be calibrated. An important aspect of calorimeters is also the intrinsic response to electrons and pions, the e/π ratio. The UA1, UA2 and CDF detectors have non-compensating calorimeters, that is, e/π is not unity and their calorimeters will therefore respond differently to electromagnetic energy deposited by electrons, photons and π^0's compared to hadronic energy from charged pions. This results in non-linearities and a worsening of the energy resolution. At low momenta the

calorimeters of the UA1, UA2 and CDF detectors show substantial non-linearities in their response (see also section 6.1). The calorimeter of the DØ (and ZEUS) detector has an e/π ratio most close to unity and shows only minor deviations from linearity at low momenta [21, 22]

Because the cross section for inclusive jet production is several orders of magnitude larger than the cross section for any other large p_t process, a high level of rejection against jet events is desired when studying muons, electrons, photons and missing energy signals. This means that high quality tracking and containment of hadronic showers is important. Moreover, because of the high multiplicity environment good double track resolution is required and high quality extrapolation of tracks through calorimeters and muon detectors must be available. Although a central magnetic field aids in the track reconstruction, opens up a few more physics windows and provides an in situ calibration for the calorimeter, it is not essential for a collider detector. The UA1 and CDF detectors have a central magnetic field; the UA2 and DØ detectors are non-magnetic detectors.

In order to complement the electron detection channel all detectors, except UA2, have a muon detection system. For b-physics, a muon detection system at small angles is desired since the production cross section for b-quarks peaks at large absolute values of pseudorapidity.

Rather than giving a detailed description of the four collider experiments only the main features of these detectors will be discussed in the next four sections. A detailed description can be found in the references.

4.2 The UA1 Detector

The UA1 detector [18], shown schematically in figure 9, is a general purpose magnetic detector. Its central part is a 6 m long, 2.4 m diameter drift chamber system providing tracking and magnetic analysis of charged particles in the range $|\eta| < 3$. The central tracking chamber is surrounded by the electromagnetic calorimeters. Both the central detector and the electromagnetic calorimeters are inside the coil of a dipole magnet which produces a horizontal magnetic field of 0.7 Tesla perpendicular to the beam axis. The electromagnetic calorimeters, called gondolas in the central and bouchons in the forward region, are lead-scintillator sandwich calorimeters, longitudinally subdivided in four readout segments approximately 4, 7, 9 and 7 radiation lengths (X_0) thick. The transverse segmentation of the gondolas is $\Delta\vartheta \times \Delta\varphi = 5^\circ \times 180^\circ$. The bouchons have a much more fine segmentation of $\Delta\vartheta \times \Delta\varphi = 20^\circ \times 11^\circ$. The electromagnetic calorimeter is followed by a hadronic iron-scintillator calorimeter consisting of 450 readout cells, with a typical cell size of $\Delta\vartheta \times \Delta\varphi = 15^\circ \times 18^\circ$ in the central and $\Delta\vartheta \times \Delta\varphi = 5^\circ \times 10^\circ$ in the forward regions. The thickness of the hadron calorimeter is approximately 5 absorption lengths (λ_0) in the central region and 7 λ_0 in the forward regions. The energy resolutions of the calorimeters are $\sigma/E = 15\%/\sqrt{E}$ and $\sigma/E = 80\%/\sqrt{E}$, for the electromagnetic and

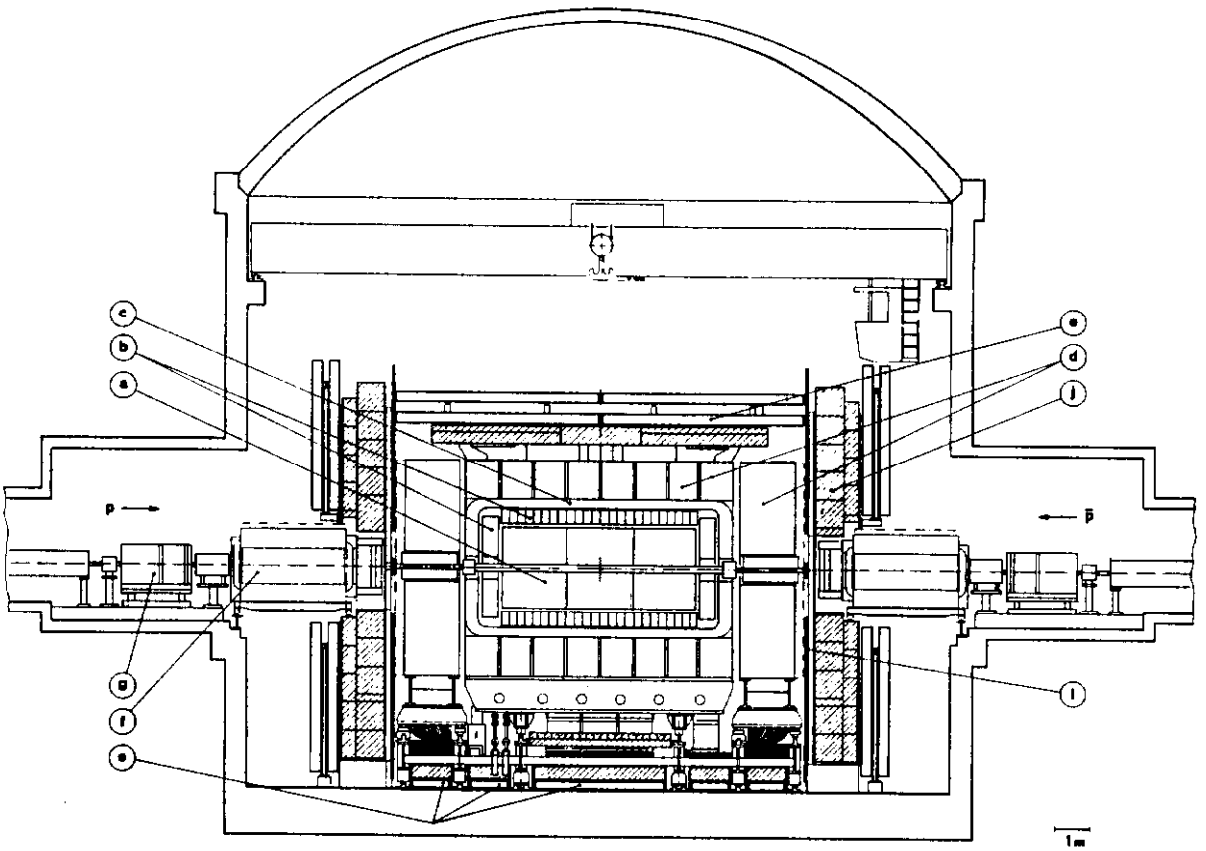

Figure 9: Schematic layout of the UA1 detector.

hadronic calorimeters, respectively. The muon system of the UA1 detector covers the pseudorapidity interval $|\eta| < 2.3$ and has full azimuthal coverage.

An ambitious upgrade program of the UA1 detector had been started in 1986. The muon system was improved by increasing the hadron absorber thickness both in the central and forward region with additional iron, instrumented with planes of limited streamer tubes. In the forward region additional drift tubes were installed. It was planned to replace the old calorimeter with a new uranium-TMP (Tetramethylpentane) calorimeter. To prepare for the insertion of the new calorimeter, the electromagnetic calorimeter was removed in 1988. Unfortunately the upgrade of the calorimeter never took place and the last data taken with the UA1 experiment was without an electromagnetic calorimeter. The recent UA1 results presented in these notes were taken with the electromagnetic calorimeter removed.

4.3 The Upgraded UA2 Detector

The UA2 detector [19] is purely an electron detector. The structure of the detector is shown in figure 10. Around the beam pipe, at radii of 3.5 cm and 14.5 cm, are two arrays of silicon pad detectors that measure the particle's dE/dx to reject photon conversions and Dalitz decays. Between the two is a cylindrical vertex drift chamber, measuring the tracks of charged particles. Behind the inner tracking detectors are the transition radiation detectors which provide an independent electron

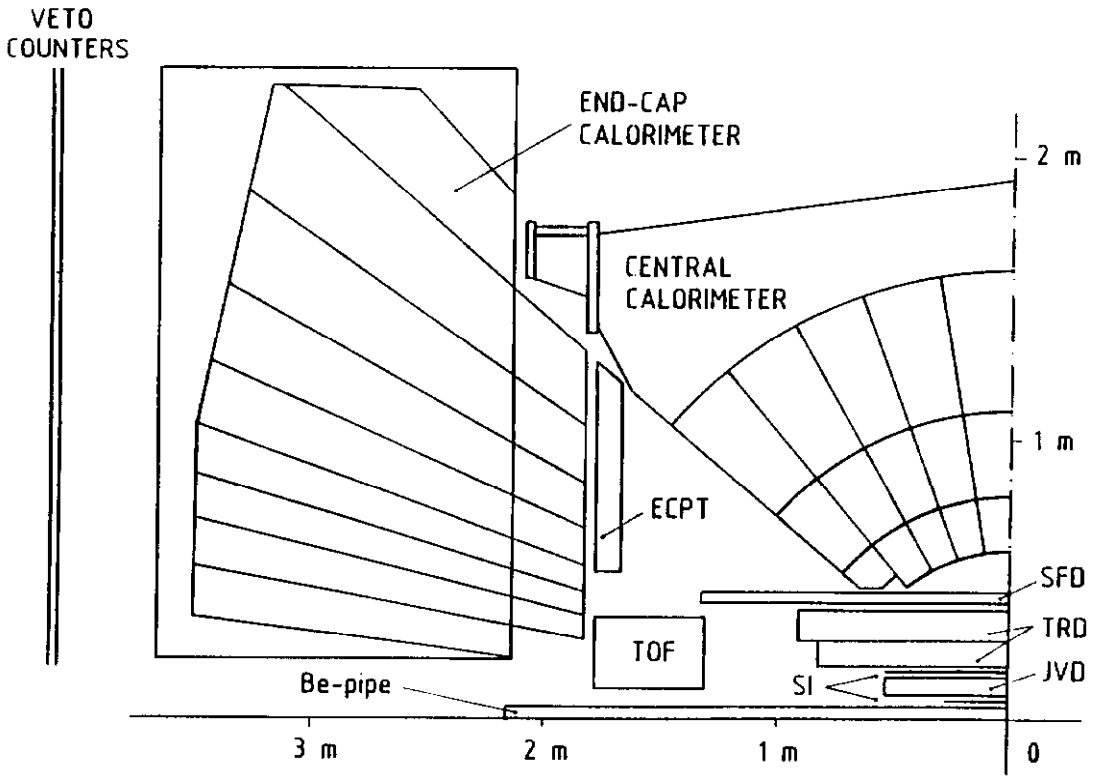

Figure 10: Schematic layout of one quadrant of the UA2 detector.

identification in addition to the calorimeter. The central detector is completed by a scintillating fiber detector which has three major components: 6 stereo triplets of tracking, a 1.5 X_0 thick lead converter followed by another 2 stereo triplets of scintillating fibers used to localize the early development of electromagnetic showers initiated in the lead converter. The track finding and electron identification are complemented in the forward and backward region by proportional drift tubes, including a 2 X_0 thick lead radiator for preshower detection, mounted on the calorimeter end caps.

Calorimetry is provided by a central calorimeter, covering pseudorapidities $|\eta| < 1$ and two end cap calorimeters covering the region $0.9 < |\eta| < 3$. The central calorimeter is segmented into 240 cells subtending 10° in ϑ and 15° in φ. The electromagnetic section is a multilayer sandwich of lead and scintillator, 17 X_0 deep with no longitudinal segmentation. The hadronic section is an iron-scintillator sandwich, subdivided in two longitudinal compartments. The total thickness of the central calorimeter is 4.5 λ_0 at normal incidence. The electromagnetic and hadronic compartments of the end cap calorimeters are also lead-scintillator and iron-scintillator multilayer sandwich calorimeters, respectively. The calorimeter cells in the interval $1.0 < |\eta| < 2.2$ have a segmentation of $\Delta\varphi = 15°$ and $\Delta\eta = 0.2$, with one electromagnetic and one hadronic longitudinal readout segment. The cells closest to the beam ($2.2 < |\eta| < 3.0$) have a segmentation twice as coarse in azimuth. The total depth of the end calorimeters is about 6.5 λ_0 at normal incidence.

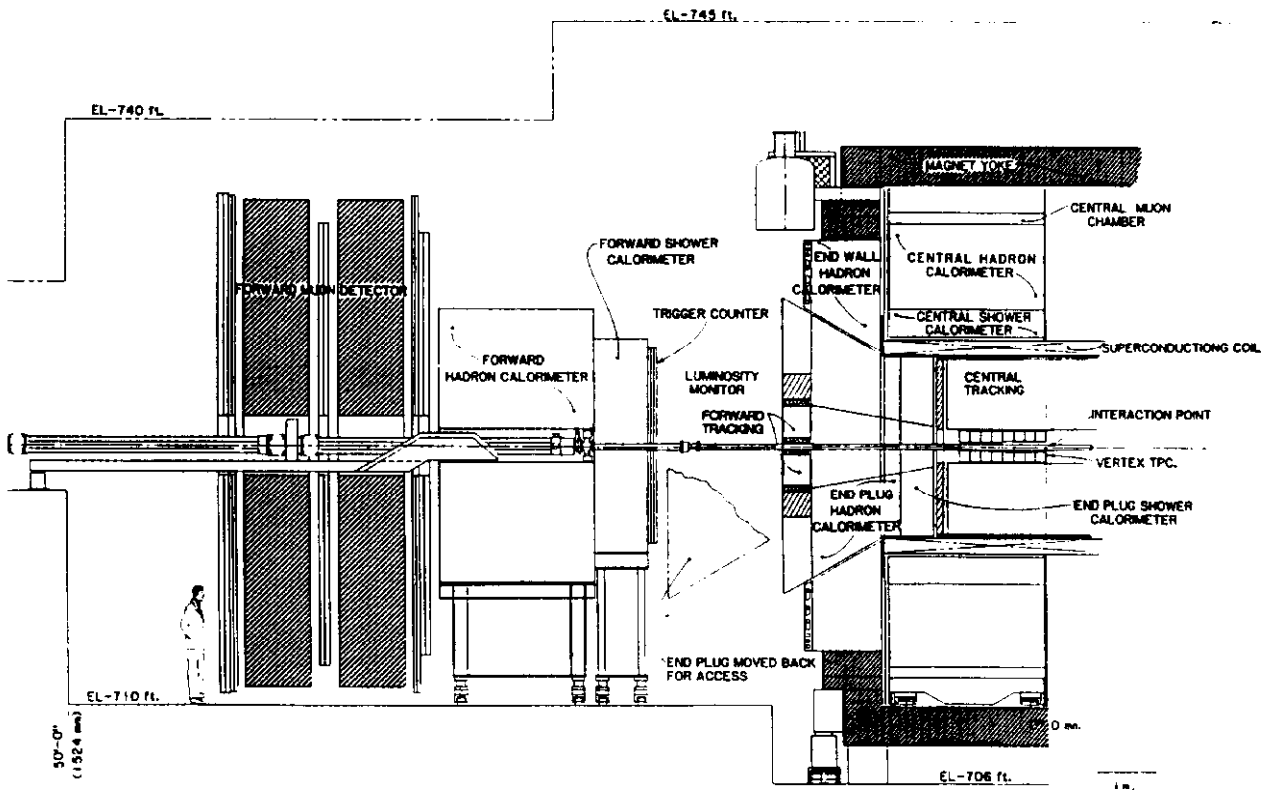

Figure 11: Schematic layout of one half of the CDF detector.

4.4 The CDF Detector

A cross section of the CDF detector [20] is shown in figure 11. In the central region the CDF detector has a vertex time projection chamber surrounded by a large volume axial wire drift chamber inside a superconducting 1.5 Tesla solenoid. Complete tracking information is available for $40° < \vartheta < 140°$. The central detector is followed by the calorimeter systems. CDF has three calorimeter systems: the central, plug and forward calorimeters. The central calorimeter, which covers the region $|\eta| < 1.1$, consists of a lead-scintillator sandwich electromagnetic calorimeter, followed by an iron-scintillator hadron calorimeter with a segmentation of $\Delta\eta \times \Delta\varphi = 0.11 \times 15°$. The active elements of the calorimeters outside the central region are gas-proportional chambers with cathode pad readout. The plug and forward calorimeters cover the pseudorapidity ranges $1.1 < |\eta| < 2.4$ and $2.2 < |\eta| < 4.2$, respectively. These calorimeters have a slight more fine segmentation than the central calorimeter: $\Delta\eta \times \Delta\varphi = 0.09 \times 0.087$. The respective absorber media for the non-central electromagnetic and hadronic calorimeters are the same as for the central calorimeter. Embedded in the electromagnetic calorimeter at shower maximum are strip chambers used in the electron identification. The CDF muon system covers the central region $|\eta| < 0.63$ and the far forward region $|\eta| > 2$. The upgraded CDF detector, which will run in 1992, will include a silicon vertex detector for tagging events with secondary vertices and a central pre-radiator detector for photon tagging. Furthermore, its muon system will have an extended coverage to $|\eta| < 1$ and the hadron rejection will be improved in this region because of added steel.

4.5 The DØ Detector

An isometric view of the DØ detector [21] is shown in figure 12. At the heart of the DØ detector is its calorimeter. One of the design aims of DØ was excellent calorimetry and to provide good energy resolution for electrons, photons and jets with good hermeticity. For these reasons, and for compactness, radiation hardness and uniformity of response, liquid argon with uranium as absorber was chosen for calorimetry. The DØ calorimeter consists of three parts of roughly equal size: a central calorimeter and two end calorimeters. The central calorimeter consists of three annuli of calorimetry. Surrounding the central detector is a ring of 32 electromagnetic calorimeter modules. This ring is enclosed by a ring of 16 fine hadronic modules. An annulus of 16 coarse hadronic modules around the fine hadronic modules completes the central calorimeter. The total thickness of the central calorimeter at normal incidence is 4.5 λ_0. Each of the end calorimeters consists of a ring of 16 outer hadronic calorimeter modules; inside this is another ring of 16 middle hadronic modules and at the central core is a monolithic inner hadronic module. The latter weighs 32 tons and has a diameter of 1.7 m. In front of the inner hadronic module is the electromagnetic end calorimeter. Both the central and end electromagnetic calorimeters are longitudinally subdivided in four read-out segments approximately 2, 2, 7, and 10 X_0 thick. The fine hadronic sections are read-out in three separate longitudinal layers in the central region and four read-out segments in the end calorimeters. Each fine hadronic read-out section is about one λ_0 thick. The coarse hadronic sections have no further longitudinal segmentation. Transverse segmentation is provided by readout pad electrodes on the signal boards, each covering an (η, φ) interval of $\Delta\eta \times \Delta\phi = 0.1 \times \pi/32$ (≈ 0.1). In the third longitudinal layer of the electromagnetic calorimeter, which typically contains 65% of the electromagnetic shower energy, the transverse segmentation is made finer to $\Delta\eta \times \Delta\varphi = 0.05 \times 0.05$ to provide better position resolution. The calorimeters have in total about 50,000 read-out channels.

In front of the calorimeters is the DØ Central Detector, composed of three tracking chambers and a transition radiation detector. The vertex detector has three layers of concentric cylindrical high precision drift chambers immediately surrounding the beam pipe. The transition radiation detector, encircling the vertex chamber, consists of three concentric layers of polypropylene foils followed by radial drift X-ray detectors to help separate electrons from pions. Outside of the transition radiation detector is a central drift chamber, composed of four concentric layers of axial wire chambers. Each end of the central detector is capped by a forward drift chamber. The forward drift chambers are composed of three layers of chambers. In the inner and outer chambers the wires are aligned along Cartesian coordinates giving a measure of the track's polar angle ϑ. In the middle chamber the wires are strung radially giving a measure of the track's φ angle.

The calorimeters are surrounded by the third major sub-system, the DØ muon system, which consists of magnetized iron toroids and sets of proportional drift

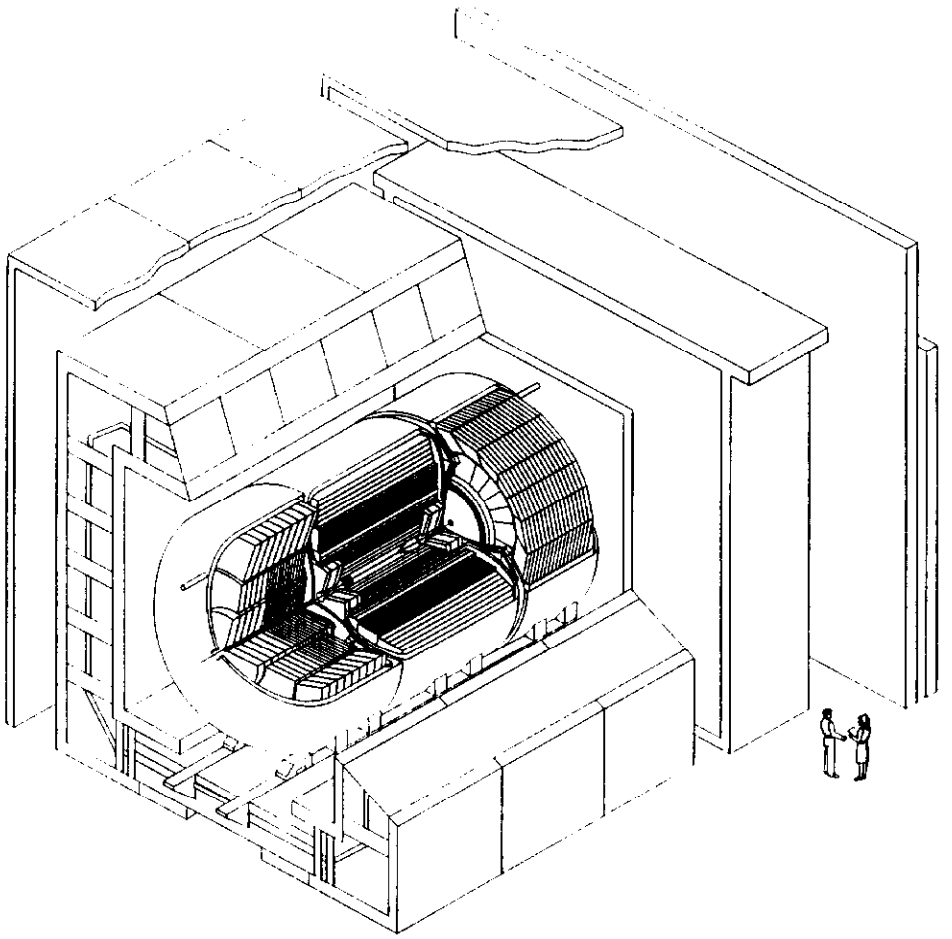

Figure 12: Isometric view of the DØ detector.

tube chambers. The muon system provides full coverage in the pseudorapidity range $|\eta| < 3.8$ and full azimuthal coverage. In the large angle region ten measurements are made along the muon trajectory; in both the forward and backward region nine planes of proportional drift tubes measure the charged particle track. The total number of interaction lengths seen by a particle is on average 13 λ_0 in the central region, and 18 λ_0 in the forward regions.

5 Large Momentum Transfer Processes

Interactions between particles are described by field theories. If the interaction is sufficiently weak, solutions to the field equations can be obtained using a perturbative expansion in the coupling constant of the interaction. Since the coupling constant for strong interactions is relatively small at large p_t, processes involving large momentum transfers can be described by perturbative QCD [23]. A schematic view of a $\bar{p}p$ collision is shown in figure 13. The QCD calculations are generally carried out in the Quark Parton Model. In this picture, the scattering occurs between the constituent partons that are treated as quasi free particles inside the hadrons. The momentum distributions of the initial partons are described by a set of parton distribution functions $f_i(x)$, which give the probability for finding a parton of type i inside the hadron carrying a fraction x of the hadron's total momentum. In this

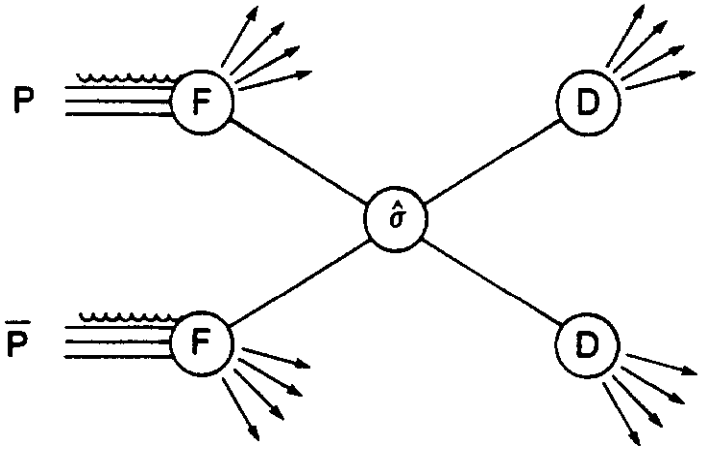

Figure 13: Schematic view of parton-parton scattering.

model, the incoming hadrons are regarded as beams of partons where the momentum distributions of the quarks and gluons are described by the distribution functions. Moreover, it is assumed that the distribution function $f_i(x_1)$ is independent of x_2, the momentum fraction carried by the parton in the other hadron. The hard scattering which takes place between these partons is in the parton model represented by the formula

$$\sigma = \sum_{ij} \int dx_1\, dx_2\, \hat{\sigma}_{ij}(\hat{s})\, f_i(x_1, Q^2)\, f_j(x_2, Q^2) \tag{10}$$

The subscripts i and j indicate the type of the incoming parton. The sum extends over all parton cross sections $\hat{\sigma}_{ij}$ contributing to the process. The parton cross section is evaluated at the parton center of mass energy, $\sqrt{\hat{s}}$, which is related to the hadron-hadron center of mass energy $\sqrt{s}$ through the relation $\hat{s} = x_1 x_2\, s$. They are calculable using perturbative QCD and are expressed as an expansion in the coupling constant α_s. To obtain the observed cross section at the proton level, the parton cross section is convoluted with the parton distribution function $f_i(x, Q^2)$ for parton species i. Figure 14 shows a typical set of structure functions, the product of x and the distribution function $f_i(x, Q^2)$, for gluons, u, d and s-quarks and the sea-quarks at a Q^2-scale of 10 GeV^2 [24].

In the naive parton model the parton distribution functions scale, that is, they are independent of the momentum transfer in the scattering process. In any interacting field theory though, like QCD, the partons interact with the carriers of the force thereby reducing their momentum by a fraction z. QCD corrections thus introduce a Q^2-dependence of the scattering process. This dependence is absorbed in a Q^2-dependence of the distribution functions and is referred to as "non-scaling behavior". The structure functions are generally derived from measurements of some reference process, normally taken to be deep inelastic scattering. They are then evolved to the Q^2-scale appropriate to the hard scattering process of interest. This evolution of the structure functions is governed by the Altarelli-Parisi equations [25]. The dependence of the structure functions on Q^2 is rather mild, since in QCD the scaling is broken by logarithms of Q^2. Figure 15 illustrates the Q^2-evolution of

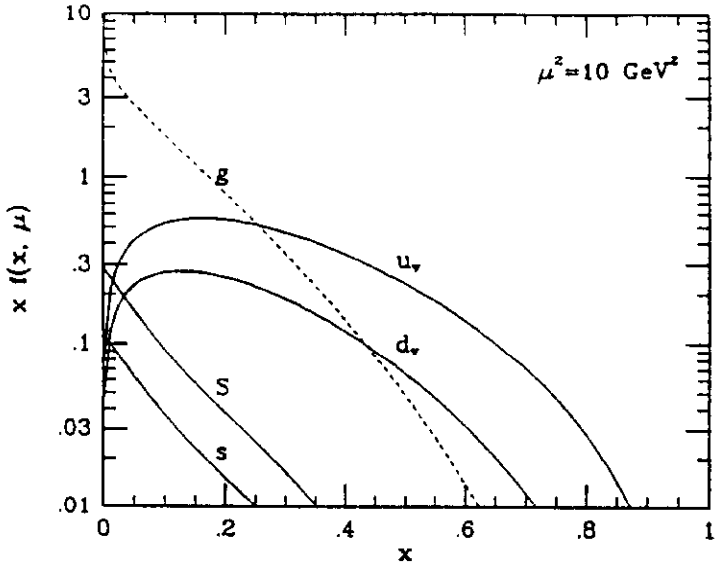

Figure 14: Quark and gluon distribution functions at $Q^2 = 10\ GeV^2$.

some structure functions [26].

There are many parametrizations of the structure functions, labeled after the names of their authors. Some of the most common ones are the parametrizations by Eichten, Hinchliffe, Lane and Quig (EHLQ) set 1 and 2 [27], Diemoz, Ferroni, Longo and Martinelli (DFLM) [28], Martin, Roberts and Stirling (MRS) [29] and Morfin and Tung [30]. The parametrizations differ from each other mainly in that they fit different experimental data and use different parametrizations for the gluon distribution function at low x [31]. As mentioned in the previous paragraph, the structure functions are measured in some reference process which is usually deep inelastic scattering. Since this process is not directly sensitive to the gluon distribution function, this distribution is inferred from the measured quark and anti-quark distributions. This results in rather large uncertainties in the gluon distribution because

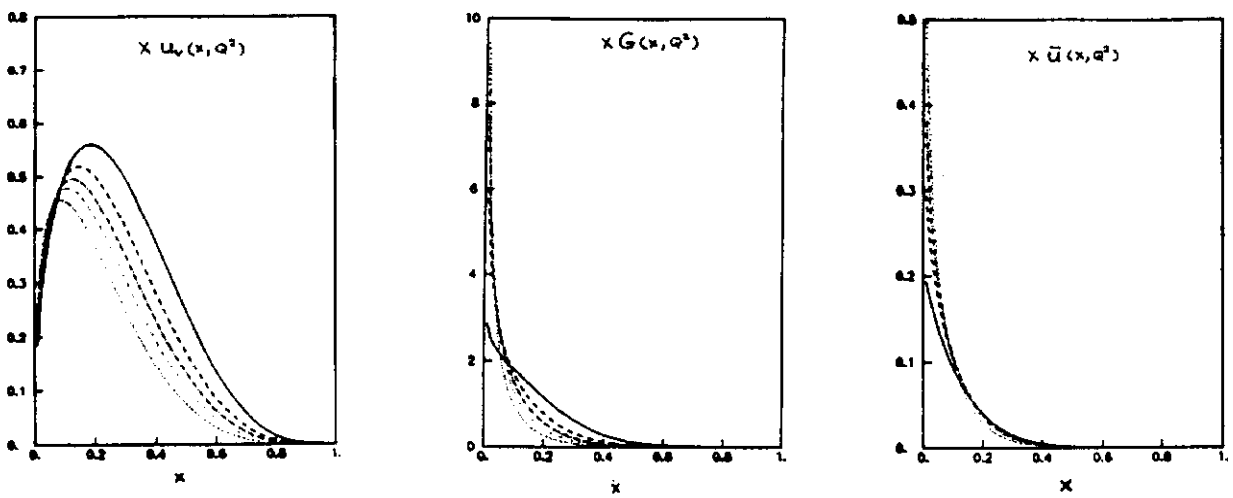

Figure 15: Q^2 evolution of some structure functions. The functions have been evolved from $Q^2 = 10\ GeV^2$ (solid lines) up to $Q^2 = 10^6\ GeV^2$ (dotted lines). Shown also are the distributions evaluated at the intermediate Q^2-values of 10^2, 10^3 and $10^4\ GeV^2$.

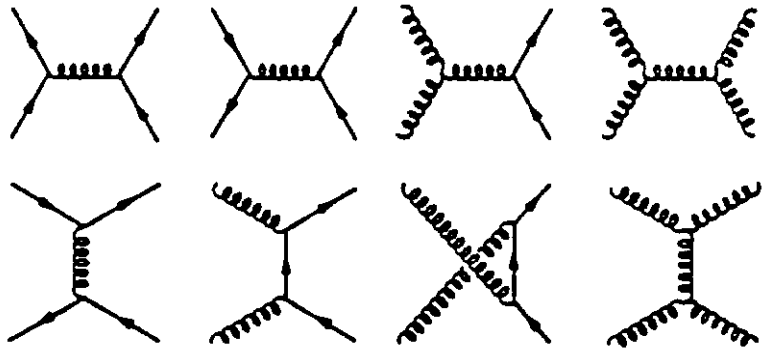

Figure 16: Feynman diagrams contributing to parton-parton scattering in lowest order.

of the sensitivity to the boundary conditions of the extraction method. It should be noted that the uncertainties in the Q^2-scale, the uncertainties in the structure functions and the unknown contribution from higher order calculations represent an intrinsic systematic error on all theoretical predictions.

Figure 16 shows the diagrams contributing to two-jet production in $\overline{p}p$ collisions. The important contributions to the cross section are the t-channel contributions. The angular distribution in the center of mass system is thus similar to Rutherford scattering:

$$\frac{d\hat{\sigma}}{d\hat{t}} = \frac{|M|^2}{16\pi\hat{s}^2} \tag{11}$$

Because of color factors, the two-jet cross section at the parton level is dominated by gluon-gluon scattering. To obtain the observed cross section, the parton cross sections need to be folded with the proton structure function. Although the cross section is dominated by gluon-gluon scattering at the parton level, the situation is significantly different at the proton level. Since the gluon distribution function peaks at low x (see figure 14), the gluon-gluon contribution is heavily suppressed for high subprocess center of mass energies. Figure 17 shows the expected fractions of gg, $q\overline{q}$ and $qg + \overline{q}g$ final state two-jet events in the pseudorapidity range $|\eta| < 2$ as function of the parton center of mass energy $\sqrt{\hat{s}} = x_1 x_2\, s$. The suppression of the gluon contribution with increasing $\sqrt{\hat{s}}$ due to the steeply falling gluon structure function with increasing x is clearly visible. The importance at the detector level of each of the eight basic $(2 \rightarrow 2)$ processes shown in figure 16 depends on the structure functions describing the initial quark and gluon fluxes.

The final stage of the hard scattering process is the formation of colorless hadrons from the outgoing colored partons called fragmentation or hadronization (see fig. 13). This process is a soft process and the hadrons are produced with small p_t with respect to the initial parton direction. Since the hadrons follow the initial parton direction and produce a confined jet of particles, the observed hadronic jet can be associated with the colored parton produced in the hard scattering process.

A typical $\overline{p}p$ event appears in the detector as two beam jets at high absolute values of pseudorapidity, remnants of the incoming proton and anti-proton, and two

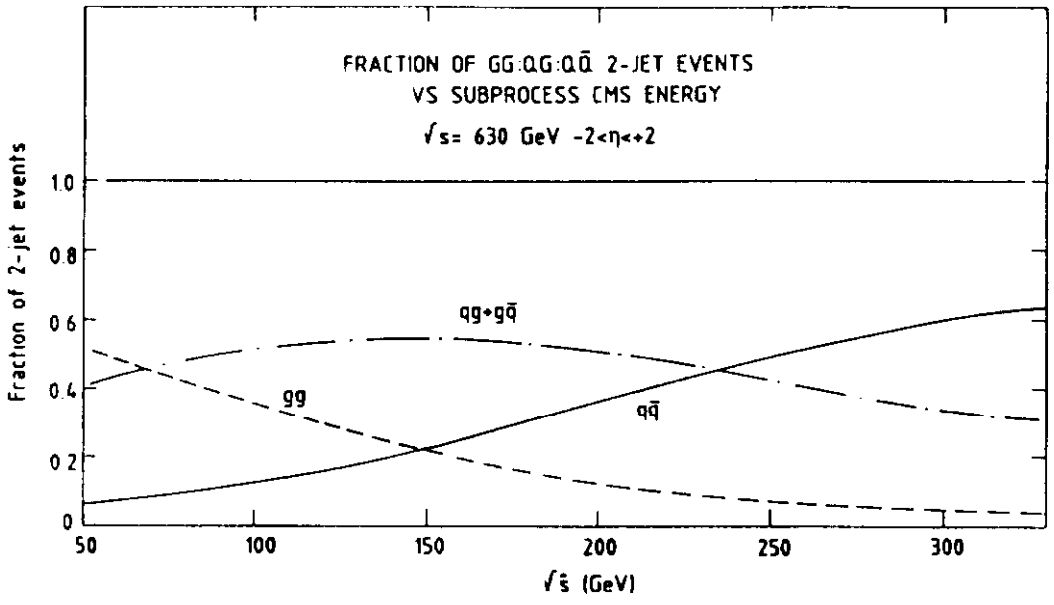

Figure 17: Fractions of gg, $q\bar{q}$ and $qg + \bar{q}g$ final state two-jet events in the pseudo-rapidity range $|\eta| < 2$ as function of the parton center of mass energy $\sqrt{\hat{s}}$.

or more high p_t objects resulting from the hard parton-parton scattering. The partons that do not participate in the hard scattering give rise to the underlying event, which is well described by a flat rapidity distribution of low p_t particles (cf. section 3.2).

6 Jet Physics and QCD studies

6.1 Jet finding

The study of high p_t jets allows high statistic tests of QCD predictions. Although high p_t jets, which manifest themselves in a detector as localized deposits of energy, can be identified relatively easily, a quantitative study of jets is far from trivial. The basic assumption in jet measurements is that the observed jet distributions follow closely those of the parton processes. This assumption relies on the ability to experimentally define jets that are well matched with the theoretical predictions.

Experimentally jets are identified using a jet finding algorithm. There are many different jet algorithms and every experiment utilizes different algorithms for different applications. For a jet finding algorithm to be acceptable, it must meet certain conditions. Above all, the algorithm must be robust, that is, it must be stable against fluctuations caused by fragmentation, by the underlying event and by the finite energy resolution of the calorimeter. Furthermore, it should give stable results independent of event topology. The algorithm should also be free of singularities over the whole angular coverage of the detector. The jet finding algorithm that is used in the final stages of the data analysis of comparing experimental data with theory must provide a good correlation between the parton and the jet, both in energy and position.

One of the most popular jet finding algorithms is the "fixed cone" algorithm. It is commonly used because it is very robust and allows an easy comparison between experiment and theory. This iterative algorithm consists of two stages: a pre-clustering stage and a jet-formation stage. In the pre-clustering stage contiguous towers, each with a transverse energy above typically 1 GeV are joined to form pre-clusters. Any pre-cluster with an energy above a couple of GeV is considered a seed for the cluster finding. In the jet-formation stage, the energy of all cells within a cone of radius $R = \sqrt{\Delta\eta^2 + \Delta\varphi^2}$ in (η, φ)-space around the position of the seed is added to the cluster. The position of the cluster, using the energy weighted centroid of all towers in the cluster, is then recalculated. A new circle in (η, φ)-space is drawn around the recalculated position and the procedure is iterated until a stable cluster is found. The cluster that passes a certain E_t threshold is called a jet. The size of the cone is a parameter in the algorithm and is typically taken to be $R = 0.7$ at $\sqrt{s} = 1.8\ TeV$.

The energy and transverse energy of the jet can be evaluated using the relations

$$\begin{aligned} E_{cluster} &= \sum_i E_i \\ \vec{E}_{cluster} &= \sum_i E_i\, \hat{n}_{centroid} \\ E_{tcluster} &= \sum_i E_t^i\, \sin\vartheta_{centroid} \end{aligned} \tag{12}$$

The sum runs over all towers in the cluster and the vector $\hat{n}_{centroid}$ is a unit vector pointing from the reconstructed vertex to the center of the cluster. The energy vector and the transverse energy of the cluster can be defined using the cluster centroid, as indicated in the relations given above. They can also be defined, however, using the centroids of the individual towers:

$$\begin{aligned} E_{cluster} &= \sum_i E_i \\ \vec{E}_{cluster} &= \sum_i E_i\, \hat{n}_i \\ E_{tcluster} &= \sum_i E_t^i\, \sin\vartheta_i \end{aligned} \tag{13}$$

The vectors $\hat{n}_i$ are now unit vectors parallel to the direction ϑ_i given by the vertex of the event and the geometric center of tower i. There is no compelling reason to use one or the other and it is a matter of experimental preference which definition is used. The CDF collaboration uses the former definition while the UA1 and UA2 collaborations use the latter. Also DØ will use the latter definition.

An experimentally difficult task is to translate the observed jet energy to the initial parton energy. Detector effects as well as physics effects have to be taken into account to establish the absolute energy scale for jets. Non-compensating

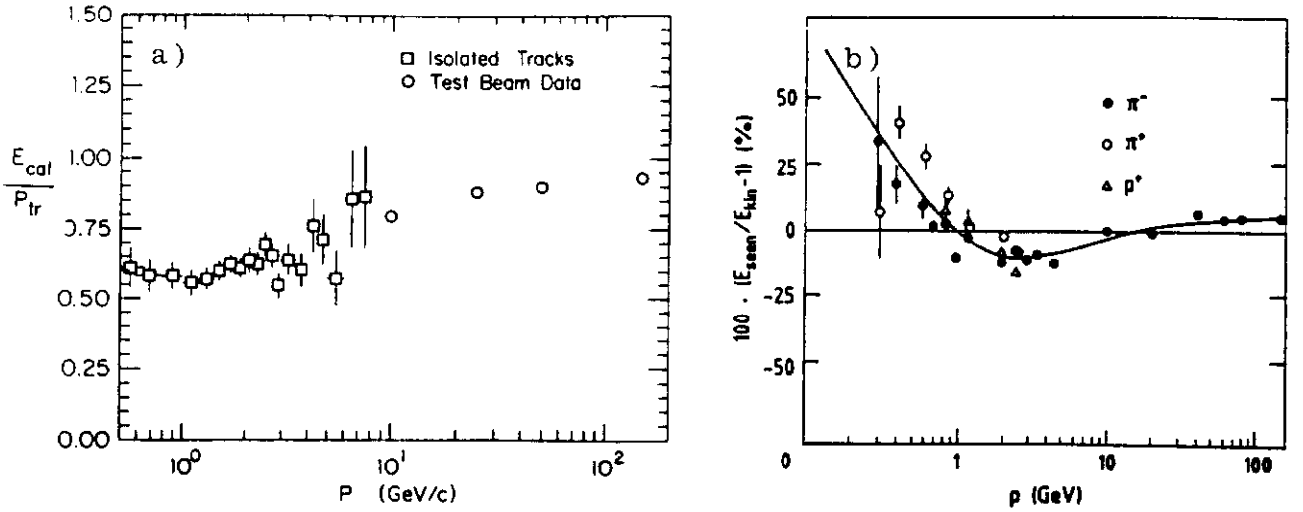

Figure 18: Nonlinearity of the (a) CDF and (b) UA2 detector.

calorimeters and non-linearities in their response are main detector effects contributing to a shift of the jet energy with respect to the original parton energy. Figure 18 shows the ratio of the observed energy in the calorimeter and the measured particle momentum as function of the particle momentum for both CDF (Fig. 18a) and UA2 (Fig. 18b). Both calorimeters show substantial non-linearities at low momenta. These non-linearities in detector response cause the observed jet energy to be systematically lower than the parton energy. Knowing the charged particle momentum spectrum within a jet, this effect can on average be corrected for.

Besides the purely detector effects, there are physics effects that change the observed jet energy. Two effects are illustrated in figure 19. Plotted here is the distribution of energy for two-jet events as function of φ, the azimuthal angle with respect to the leading jet. The two peaks at $\varphi = 0°$ and $\varphi = 180°$ result from

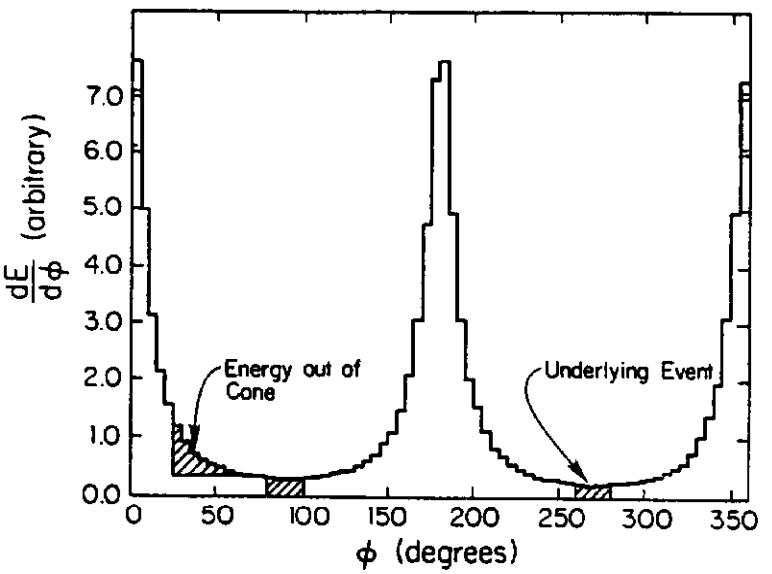

Figure 19: Distribution of energy in two-jet events as function of φ, the azimuthal angle with respect to the leading jet.

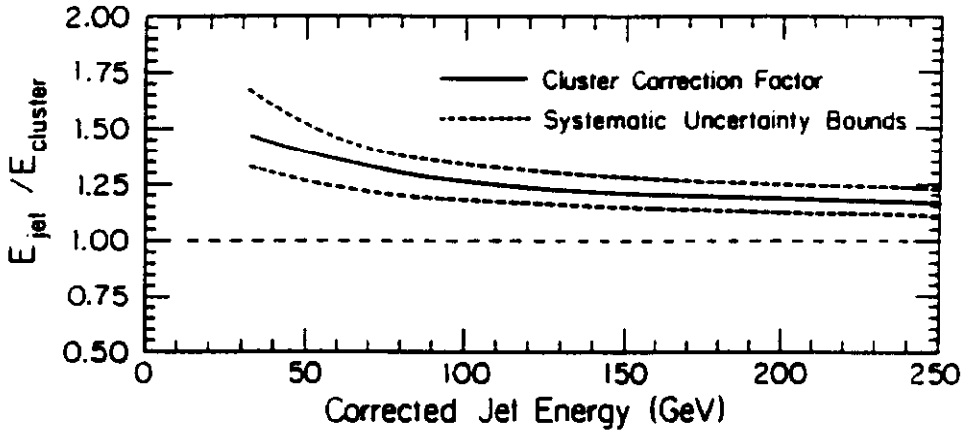

Figure 20: Correction factor applied to the observed cluster energy to obtain the corresponding jet energy for the CDF detector. The dashed lines represent the limit of the systematic uncertainty assigned to the correction.

the two-jet dominance of the events. As is shown in the figure, energy that is part of the jet energy, is lost outside the fixed cone of the clustering algorithm due to fragmentation effects. On the other hand, energy from the underlying event, which is estimated from the flat energy distribution between the jets, is added to the jet energy.

The observed jet energies need to be corrected for all these effects, most of which depend on η and p_t. CDF has done a careful study of the systematic effects on jet energies [32] and the results are summarized in figures 20 and 21. Figure 20 shows the total correction factor to be applied to the observed cluster energy as function of the corrected jet energy. Correction factors of up to 50% are applied for low energetic jets. Figure 21 shows the total systematic error on the jet energy and the individual contributions as function of the energy of the jet.

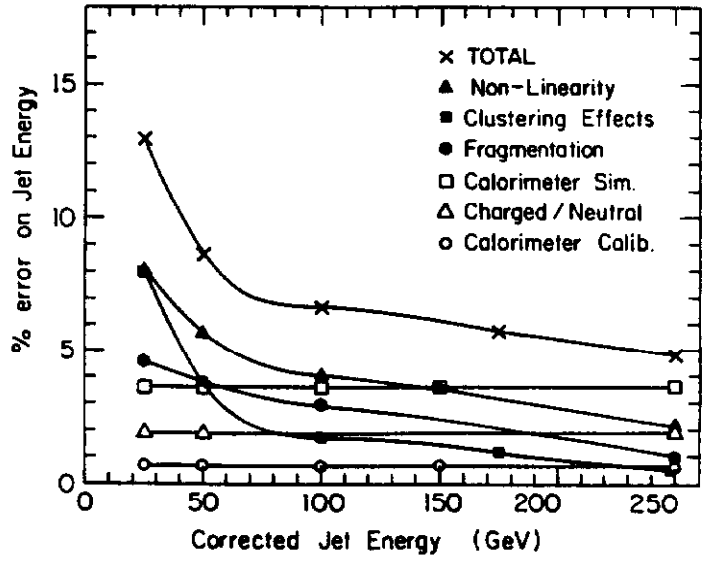

Figure 21: Individual contributions to, and total systematic error on the jet energy as determined for the CDF detector.

6.2 Jet production and production properties

In the parton model the jet production cross section is given by equation 10. It was noted there that the dominant contributions at all values of p_t came from the t-channel exchange diagrams. Since the matrix elements of the t-channel diagrams are similar, the rates of quark-quark, quark-gluon and gluon-gluon scattering is determined by structure functions and color factors. Considering that at present one does not experimentally distinguish between the different final states and that one cannot distinguish between the different incoming partons, the similarity between the different matrix elements allows one to use the "single effective subprocess approximation" [33], that is, the differential cross section can be written as

$$\frac{d^3\sigma}{dx_1\,dx_2\,d\cos\vartheta^*} = \frac{F(x_1)}{x_1}\,\frac{F(x_2)}{x_2}\,\frac{d\hat{\sigma}_{ses}(1,2\to 3,4)}{d\cos\vartheta^*} \tag{14}$$

where

$$F(x) = G(x) + \frac{4}{9}\sum_i (Q_i(x) + \overline{Q}_i(x)) \tag{15}$$

The parton cross section $\hat{\sigma}_{ses}$ is in this approximation the cross section of a dominant parton-parton scattering process taken to be $gg \to gg$:

$$\frac{d\hat{\sigma}(gg\to gg)}{d\cos\vartheta^*} = \frac{9}{8}\,\frac{\pi\alpha_s^2}{2\,\hat{s}}\,\frac{(3+\cos^2\vartheta^*)^3}{(1-\cos\vartheta^*)^2} \tag{16}$$

The structure function $F(x)$ is a combination of the quark, anti-quark and gluon structure functions.

The structure function $F(x)$ and the angular distribution can be extracted from the topology of two-jet events. Since the cross section is proportional to the product $F(x_1)\,F(x_2)$ both x_1 and x_2 have to be known to extract $F(x)$. These variables are readily obtained from the measured parton relative center of mass energy, τ, and the measured Feynman x-variable, x_F, defined through the relations

$$\tau = \quad x_1\,x_2 \quad = \frac{\hat{s}}{s} = \frac{(p_3+p_4)^2}{s} \tag{17}$$

$$x_F = \; x_1 - x_2 \; = \frac{\vec{p}_{3L}+\vec{p}_{4L}}{\frac{1}{2}\sqrt{s}} \tag{18}$$

Note that the parton center of mass energy is simply the di-jet invariant mass, $\hat{s} = x_1\,x_2\,s = m_{jj}^2$. Solving the two equations for x_1 and x_2 yields,

$$x_{\frac{1}{2}} = \frac{1}{2}\left[\pm x_F + \sqrt{x_F^2 + 4\tau}\,\right] \tag{19}$$

The direction ϑ^* in the parton center of mass system is given by

$$\cos\vartheta^* = \frac{(\vec{p}_3-\vec{p}_4)\cdot(\vec{p}_1-\vec{p}_2)}{|\vec{p}_3-\vec{p}_4|\,|\vec{p}_1-\vec{p}_2|}$$

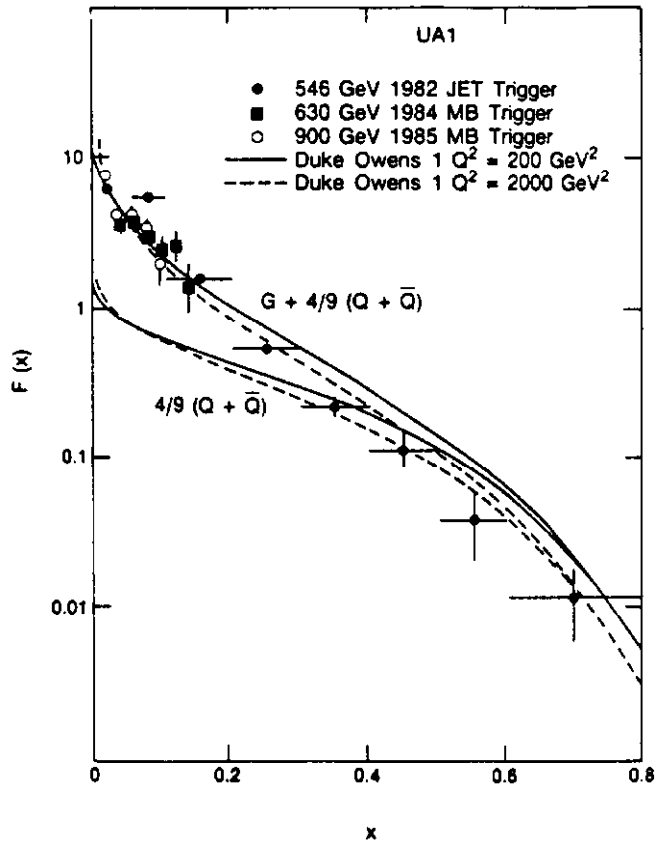

Figure 22: The effective structure function $F(x)$ as measured by the UA1 collaboration. The curves show the QCD prediction with and without the gluon contribution, evaluated at two Q^2-values.

Both the UA1 and UA2 experiments have extracted $F(x)$ using inclusive jet data [35]. Figure 22 shows the UA1 measurement of $F(x)$ with the QCD prediction evaluated at two values of the Q^2-scale. The fraction of the proton momentum carried by the partons decreases exponentially with increasing x. The expected distribution due to quarks and antiquarks only without the gluon contribution is shown separately. The data demonstrates that the jet cross section at low x cannot be described by quark-antiquark scattering alone, but is in good agreement with the full QCD calculation showing the non-abelian nature of the strong interactions.

Because of the dominance of the t-pole exchange diagrams, the di-jet angular distribution, as given in equation 16, follows closely a Rutherford law. Figure 23 shows the two-jet angular distribution as measured by UA1 [36]. The broken curve is the exact angular distribution predicted by all QCD tree graphs. The full curve is the QCD prediction including non-scaling effects.

Deviations from Rutherford scattering and non-scaling effects are more pronounced when the angular distribution is plotted as function of the variable $\chi = (1 + \cos\vartheta^*)/(1 - \cos\vartheta^*)$ [34]. For pure Rutherford scattering the differential cross section $d\sigma/d\chi$ is constant. Figure 24 shows the UA1 measured χ-distribution. The data, which shows a marked increase with increasing χ, follows nicely the QCD prediction provided higher order scale breaking effects are taken into account.

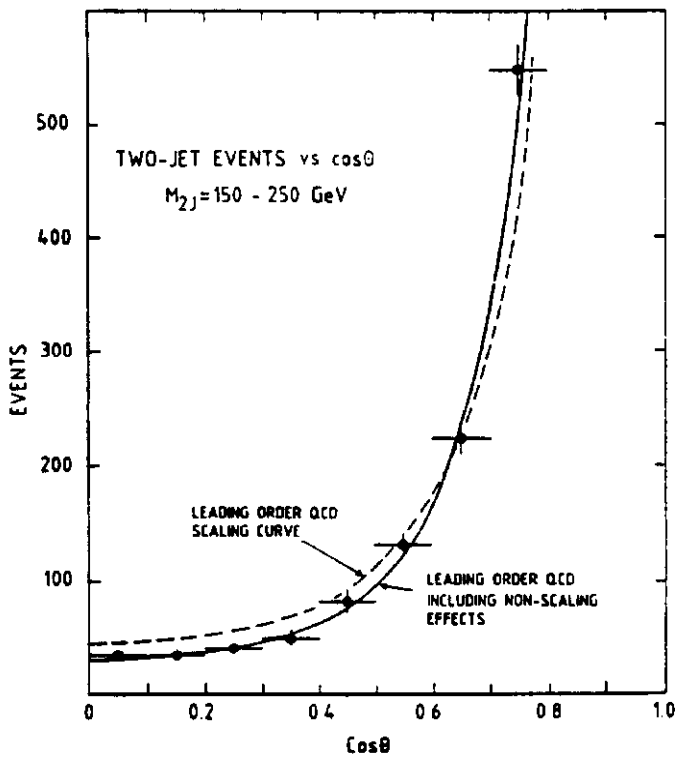

Figure 23: The UA1 two-jet angular distribution versus $\cos\vartheta^*$. The broken curve shows the leading order QCD prediction; the solid curve takes into account scale breaking effects.

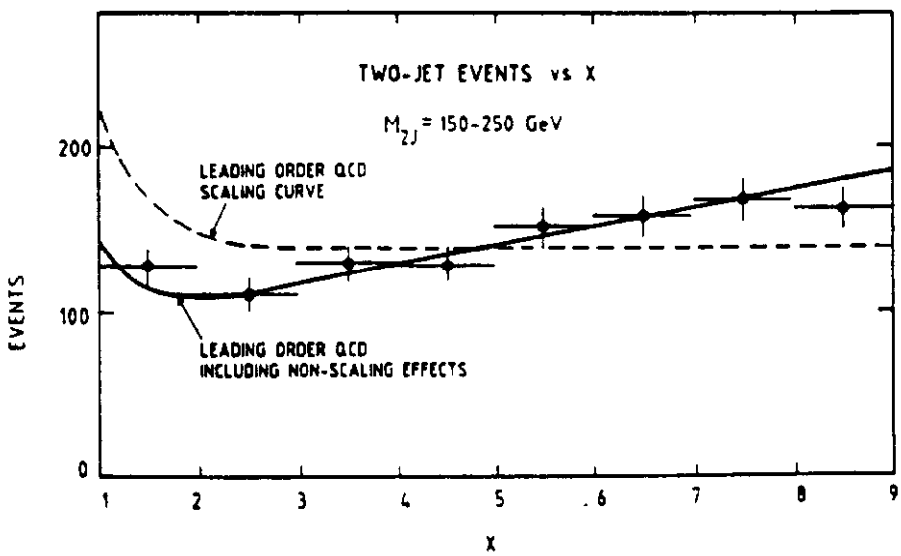

Figure 24: UA1 two-jet angular distribution versus $\chi = (1 + \cos\vartheta^*)/(1 - \cos\vartheta^*)$. The broken curve shows the leading order QCD prediction; the solid curve includes scale breaking corrections.

Three jet events result from the emission of a hard gluon in the initial or final state. The final state parton configuration for a (massless) three body final state is specified by five independent variables. Three angular variables and two energy fractions in the parton center of mass system are commonly chosen to specify the final state of the process ($1,\ 2 \rightarrow 3,\ 4,\ 5$). The three angular variables are the angles ϑ_3^*, ψ and φ. The angle ϑ_3^* is the angle between parton 3 and the beam direction. The angle ψ indicates the angle between the plane spanned by the direction of partons 4 and 5 and the plane defined by parton 3 and the beam axis. The remaining azimuthal degree of freedom of parton 3 with respect to the beam direction is described by the angle φ. Since the final state is isotropic for unpolarized beams the φ-dependence is generally integrated out. For the two remaining independent variables the energy fractions x_3 and x_4 of the outgoing partons 3 and 4 are taken. They are scaled to the total subprocess center of mass energy such that $x_3 + x_4 + x_5 = 2$. The partons are ordered in a way that $x_3 > x_4 > x_5$.

Figure 25 shows the distributions for x_3 and x_4 as obtained by CDF [37]. The data sample was obtained by requiring at least three energy clusters, each having an $E_t > 10\ GeV$, falling within the angular region $|\eta| < 3.5$. To ensure that the jets are well separated from each other and from the beams, kinematic cuts are applied. Soft gluon bremsstrahlung events are eliminated by requiring that the leading jet carries less than half the center of mass energy in the parton center of mass system, $x_3 < 0.9$. This ensures that the jets from partons 4 and 5 are resolved as separate jets. The angular cuts $|\cos\vartheta_3^*| < 0.6$ and $30^\circ < |\psi| < 150^\circ$ eliminate soft initial state gluon radiation and guarantee that all three jets are well separated from the beam jets. In addition to these cuts, the jets were required to be separated in (η, φ)-space by 0.85 and to have a three-jet invariant mass $m_{jjj} > 250\ GeV/c^2$. Along with the data are shown the predictions from phase-space, full QCD and $q\bar{q}$ initial states only. The data clearly prefers the full QCD calculation and significant deviations from the phase-space model are observed. This indicates that three jet events originate from a bremsstrahlung process, a proposition which is corroborated by the distribution of the angle ψ in three-jet events and the similarity in angular distribution of the leading jet in two- and three-jet events [36, 37, 38]

The cross-section for inclusive production of jets as function of the jet transverse momentum has been measured by all collider experiments. The cross section for this process, which has been calculated to $\mathcal{O}(\alpha_s^2)$ in QCD [39], is dominated by $(1,2 \rightarrow 3,4)$ parton scattering. Figure 26 shows the UA2 inclusive jet cross section $d^2\sigma/dp_t d\eta$ as function of p_t for different $|\eta|$ bins [40]. The error bars shown include both statistical and p_t-dependent systematic errors. The curves represent the QCD $\mathcal{O}(\alpha_s^2)$ calculation with $Q^2 = (\frac{1}{2}p_t)^2$ using the EHLQ structure functions. The agreement between the experimental data points and the QCD prediction is good for central values of η both in terms of p_t-dependence and in terms of the values for the absolute cross section. Only a marginal agreement is observed at large values of $|\eta|$. It should be noted, however, that there are additional large systematic

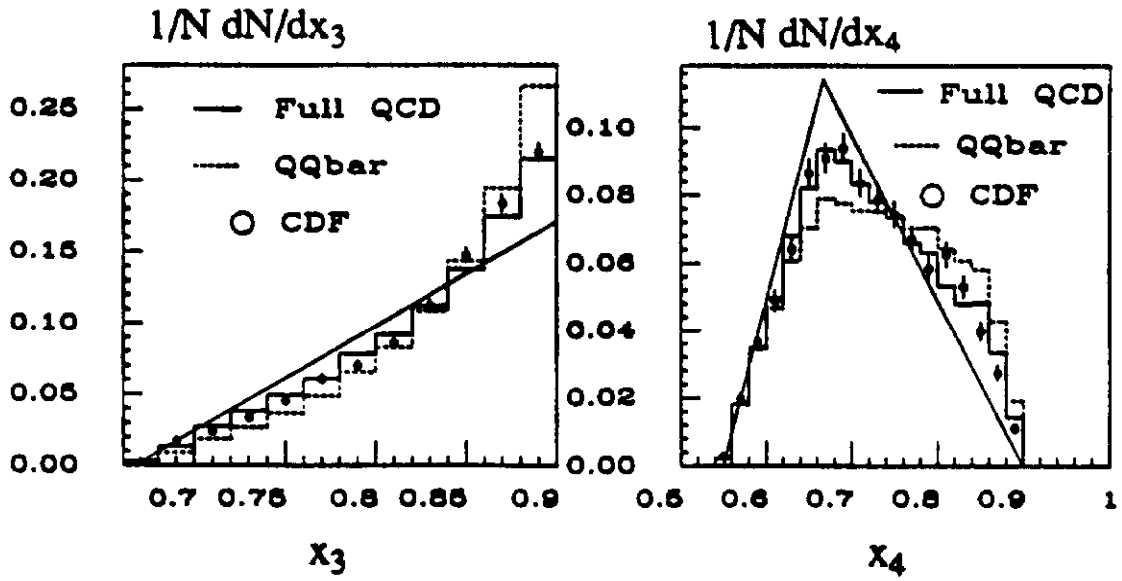

Figure 25: Distributions of the CDF jet energy fractions x_3 and x_4 for 3-jet events as observed in the CDF detector. The predictions from phase-space, full QCD and $q\bar{q}$ initial states only are also shown.

uncertainties, that are not indicated in the figure. First, there is a large experimental systematic uncertainty resulting in an overall 32% systematic scale error on the cross section. This error is dominated by contributions from the model dependence of the acceptance correction calculations and by the systematic uncertainty on the absolute calorimeter energy scale of 11%. Secondly, as mentioned already in section 5, there are large theoretical systematic uncertainties due to the uncertainty in Q^2-scale and the uncertainties in the parametrization of the distribution functions. UA2 has studied the effect of the different structure functions on the inclusive jet cross section [40]. Figure 27 shows the ratio of the measured inclusive jet cross section for the central region and the QCD calculation using the EHLQ structure functions. The curves represent calculations for different sets of structure functions, also normalized to the calculation using the EHLQ structure functions. All results are evaluated for $Q^2 = (\frac{1}{2}p_t)^2$, which gives the best description of the data for most cases. Excursions of up to 30% are observed by choosing different structure functions. Although the agreement between the QCD predictions and the experimental data, spanning seven orders of magnitude, is amazing, quantitative predictions are difficult because of the inherent large systematic experimental and theoretical errors in jet studies. It is a real challenge for the current collider experiments to constrain the QCD calculations and make quantitative predictions. Though the task seems daunting, the large data samples that will become available in the near future should make this possible.

The measurement of the inclusive jet cross section also allows to study models of quark compositeness. If quarks are composite objects, their strong cou-

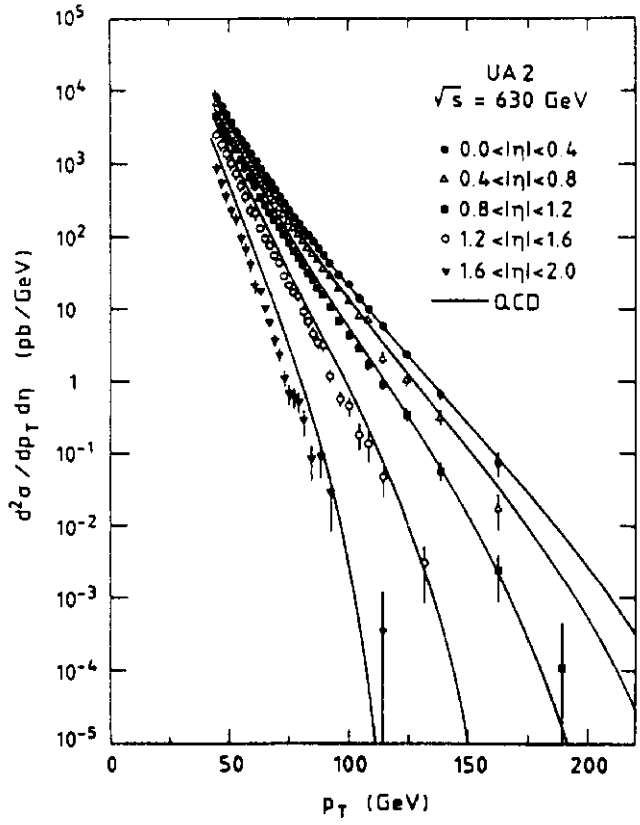

Figure 26: Inclusive jet cross section $d^2\sigma/dp_t d\eta$ for different bins of pseudorapidity as measured by UA2. The curves represent a QCD $\mathcal{O}(\alpha_s^2)$ calculation with $Q^2 = (\frac{1}{2}p_t)^2$ using the EHLQ structure functions.

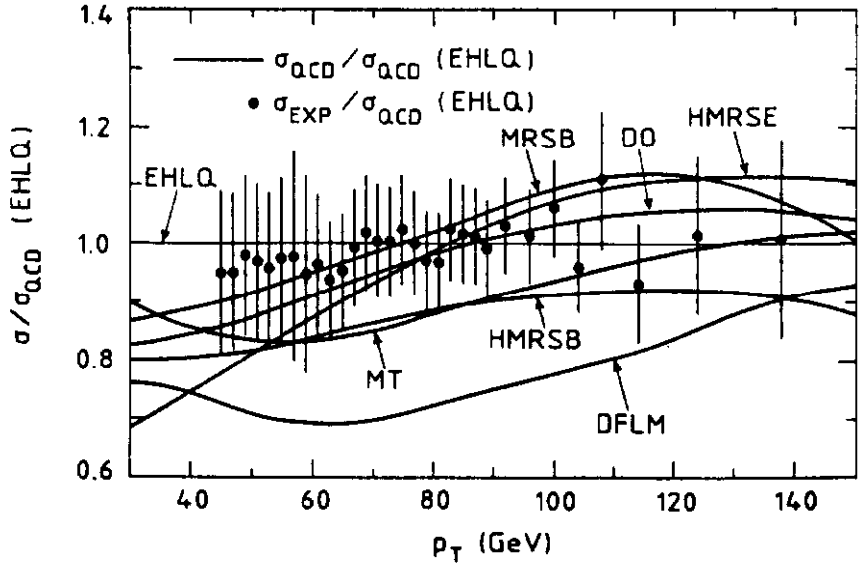

Figure 27: Ratio of the inclusive jet cross section for the central region, shown in figure 26, and the QCD calculation using the EHLQ structure functions. The curves show the sensitivity to different structure functions.

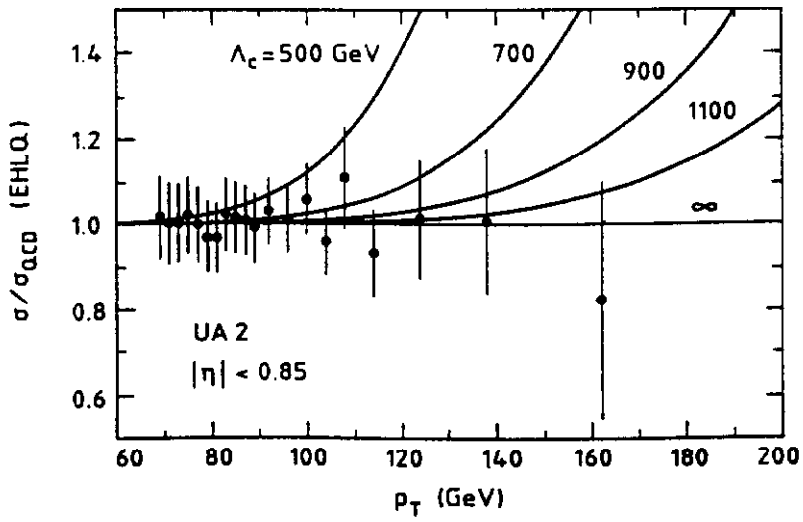

Figure 28: Ratio of the UA2 inclusive jet data and the QCD calculation using the EHLQ structure functions evaluated at $Q^2 = (\frac{1}{2}p_t)^2$. The solid curves show the predicted behavior, relative to the QCD calculation, for finite values of Λ_c.

pling will be modified to include a form factor

$$F(Q^2) = \left(1 + \frac{Q^2}{\Lambda_c^2}\right)^{-1}$$

Quark compositeness is phenomenologically described by adding a contact interaction between left-handed quarks to the Lagrangian [41]. The strength of the new interaction is characterized by an energy scale Λ_c. This interaction adds a term to the inclusive cross section that is independent of $\hat{s}$, giving rise to an excess of events at large p_t with respect to the standard QCD prediction, which corresponds to $\Lambda_c = \infty$. Figure 28 shows the ratio of the UA2 inclusive jet cross section data from the central region and the QCD calculation using $\Lambda_c = \infty, Q^2 = (\frac{1}{2}p_t)^2$ and the EHLQ structure functions [40]. The calculations have been normalized to the data in the region $69 < p_t < 79\ GeV/c$, where contributions from the contact term are negligible. The behavior predicted for finite values of Λ_c relative to the QCD prediction are shown as solid curves. The UA2 data allows to set an upper limit on Λ_c of 0.8 TeV, at 95% confidence level. Since the greatest sensitivity to possible substructure effects is at large p_t, higher center of mass energies allow to set more stringent limits. CDF has reported an upper limit on Λ_c of 1.4 TeV, at 95% confidence level [42].

6.3 Jet fragmentation

Since the transformation process of outgoing colored quarks and gluons into colorless jets of hadrons involves non-perturbative effects, quantitative predictions for the fragmentation process cannot be made within the perturbative QCD framework. Rather, the distribution of the jet momentum among the charged hadrons is

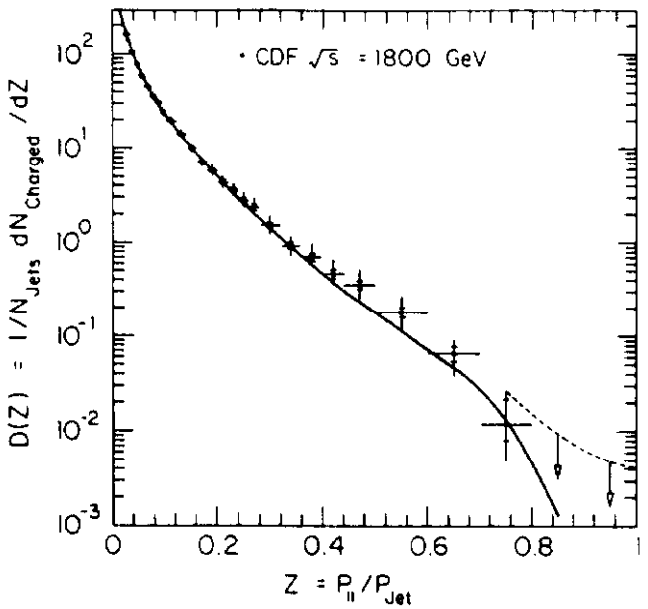

Figure 29: Charged fragmentation function $D(z)$ as measured by CDF. The solid curve is a Monte Carlo prediction.

described phenomenologically by a fragmentation function, $D(z, Q^2)$, defined as

$$D(z, Q^2) = \frac{1}{N_{jets}} \frac{dN_{charged}}{dz} \tag{20}$$

where

$$z = \frac{p_{||}}{|\vec{p}_{jet}|} \tag{21}$$

Here $p_{||}$ is the particle momentum parallel to the jet axis. The factor $1/N_{jets}$ simply indicates the average over the number of jets in the data sample. The magnetic detectors CDF and UA1 have both measured the fragmentation of jets [43, 44]. The CDF study was based on two-jet events in the pseudorapidity range $0.1 < |\eta| < 0.7$. The jets were identified using the cone algorithm with a jet cone of radius $R = 1.0$. For efficiency reasons, only events with a di-jet invariant mass $m_{jj} < 200\ GeV/c^2$, and only charged tracks with $p_{||} > 0.6\ GeV/c$ were considered. The measured fragmentation function $D(z)$ is shown in figure 29 [43]. Because of the steeply falling spectrum, the uncertainty on the jet momentum scale is the dominant systematic uncertainty, except for the region $z < 0.05$ where the acceptance and underlying event corrections are substantial. The tail of the fragmentation function, which goes out to $z = 1$, gives the relative probability that a jet fragments into one leading charged particle.

The Q^2-evolution of the fragmentation function is illustrated in figure 30. Shown here is the fragmentation function for six intervals in z, as function of the di-jet invariant mass, m_{jj}, which is used as an estimator of Q^2. Also plotted is the data from the e^+e^- experiment TASSO as function of the e^+e^-center of mass energy squared. As seen in section 5, QCD calculations predict logarithmic deviation from the scaling behavior, which is clearly observed. As Q^2 increases more particles

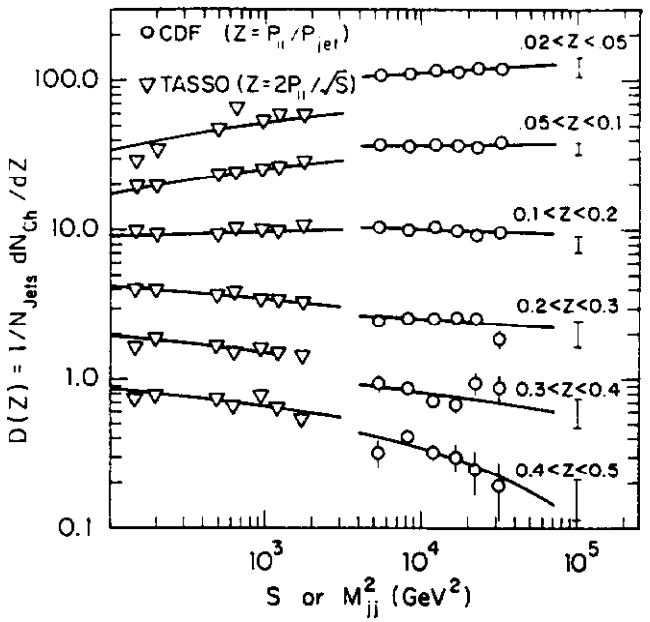

Figure 30: Evolution of the fragmentation function with m_{jj}^2 for the CDF data (o) and with s for the TASSO data ($\triangledown$). The curves are fits to the data points. Typical systematic errors for the CDF data are indicated at the right.

are observed at low z and fewer at high z, indicating a steepening of the fragmentation function with Q^2. This behavior was illustrated in figure 15. The average charged momentum fraction has been extracted from the fragmentation function to be $\langle f_{ch} \rangle = 0.65 \pm 0.02 \pm 0.08$, to be compared with the UA1 and TASSO result of $\langle f_{ch} \rangle = 0.47 \pm 0.02 \pm 0.05$ and $\langle f_{ch} \rangle = 0.58 \pm 0.02$, respectively [44, 45]. It should be noted that predominantly gluon jets are produced at the Tevatron collider at $\sqrt{s} = 1.8\ TeV$ for di-jet invariant masses $m_{jj} < 200\ GeV/c^2$ and jet transverse momenta of typically 50 GeV/c. The ratio of gluon jets to quark jets under these conditions is about 3:1.

6.4 Direct Photons

Direct photon production, $\bar{p}p \rightarrow \gamma + \mathrm{X}$, for which the two dominant processes are shown in figure 31, is of particular interest for QCD tests because it allows a direct measurement of the gluon structure function. Since the gluon structure function peaks in the low x region where the cross section is largest, the QCD Compton diagram ($qg \rightarrow \gamma q$) will dominate over the annihilation diagram ($q\bar{q} \rightarrow \gamma g$). This is fortunate since it is precisely the QCD Compton diagram that probes the gluon distribution inside the proton. Prompt photon production has experimentally several advantages over the study of jet production. First, it is possible to measure the transverse momentum of the photon in the electromagnetic calorimeter with much better accuracy than the transverse momentum of jets. Secondly, because the photon is a parton, fragmentation effects are absent. Furthermore, this process involves one coupling constant, the fine structure constant, which is very well understood. This, however, is at the same time a disadvantage. Since the production of prompt

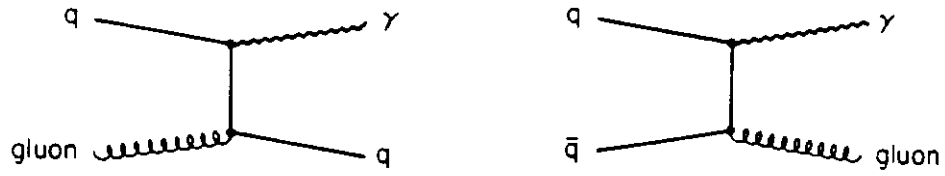

Figure 31: Dominant lowest order Feynman diagrams contributing to direct photon production.

photons involves one electromagnetic coupling, the cross section is at least two orders of magnitude lower than the inclusive jet production cross section and tails of the jet production distributions become important and can constitute a substantial background. Initial and final state bremsstrahlung are an additional source of photons that dilute the signal.

The main experimental difficulty is the separation of single γ's from multiple γ's from π^0 and η^0 decays. Both the CDF and UA2 experiment determine the π^0 background in the direct photon data sample on a statistical basis. CDF utilizes strip chambers, embedded in the electromagnetic calorimeter at approximately shower maximum, to distinguish showers originating from a single photon or from two photons on the basis of the transverse shower profile [46]. The method used by UA2 is based on measuring the number of photon conversions that occur in the preradiator [47]. This method has recently also been used by CDF. The data sample of photon candidates, being events where a conversion has occurred, consists of a signal sample of single photon events, and a background sample of π^0 conversions. The fraction of observed conversions is thus

$$\alpha = f\,\epsilon_\gamma + (1-f)\,\epsilon_\pi$$

The fraction f of direct photon candidates is then given by

$$f = \frac{\alpha - \epsilon_\pi}{\epsilon_\gamma - \epsilon_\pi}$$

Here, ϵ_γ is the conversion probability for a single photon; ϵ_π is the conversion probability for a π^0, which can be derived from ϵ_γ. These conversion probabilities are determined using a Monte Carlo.

The measured UA2 invariant inclusive cross section for prompt photon production in the region $|\eta| < 0.76$, based on an integrated luminosity of $\mathcal{L} = 7.4 \pm 0.4\ pb^{-1}$ is shown in figure 32a [47]. The cross section has been corrected of course for the background contamination. Figure 32b shows the multi-photon background fraction in the sample of direct photon candidate events as function of the photon transverse momentum. Large background fractions are incurred at low transverse momenta. The curves show the next-to-leading order QCD prediction [48] for different sets of structure functions and different choices of Q^2-scale. In general

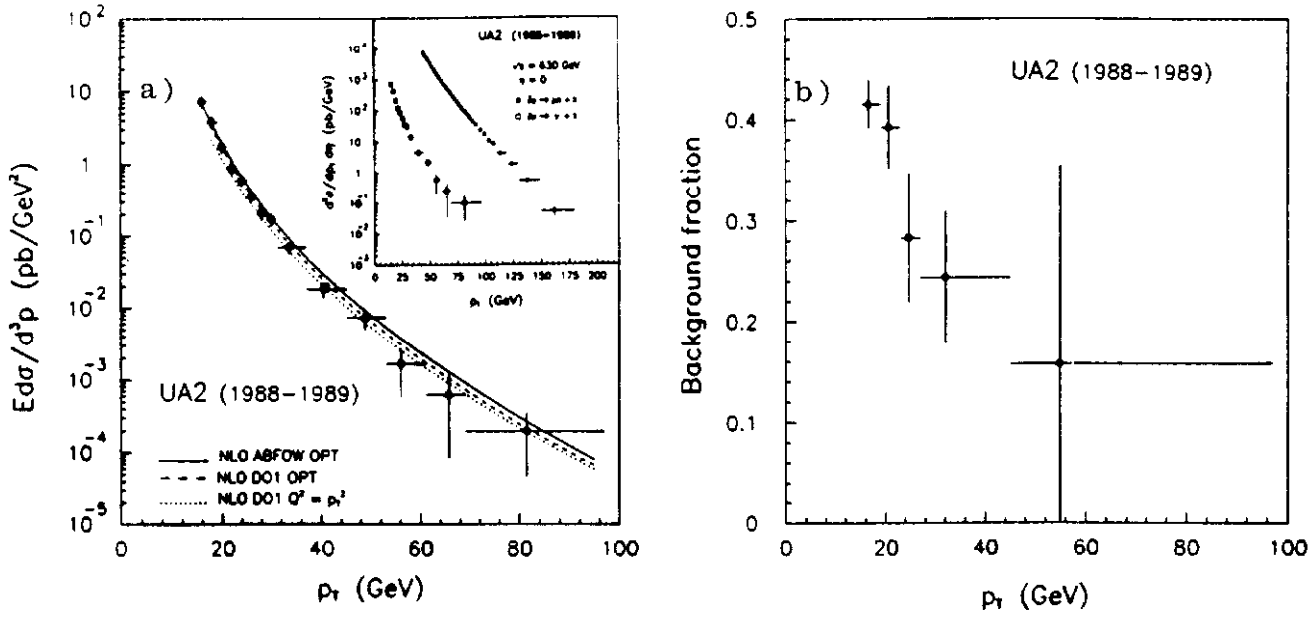

Figure 32: a) The invariant differential cross section for direct photon production in the central region ($|\eta| < 0.76$), as measured by UA2, compared with the QCD calculations. The inset shows a comparison between the differential cross section for direct photon and jet production at $\eta = 0$. b) Fractional multi-photon background contamination in the sample of direct photon candidate events.

there is good agreement between the data and the theoretical prediction. The inset in figure 32a illustrates the effect of the electromagnetic coupling constant, where the photon production cross section (lower data points) is compared with the jet-production (upper data points) at $\eta = 0$.

Figure 33 shows the sensitivity of the invariant cross section to the gluon structure function [49]. Plotted are the invariant cross sections as function of the photon pseudorapidity for a photon with transverse momentum $p_t = 10\ GeV/c$ (fig. 33a) and $p_t = 20\ GeV/c$ (fig. 33b) for different parametrizations of the gluon distribution function. The error bars indicated are the statistical errors corresponding to an integrated luminosity of 1 pb^{-1}, assuming full detection efficiency. The gluon distribution function was parametrized as

$$x\,G(x) = x^{-\epsilon}(1-x)^b$$

and the parameters ϵ and b were only allowed to vary over a range allowed by the currently available experimental data. Since the gluon distribution peaks at low x values, the greatest sensitivity to the parameters is clearly at small p_t values. At larger p_t values the sensitivity remains, given direct photons can be detected down to pseudorapidities of $|\eta| = 3$. Although removing the background from π^0 conversions and from bremsstrahlung processes will experimentally be difficult, the production of prompt photons is a promising process that can provide new insight in the small x-behavior of the gluon distribution function. The sensitivity of the prompt photon production in $\bar{p}p$ collisions to different parametrizations of the gluon distribution is competitive with the expected sensitivity at the HERA ep-collider [50].

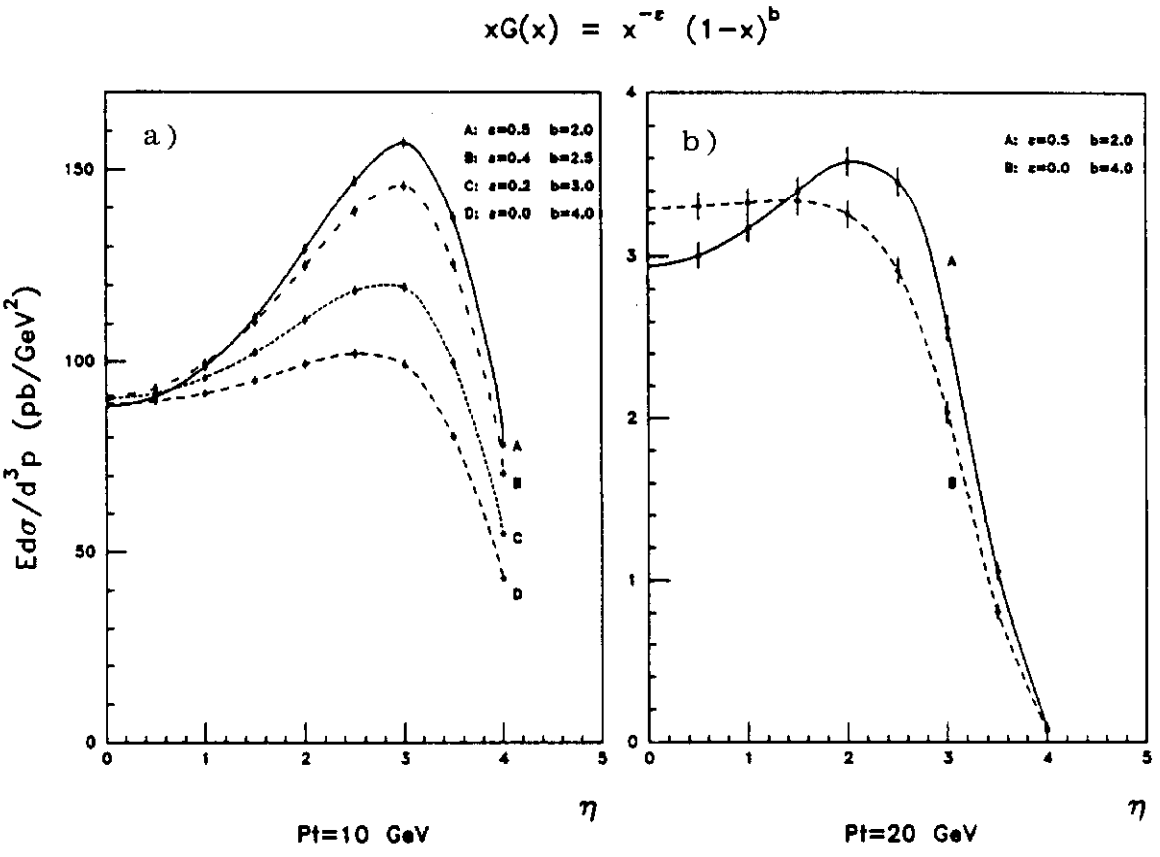

Figure 33: Invariant cross section for direct photon production as function of pseudo-rapidity for different parametrizations of the gluon distribution function for photons with (a) $p_t = 10\ GeV/c$ and (b) $p_t = 20\ GeV/c$.

6.5 Jet Mass Spectroscopy

In the standard model, the dominant decay modes of the intermediate vector bosons are the decays in quark-antiquark pairs. It is experimentally very challenging to detect this signature because of the copious QCD background and the limited energy resolution of hadron calorimeters. The UA2 collaboration has observed a signal of only 5% above the QCD background, consistent with hadronic decays of W and Z^0 bosons, with a significance of five standard deviations (fig. 34a) [51]. The signal over background ratio is plotted in figure 34b. The solid line is a double Gaussian fit to the data. The dashed line indicates the contribution from hadronic decays of W-bosons only. The two-jet mass resolution is clearly too poor to identify the W- and Z^0-mass peaks separately. At future hadron colliders jet spectroscopy will be one of the crucial experimental features and the study of hadronic decays of the intermediate vector bosons will give important information regarding the feasibility of certain studies planned with future calorimeters.

The most promising decay modes to study the intermediate vector bosons are the leptonic decay channels, which will be the topic of discussion of the next section.

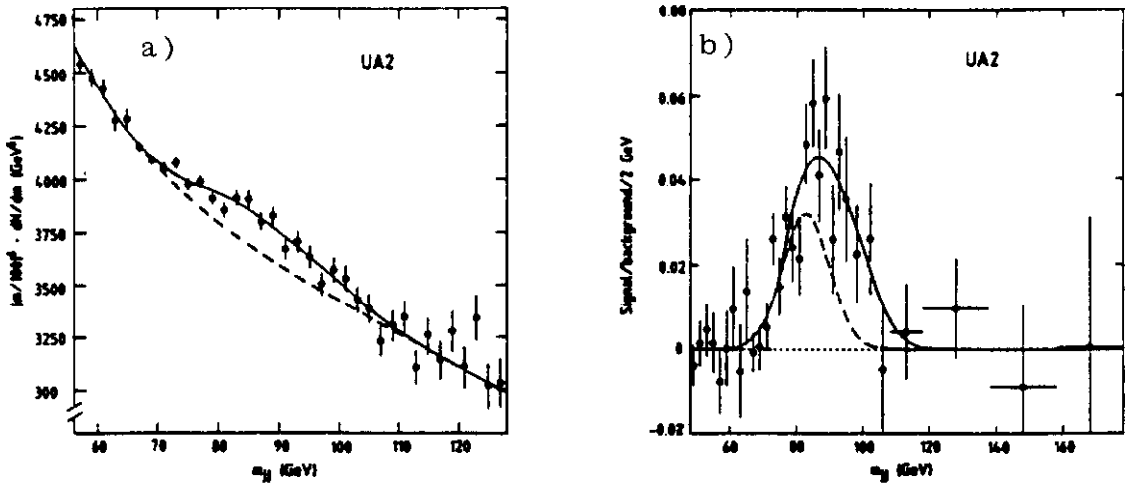

Figure 34: a) Signal of hadronic decays of W- and Z^0-bosons observed in the UA2 di-jet invariant mass spectrum. The solid line is a fit to the data assuming a double Gaussian resolution function for the hadronic W and Z^0 decays. b) Signal over background ratio. The dashed line indicates the W-contribution only.

7 Intermediate Vector Boson Physics

7.1 Theoretical Preliminaries

The study of the properties of the Intermediate Vector Bosons (IVB's) allows for precision tests of the theory of electroweak and strong interactions. The theory which, based on local gauge invariance, unifies the electromagnetic and weak interactions, is called the standard model [52]. In this model the electromagnetic and weak interactions are governed by the local symmetry group $SU(2) \times U(1)$. In analogy to the notion of (approximate) isospin invariance of the strong interactions, introduced by Heisenberg, the $SU(2)$ symmetry transformations here are called "weak isospin" rotations. Similarly, the group $U(1)$ is associated with a "weak hypercharge" operator. The four gauge fields of the group $SU(2) \times U(1)$ are identified with the three weak intermediate vector bosons $W^{\pm}$ and Z^0, carriers of the weak force, and the photon, the carrier of the electromagnetic force.

Since mass terms cannot be introduced in the Lagrangian in a gauge invariant way, masses for the gauge bosons are generated through the so-called Higgs mechanism, whereby the $SU(2) \times U(1)$ symmetry is spontaneously broken by the introduction of complex scalar fields which acquire a non-vanishing vacuum expectation value. The transformation from weak interaction eigenstates to mass eigenstates through diagonalization of the mass matrices mixes the different quark flavors. This mixing is described by the unitary Cabibbo-Kobayashi-Maskawa (CKM) matrix. Since neutrino's are (still?) massless, there is no flavor mixing in the lepton sector.

After spontaneous symmetry breaking and mass diagonalization, the interaction Lagrangian for the fermions can be written as a sum of a neutral current and a charged current Lagrangian. The interactions with the intermediate vector bosons contain both a vector and an axial vector coupling. In the charged current sector, both couplings have the same strength. Their respective coupling strengths

with the neutral vector bosons are given by

$$g_V^f = I_3 - 2\,Q_f \sin^2\vartheta_w \tag{22}$$

$$g_A^f = I_3 \tag{23}$$

where I_3 is the third component of the weak isospin and Q_f the charge of the fermion. Since left-handed leptons and quarks are assigned to $SU(2)$ doublets, I_3 is $+\frac{1}{2}$ for neutrino's and charge $\frac{2}{3}$ quarks and $-\frac{1}{2}$ for the electron, muon and tau-lepton and the charge $-\frac{1}{3}$ quarks.

In order to increase the experimental signal over the background, all experiments initially study the weak intermediate vector bosons through their leptonic decays. The branching ratio for decay into leptons, however, is comparatively small. The decay width for the Z^0-boson into leptons and quarks is given by

$$\Gamma(Z^0 \to \ell^+\ell^-) = \frac{G_F\,M_Z^3}{6\pi\sqrt{2}}\,(g_V^{\ell\,2} + g_A^{\ell\,2}) \tag{24}$$

$$\Gamma(Z^0 \to q\bar{q}) = 3\,\frac{G_F\,M_Z^3}{6\pi\sqrt{2}}\,(g_V^{q\,2} + g_A^{q\,2})\left(1 + \frac{\alpha_s(m_Z)}{\pi}\right) F_{q\bar{q}} \tag{25}$$

The term $(1 + \alpha_s/\pi)$ is a QCD correction factor and $F_{q\bar{q}}$ takes into account phase-space suppression for massive quarks. The factor 3 in equation 25 arises from the three color degrees of freedom of the quarks. Using the expressions for g_V^f and g_A^f given in equations 22, 23 and the measured Z^0 total decay width, $\Gamma_Z = 2.55\ GeV$, one can readily show that the branching ratio for Z^0's decaying into an electron-positron pair is about 3%.

The decay width of $W^\pm$-bosons into leptons is given by

$$\Gamma(W \to \ell\nu) = \frac{G_F\,M_W^3}{6\pi\sqrt{2}} \tag{26}$$

Since the coupling strengths for the vector and axial vector couplings have the same strength for all fermions in the charged current sector ($g_V = g_A = 1$) the ratio of the decay width into quarks and leptons includes only the appropriate quark mixing matrix element (cf. eq. 25)

$$\frac{\Gamma(W \to q\bar{q}')}{\Gamma(W \to \ell\nu)} = 3\,|V_{q\bar{q}'}|\left(1 + \frac{\alpha_s(M_W)}{\pi}\right) F_{q\bar{q}'} \tag{27}$$

Using equations 26 and 27 the W-leptonic branching ratio can be determined easily. A much quicker way to get an estimate of the branching ratio is to look at the number of available decay channels for the W-boson. If the top quark is heavier than the W-boson and approximating the CKM-matrix by a diagonal unitary matrix, *i.e.* $V_{ud} = V_{cs} = 1$, there are only two hadronic decay channels for the W: $W \to u\,d$, $W \to c\,s$. Ignoring the two correction factors in equation 27, it immediately follows

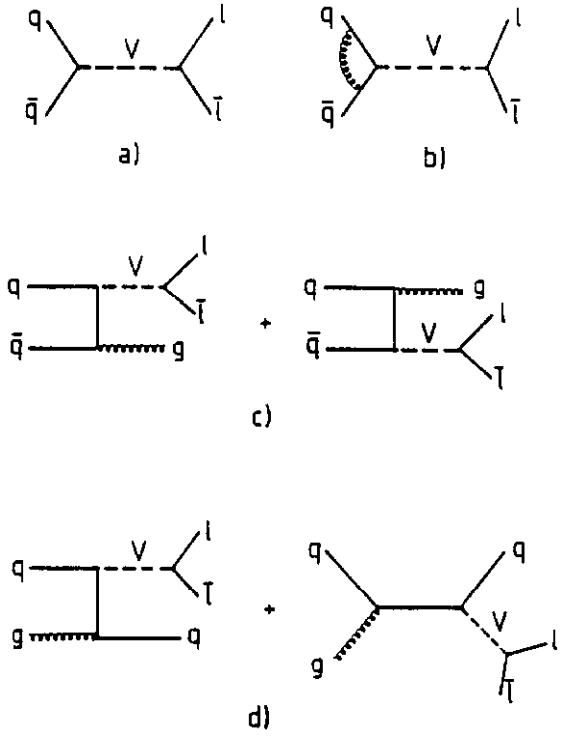

Figure 35: Feynman diagrams to lowest order for producing intermediate vector bosons.

from this equation that the partial decay branching ratio for each of the three leptonic decay modes of the W-boson is $\frac{1}{9}$.

Figure 35 shows the lowest order Feynman diagrams for the production of IVB's. The IVB's are produced through $q\bar{q}$ annihilation and therefore have no transverse momentum in lowest order (fig. 35a). Higher order QCD processes generate the IVB transverse momentum. The production of Z^0-bosons at $\bar{p}p$ colliders is the time reversed process of Z^0-production at LEP, convoluted with the parton distribution functions. The essential characteristics of this process in $\bar{p}p$ collisions are similar to production in e^+e^- collisions and are discussed in the lectures on LEP physics at this school.

The production and subsequent leptonic decay of $W^\pm$-bosons is governed by helicity conservation and its spin 1 nature. Since the W's are produced from the fusion of a left-handed quark and a right-handed antiquark, the W's are almost fully polarized along the antiproton direction, as indicated in figure 36. Consequently, the positron (electron) from the W^+ (W^-) decay will be emitted preferentially along the antiproton (proton) direction. The angular distribution of the W^+-decay lepton from W^+-production through $u\bar{d}$-fusion is given by

$$\begin{aligned} \frac{d\hat{\sigma}}{d\cos\vartheta^*} &= \frac{|V_{ud}|^2}{8\pi}\left(\frac{G_F M_W^2}{\sqrt{2}}\right)^2 \frac{\hat{s}\,(1+\cos\vartheta^*)^2}{(\hat{s}-M_W^2)^2+(\Gamma_W M_W)^2} \\ &= \frac{3}{8}\,\hat{\sigma}\,(1+\cos\vartheta^*)^2 \end{aligned} \tag{28}$$

where ϑ^* is the angle between the outgoing positron and the incoming $\bar{d}$-quark. The

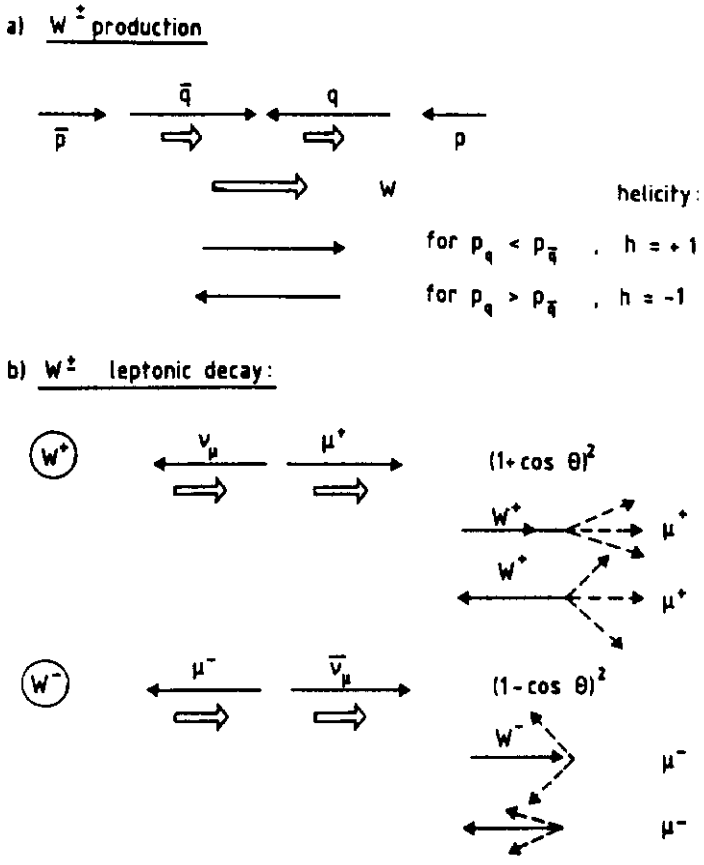

Figure 36: (a) $W^{\pm}$ production: polarization of the $W^{\pm}$ due to the V-A coupling; (b) $W^{\pm}$ leptonic decay: preferred direction of the decay leptons.

V-A coupling of the W-bosons to the leptons is reflected in the strongly asymmetric $(1+\cos\vartheta^*)^2$ angular dependence.

Since the decay of W-bosons involves neutrinos, which escape detection, the presence of neutrinos is inferred from a large momentum imbalance. Now, any collider detector has by necessity openings in the forward and backward regions to allow the particle beams to enter the device and no collider detector is capable of measuring the total energy flow in the beam directions. Moreover, in hadron collisions the remnants of the initial proton and antiproton carry a large fraction of the initial momentum and escape along the beam pipe. The common technique therefore to detect neutrinos is to look for a large missing transverse momentum. Since the longitudinal momentum of the neutrino is not measured directly, there is always an ambiguity when boosting to the W-rest frame and thus an ambiguity in the angle ϑ^*. The angle ϑ^* is thus not the optimal variable for the study of the production properties of W-bosons. Much more suited is the transverse momentum of the decay lepton. In lowest order, when the W-boson has no transverse momentum, the relation between the transverse momentum and the angle ϑ^* is given by

$$\hat{p}_t^2 = \frac{1}{4}\,\hat{s}\,\sin^2\vartheta^*$$

Making the coordinate transformation from ϑ^* to p_t involves the Jacobian transfor-

mation

$$\frac{d\cos\vartheta^*}{d\hat{p}_t^2} = -\frac{2}{\hat{s}}\left(1-\frac{4\hat{p}_t^2}{\hat{s}}\right)^{-\frac{1}{2}} \tag{29}$$

Since angles ϑ^* and $\pi-\vartheta^*$ contribute to the same $\hat{p}_t$, terms linear in $\cos\vartheta^*$ cancel and the lepton p_t spectrum is given by

$$\frac{d\hat{\sigma}}{d\hat{p}_t^2} = \frac{\hat{\sigma}}{\hat{s}}\frac{3}{2}\frac{1-2\hat{p}_t^2/\hat{s}}{(1-4\hat{p}_t^2/\hat{s})^{\frac{1}{2}}} \tag{30}$$

This cross section diverges at $\hat{p}_t = \frac{1}{2}\sqrt{\hat{s}}$. The divergence comes from the Jacobian transformation and is called the Jacobian peak. When integrating equation 30 over $\hat{s}$ the Breit-Wigner removes the singularity but leaves a sharp peak at $\hat{p}_t = \frac{1}{2}\sqrt{\hat{s}}$. Higher order QCD corrections, which give the W a transverse momentum, smear out this peak a bit more.

The mass of the W-boson can be determined using the p_t spectrum of either the decay lepton or the neutrino. The quantity which is least sensitive to the p_t of the W, and thus better suited for measuring the W-mass [53], is the transverse mass defined as

$$m_t^2 = (p_t^\ell + p_t^\nu)^2 = 2\,|\vec{p}_t^{\,\ell}|\,|\vec{p}_t^{\,\nu}|\,(1-\cos\varphi^{\ell\nu}) \tag{31}$$

where $\varphi^{\ell\nu}$ is the azimuthal angle between the decay lepton and the neutrino.

7.2 IVB Identification and Partial Production Cross Sections

In the lepton detection for W and Z events all experiments apply similar cuts aimed at finding high p_t isolated leptons. The main background to electrons comes from jets which fragment into a leading π^0 and from π^0's that overlap with charged pions. Also photon conversions can result in fake electron candidates. The UA2 experiment, which has excellent electron identification, applies only calorimetric cuts in the first stage of their electron identification. They require in the first step of the electron selection an electromagnetic cluster and only apply a cut on the cluster radius and the leakage of the shower into the hadronic compartment. Figure 37 shows the di-electron invariant mass spectrum for the Z^0-sample after this first stage of electron identification [54]. The mass peak at the Z^0-mass is clearly visible. The background is mainly QCD background and a small fraction of Drell-Yan events. In the second stage the cuts are more refined: the lateral as well as transverse shape of the shower is required to be consistent with electrons as determined from test beams. Moreover, track-calorimeter and track-preshower cluster matching is required. Figure 38a shows the di-electron invariant mass distribution for the final data sample of 169 events obtained by UA2 for the determination of the production cross section, based on a total integrated luminosity of $7.4\pm0.4\ pb^{-1}$. In the selection of this data sample strict selection criteria were applied to one electron and looser criteria to the other electron leg.

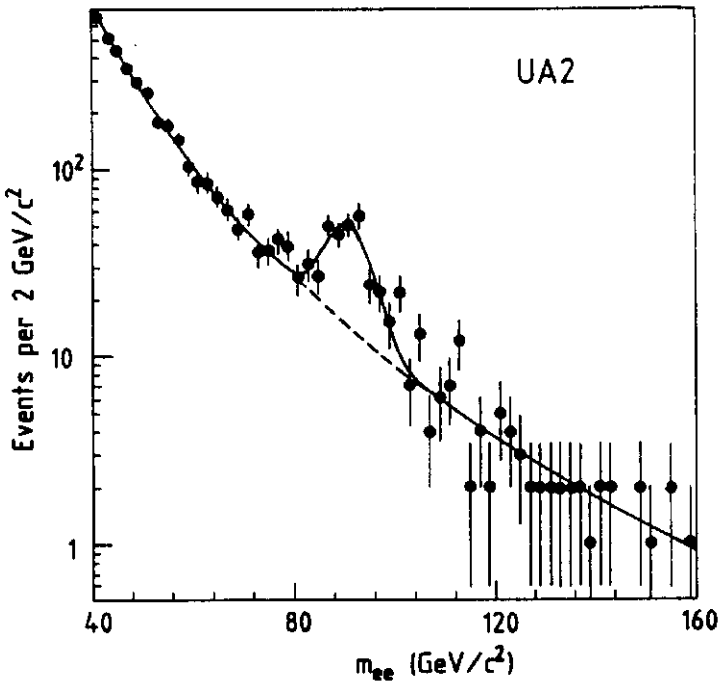

Figure 37: UA2 invariant mass spectrum for pairs of electromagnetic cluster in the calorimeter. The solid line is a fit to an exponentially falling QCD background and a Gaussian resonance.

Figure 38b shows the di-muon invariant mass distribution of the $Z^0 \rightarrow \mu^+\mu^-$ data sample of UA1 [55]. This sample consists of 52 events obtained with an integrated luminosity of 4.6 pb^{-1}. Muon events in UA1 are selected by requiring a high quality track, isolated in both the central detector and the calorimeter, and a matching track in the muon chambers. Isolation in the central detector is defined as the sum of the transverse momenta of all charged tracks in a cone $\Delta R = \sqrt{\Delta\eta^2 + \Delta\varphi^2} = 0.4$ around the muon direction to be less than 1 GeV/c. The isolation requirement on the calorimeter requires the total transverse energy in a cone of $\Delta R = 0.7$ around the muon direction not to exceed 5 GeV.

It is obvious from figure 38 that the mass resolution for the muon decay channel is much worse than for the electron channel. This is true in general for hadron collider experiments. Recall that the invariant mass of the di-lepton system is given by

$$m^2_{\ell_1\ell_2} = 4\, E_{\ell_1}\, E_{\ell_2}\, \sin^2 \alpha/2$$

where α is the angle between the two leptons. The mass resolution σ_m can then be estimated from the accuracy with which the energies and directions of the leptons are measured, $\sigma_{E_{\ell_1}}, \sigma_{E_{\ell_2}}, \sigma_\alpha$:

$$\frac{\sigma_m}{m} = \frac{1}{2}\sqrt{\left(\frac{\sigma_{E_{\ell_1}}}{E_{\ell_1}}\right)^2 + \left(\frac{\sigma_{E_{\ell_2}}}{E_{\ell_2}}\right)^2 + \left(\frac{\sigma_\alpha}{\tan(\alpha/2)}\right)^2}$$

Since the direction of charged particles is measured quite accurately in tracking devices, the error on the mass resolution due to the error on α is negligible. Electron

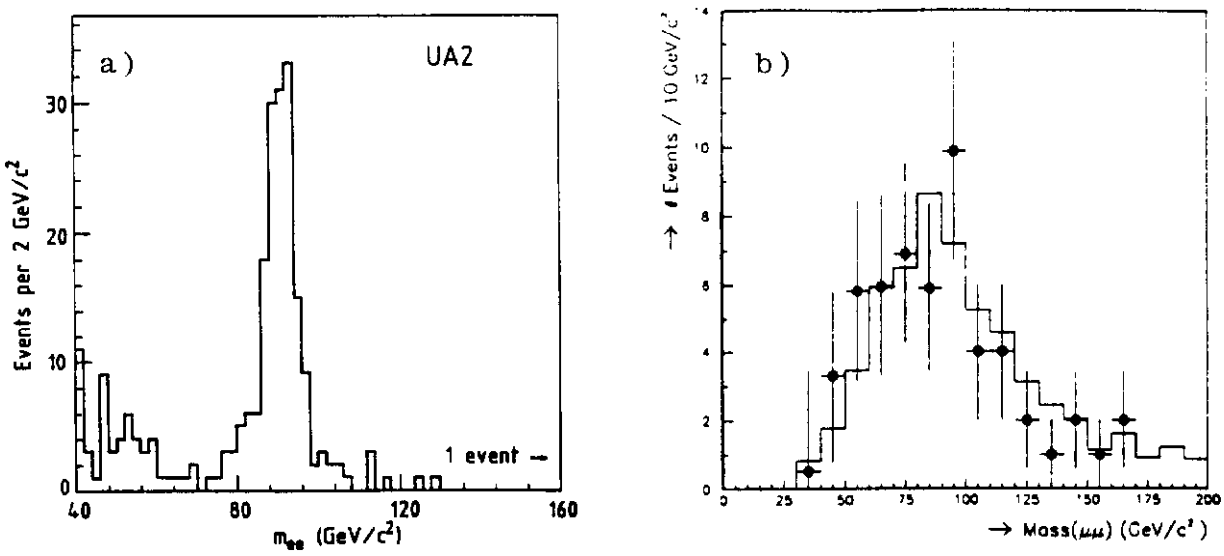

Figure 38: Invariant mass spectrum of (a) electron pair candidate events of the UA2 Z^0-data sample, (b) muon pair candidate events of the UA1 Z^0-data sample.

energies are measured with a resolution of $\sigma_E/E \approx 0.15/\sqrt{E}$, while the muon momentum resolution is typically $\sigma_p/p \approx 0.5\%\, p$ (p in GeV/c) for UA1. The respective mass resolution is thus

$$\begin{aligned} \frac{\sigma_m}{m} &\approx \frac{0.15}{\sqrt{m}} && \text{electrons} \\ &\approx 1.8 \times 10^{-3}\, m && \text{muons} \end{aligned}$$

with m in GeV/c^2. For an invariant mass m of 90 GeV/c^2 the mass resolution for the electron decay channel is $\sigma_m \approx 1.4\ GeV/c^2$, while for the muon channel the resolution is an order of magnitude worse, $\sigma_m \approx 14\ GeV/c^2$. Furthermore, the resolution increases linearly with m for the muon channel, whereas for electrons it decreases as $1/\sqrt{m}$, showing the superiority of the electron channel. For the CDF detector the momentum resolution is much better, $\sigma_{p_t}/p_t = 0.11\%\, p_t$ (p_t in GeV/c^2) [57], and for the muon decay channel the Z^0-boson mass can be determined with an accuracy comparable to the one achieved using the electron channel. The most precise measurement of m_Z still comes from the electron calorimetric measurement, though.

In contrast to the selection of Z^0-events, which is based on the identification of two isolated high p_t leptons, the detection of the decay of the W-boson, $W^\pm \to \ell^\pm \nu$, is based on a very different method, because the neutrino escapes detection. The production of a neutrino is inferred from an apparent p_t imbalance in the event

$$\vec{p}_t^{\,\nu} = \vec{\not{p}}_t = -\sum_i E_t^i \hat{n}_i \tag{32}$$

where E_t^i is the transverse energy in the i^{th} calorimeter cell and $\hat{n}_i$ a unit vector pointing from the vertex in the direction of the center of the i^{th} calorimeter cell (cf. eq. 13).

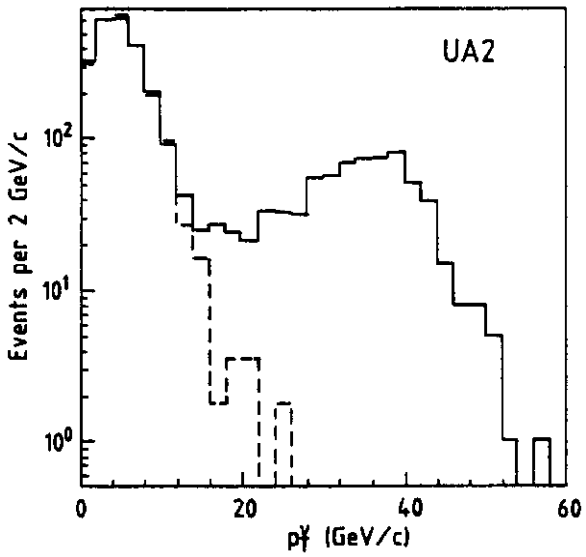

Figure 39: Distribution of p_t^{ν} of the W-candidate event sample, requiring one electron candidate with $p_t^e > 20\ GeV/c$. The dashed curve is the estimated QCD background.

A good measurement of $\vec{p}_t^{\,\nu}$ requires calorimetry down to small polar angles and good knowledge of its response, especially its low energy response. The resolution on the missing transverse momentum is parametrized by

$$\frac{dN}{d\not{p}_t^2} \propto \frac{1}{\Delta^2} \exp\left(-\frac{\not{p}_t^2}{\Delta^2}\right) \tag{33}$$

The parameter Δ depends on the total transverse energy in the event and is well parametrized by $\Delta = \alpha\,(E_t)^{\beta}$. The reported values for the parameters α and β for UA1, UA2 and CDF are, ($\alpha = 0.7, \beta = 0.5$), ($\alpha = 0.8, \beta = 0.4$) and ($\alpha = 0.7, \beta = 0.5$), respectively [58, 59, 60]. Figure 39 shows the p_t^{ν} spectrum of the UA2 inclusive electron sample, retaining only electrons with a $p_t > 20\ GeV/c$ [54]. The Jacobian peak at large p_t^{ν} is clearly visible, whereas the region of low p_t^{ν} is dominated by fake electrons from QCD background events. The missing p_t resolution is clearly not good enough to separate the W-events and the background into two distinct classes. The background in the W-signal region is estimated using a sample of events dominated by γ's from the decay of high p_t π^0's and normalizing its missing p_t spectrum to the p_t^{ν} spectrum of the W-candidate sample for $p_t^{\nu} < 10\ GeV/c$. Because the QCD background tends to peak at low values of the transverse mass, its background was found to be negligible after applying the final kinematic selection criteria for W-events, which were $p_t^e > 20\ GeV/c$, $p_t^{\nu} > 20\ GeV/c$ and $m_t > 40\ GeV/c^2$. The dominant background in the final sample of 2041 events, was the decay $W \to \tau\nu_\tau \to e\nu_e\nu_\tau\nu_\tau$, estimated to be 3.8%.

Since the IVB's are detected through their leptonic decays, the product of the total production cross section and the leptonic branching ratio is measured

$$\begin{aligned} \sigma_Z^{\ell} &= \sigma(\bar{p}p \to Z^0 + X) \cdot BR(Z^0 \to \ell^+\ell^-) \\ \sigma_W^{\ell} &= \sigma(\bar{p}p \to W^{\pm} + X) \cdot BR(W^{\pm} \to \ell^{\pm}\nu_\ell) \end{aligned}$$

Exp.	$\sigma_Z^{\mu} \cdot$ B (pb)			$\sigma_W^{\ell} \cdot$ B (pb)	
UA1	$\sigma_Z^{\mu\mu}$	$58.6 \pm 7.8 \pm 8.4$	UA1	σ_W^{μ}	$609 \pm 41 \pm 94$
	σ_Z^{ee}	$74 \pm 14 \pm 11$		σ_W^{e}	$630 \pm 50 \pm 100$
				σ_W^{τ}	$630 \pm 130 \pm 120$
UA2	σ_Z^{ee}	$65.6 \pm 4.0 \pm 3.8$	UA2	σ_W^{e}	$682 \pm 12 \pm 40$
	$\sigma_Z^{\tau\tau}$	$121\ ^{+69}_{-43} \pm 10$			
CDF	σ_Z^{ee}	$209 \pm 13 \pm 17$	CDF	σ_W^{e}	$2190 \pm 40 \pm 210$

Table 1: Intermediate vector boson partial production cross sections.

These partial production cross sections are determined from the rate of observed events, the measurement of the integrated luminosity and the knowledge of the lepton detection efficiency and detector acceptance. Table 1 lists the production cross sections as measured by all three collider experiments. Figure 40 shows their dependence on center of mass energy. The solid line in the figure is the first order QCD prediction [61]; the dashed lines indicate the theoretical uncertainty. Since the quantity that is measured is the product of the total production cross section and the leptonic branching ratio, the theoretical prediction depends on the mass of the top quark. If the mass of the top quark increases, the production cross section will increase due to the larger available phase space for the leptons. The calculation shown in figure 40 has been carried out assuming a top quark mass of $m_t = 40\ GeV/c^2$. The data clearly favors a higher mass for the top quark. Recently a calculation of the IVB production cross section to full second order has become available [62]. Although the second order contribution increases the cross section by about 10%, the data still prefers a top quark mass higher than 50 GeV/c^2. Due to the large errors on the measured cross sections no stringent limits on the top quark mass can be set, though.

Ratios of measured quantities are always very attractive since many of the experimental errors and sometimes even the theoretical uncertainties cancel. Using the measured IVB production cross sections two kinds of ratios can be formed: *i*) the ratio of the production cross section for the W- and Z^0-boson and their subsequent decay into a specific lepton flavor, and *ii*) the ratio of the IVB partial production cross sections for their various decay modes. The former gives a measurement of the W total decay width, Γ_W; the latter allows to check lepton universality in both the charged and neutral current sector.

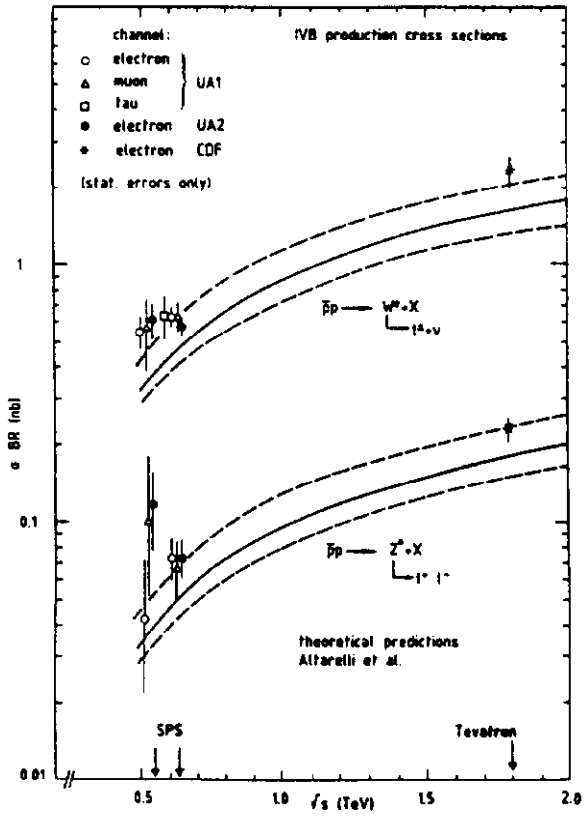

Figure 40: Intermediate vector boson partial production cross sections in $\overline{p}p$ collisions. Only statistical errors are shown. The solid lines indicate the theoretical predictions calculated to first order in α_s, assuming a top quark mass of 40 GeV/c^2. The dashed lines represent the uncertainty on the theoretical predictions.

The ratio of the W- and Z^0-partial production cross sections, R, is defined as

$$R = \frac{\sigma_W^\ell}{\sigma_Z^\ell} = \frac{\sigma(\overline{p}p \to W^\pm + X)}{\sigma(\overline{p}p \to Z^0 + X)} \frac{\Gamma(W^\pm \to \ell^\pm \nu_\ell)}{\Gamma(Z^0 \to \ell^+\ell^-)} \frac{\Gamma(Z)}{\Gamma(W)} \tag{34}$$

In taking the ratio not only the experimental but also the theoretical uncertainties largely cancel. Hence, the available Z^0 statistics limits the precision on R, which has been measured by the three experiments to be [55, 54, 56, 63]

$$\begin{aligned} R^e &= 9.1\ ^{+1.7}_{-1.2} && \text{UA1} \\ R^\mu &= 10.4\ ^{+1.8}_{-1.8} \pm 0.8 && \text{UA1} \\ R^e &= 10.4\ ^{+0.7}_{-0.6} \pm 0.3 && \text{UA2} \\ R^e &= 10.2 \pm 0.8 \pm 0.4 && \text{CDF} \end{aligned}$$

The first two terms in equation 34 do not depend on the mass of the top quark. The dependence on the top quark mass and on the number of neutrino species comes in through total decay width of the W and Z^0. Figure 41 shows the dependence of R on the top quark mass for the case there are three and four light neutrino species. One should note the "kinks" in the prediction for R at the values $m_t = \frac{1}{2}m_Z$ and $m_t = m_W - m_b$ due to the change in available total phase space for the lepton decay channels of the Z^0- and W-boson, respectively. The gray band indicates the

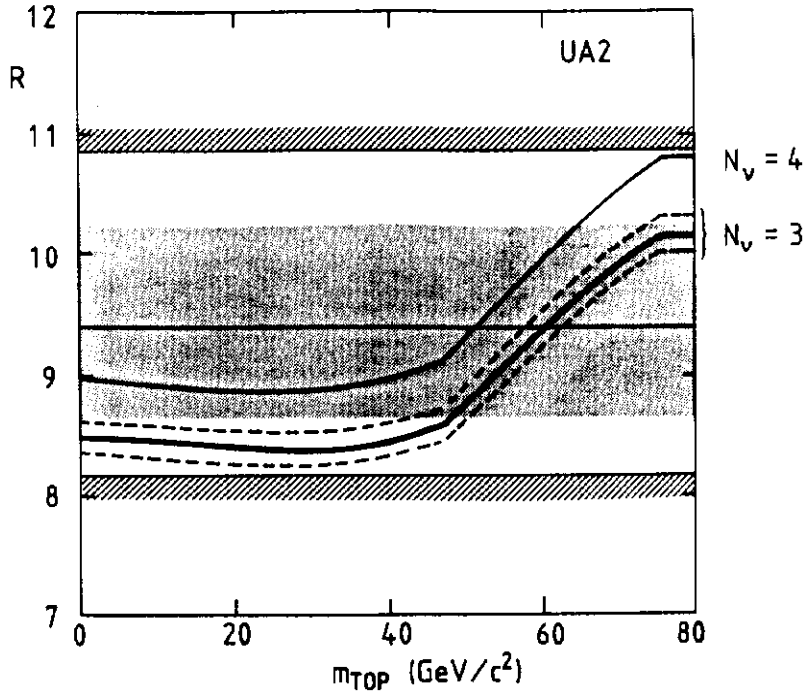

Figure 41: Comparison of the ratio of the W and Z partial production cross section, R, as measured by UA2, and the standard model prediction as function of the top quark mass. The shaded band represents the 1σ confidence interval on the measurement; the hatched regions are excluded at 90% confidence level. The solid lines correspond to the predicted R value assuming three or four light neutrinos, respectively. The dashed lines indicate the uncertainty due to the structure functions.

one sigma UA2 measurement. Though not conclusive because of the limited Z^0 statistics, the measurements of R also seem to prefer a heavy t-quark.

Using the measured total width of the Z^0-boson at LEP, the measurement of R gives a direct measurement of the total width of the W, as equation 34 shows. Figure 42 shows the dependence of Γ_W on m_t together with the world average value of $\Gamma_W = 2.12 \pm 0.12\ GeV$ [55]. The world average is in good agreement with the standard model prediction of $\Gamma_W = 2.07\ GeV$, for top quark masses greater than the W-mass. Using the measured value for Γ_W a lower limit on the top quark mass of 51 GeV/c^2 can be set, independent of its modes of decay. One should note that the measurement of Γ_W is a window for objects with a mass $\frac{1}{2}m_Z < m_X < m_W$ regardless of their decay modes, as long as they couple to W's.

The ratios of the partial production cross sections for the various W and Z^0 decay modes provide a test of lepton universality of the weak charged and neutral couplings at $Q^2 = M^2_{IVB}$. Defining the weak charged and neutral coupling constants as g_i and k_i, respectively, one has

$$\left(\frac{g_i}{g_j}\right)^2 = \frac{\sigma_W \cdot BR(W^\pm \to \ell_i^\pm \nu_i^\ell)}{\sigma_W \cdot BR(W^\pm \to \ell_j^\pm \nu_j^\ell)} = \frac{\Gamma(W^\pm \to \ell_i^\pm \nu_i^\ell)}{\Gamma(W^\pm \to \ell_j^\pm \nu_j^\ell)} \tag{35}$$

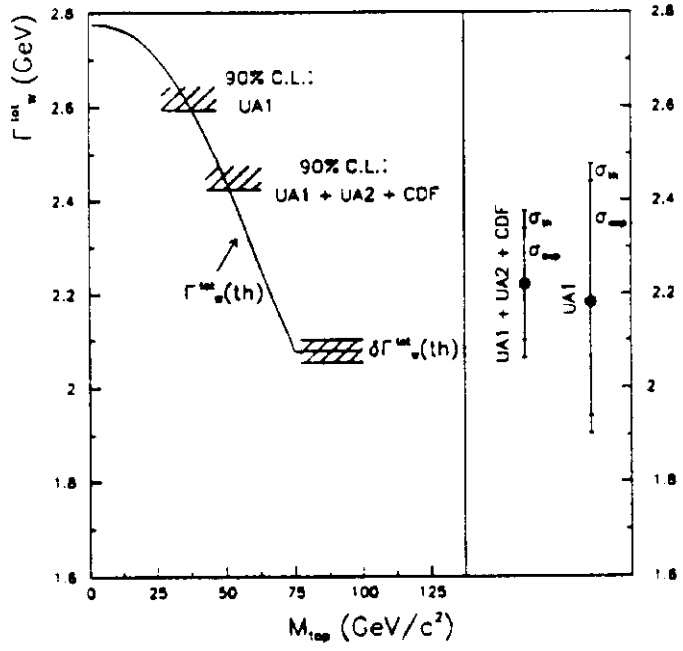

Figure 42: Dependence of Γ_W on m_{top}. Indicated is the 90% confidence limit on the top quark mass derived from the UA1 measurement alone and from the weighted average of the UA1, UA2 and CDF measurements.

$$\left(\frac{k_i}{k_j}\right)^2 = \frac{\sigma_Z \cdot BR(Z^0 \to \ell_i^+ \ell_i^-)}{\sigma_Z \cdot BR(Z^0 \to \ell_j^+ \ell_j^-)} = \frac{\Gamma(Z^0 \to \ell_i^+ \ell_i^-)}{\Gamma(Z^0 \to \ell_j^+ \ell_j^-)} \tag{36}$$

The results for g_i and k_i obtained by the UA1 and UA2 experiments are [63, 64]

$$\begin{aligned} g_\mu/g_e &= 1.00 \pm 0.07 \pm 0.04 && \text{UA1} \\ g_\tau/g_e &= 1.01 \pm 0.10 \pm 0.06 && \text{UA1} \\ k_\mu/k_e &= 1.02 \pm 0.15 \pm 0.04 && \text{UA1} \\ g_\tau/g_e &= 0.997 \pm 0.056 \pm 0.042 && \text{UA2} \end{aligned}$$

These measurements support lepton universality in IVB decays to a level better than 15%.

7.3 W Longitudinal Momentum Distribution

The longitudinal momentum distribution of the IVB's is expected to reflect the structure functions of the incoming annihilating quarks. The W fractional longitudinal momentum, $x_W \equiv 2p_L^W/\sqrt{s}$, is equal to the difference between the fractional momenta x_q and $x_{\bar{q}}$ of the two annihilating partons. It is determined by the vector sum of the longitudinal momenta of the decay leptons in the same way as indicated in equation 18. Although the longitudinal momentum of the neutrino is not known, it can be inferred by imposing the W-mass on the lepton-neutrino system:

$$m_W^2 = (E_\ell + E_\nu)^2 - (\vec{p}_\ell + \vec{p}_\nu)^2 \tag{37}$$

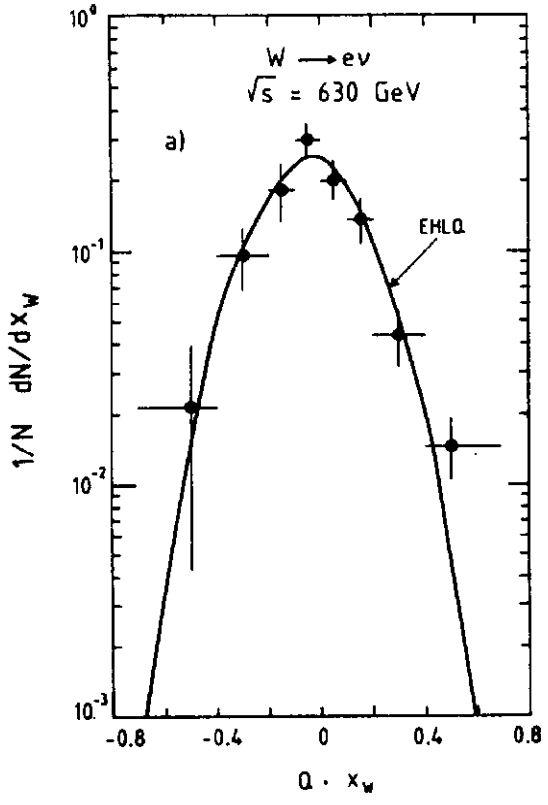

Figure 43: Distribution of the measured UA1 $Q \cdot x_W$ distribution for the $W \rightarrow e\nu$ data sample. The solid line is the theoretical prediction using the EHLQ structure functions.

This quadratic equation gives two solutions for the neutrino longitudinal momentum. For about half the events at center of mass energies of 630 GeV there is a unique value for the Feynman x of the W, as either one of the two solutions is unphysical ($|x_W| > 1$), or both solutions give the same value for x_W. In the remaining cases there is a two-fold ambiguity and the solution for x_W is chosen by convention. The UA1 collaboration retains the p_L^ν solution which gives the smallest total energy imbalance in the event.

Since the W^+ (W^-) is produced by $u\bar{d}$ ($\bar{u}d$) fusion, the x_W distribution is expected to be asymmetric as far as the u and d momentum distributions differ. In figure 43 is plotted the quantity $Q \cdot x_W$ as measured by UA1 [63], where Q is the sign of the charge of the W boson. x_W is taken to be positive along the antiproton direction. Events with $Q \cdot x_W < 0$ then correspond to W production where the fractional momentum of the u ($\bar{u}$) quark is larger than that of the d ($\bar{d}$) quark. The converse is true for the $Q \cdot x_W > 0$ region. The data clearly exhibits an asymmetry, indicating that the u quark distribution is harder than the d quark distribution as expected (cf. fig. 14). From the energy conservation relations, equations 17 and 18, and the known W charge, the x_u and x_d distribution functions can be disentangled. The UA1 collaboration has determined the mean values of the u and d distribution functions to be $\langle x_u \rangle = 0.17 \pm 0.01$ and $\langle x_d \rangle = 0.13 \pm 0.01$ [63].

7.4 IVB Angular Distribution

As discussed in subsection 7.1, the angular distribution of the W decay leptons is expected to exhibit a pronounced angular asymmetry due to the pure V-A coupling of the charged currents. The angular distribution of the lepton of the decay of the W-boson in the W-rest frame has the form $d\hat{\sigma}/d\cos\vartheta^* \propto (1+\cos\vartheta^*)^2$, where ϑ^* is the angle between the outgoing positively (negatively) charged lepton and the antiproton (proton) direction in the W-rest frame (cf. eq. 28). Due to higher order QCD processes, W's are produced with a momentum transverse to the beam direction. This implies that the p and $\overline{p}$ are not collinear in the W-rest frame and that the quark directions are not the p or $\overline{p}$ direction. In this case the Collins-Soper convention [65] is used, in which ϑ^* is measured with respect to the average of the p and $\overline{p}$ direction in the W-rest frame. A further complication arises in the determination of the angle ϑ^* because of the ambiguity in the Lorentz boost to the W-rest frame. As discussed in the previous section, the longitudinal momentum of the neutrino, needed for the Lorentz transformation, is inferred by imposing the W-mass on the lepton-neutrino system. The solution yielding the minimal total energy imbalance in the event is retained and is used for the boost to the W-rest frame. Figure 44 shows the W-decay angular distribution as function of $Q\cdot\cos\vartheta^*$, as measured by UA1 [63]. Q here is the charge of the W-boson. There is good agreement with the expected $(1+\cos\vartheta^*)^2$ behavior. The slight excess of events near -1 is compatible with a small sea-sea contribution, which is about 2-4% at $\sqrt{s} = 630\ GeV$. At Tevatron energies the sea-sea contribution, which has the opposite asymmetry, rises to about 10%.

The production of Z^0-bosons is identified through their decay in a pair of leptons. In $\overline{p}p$ collisions lepton pairs are produced through virtual photon and Z^0-exchange, and real Z^0-production, very similar to the situation at e^+e^- colliders. Because of the $\gamma - Z^0$ interference the angular distribution has a term linear in $\cos\vartheta^*$

$$\frac{d\hat{\sigma}}{d\cos\vartheta^*} \propto (1+\cos^2\vartheta^*)(1+F_1(\hat{s})) + F_2(\hat{s})\cos\vartheta^*$$

which causes a forward backward asymmetry defined as

$$A_{FB} = \frac{\int_0^1 \frac{d\sigma}{d\cos\vartheta^*} d\cos\vartheta^* - \int_{-1}^0 \frac{d\sigma}{d\cos\vartheta^*} d\cos\vartheta^*}{\int_0^1 \frac{d\sigma}{d\cos\vartheta^*} d\cos\vartheta^* + \int_{-1}^0 \frac{d\sigma}{d\cos\vartheta^*} d\cos\vartheta^*}$$

It is obvious that the parameters F_1 and F_2, which are a function of the parton center of mass energy, depend on the vector and axial-vector couplings of the fermions (see section 7.1). The measurement of the angular distribution is thus sensitive to the value of $\sin^2\vartheta_w$.

In order to compare the experimental angular distribution with the theoretical prediction, the parton cross sections need to be convoluted with the parton distribution functions. One should note that, in contrast to the e^+e^- situation,

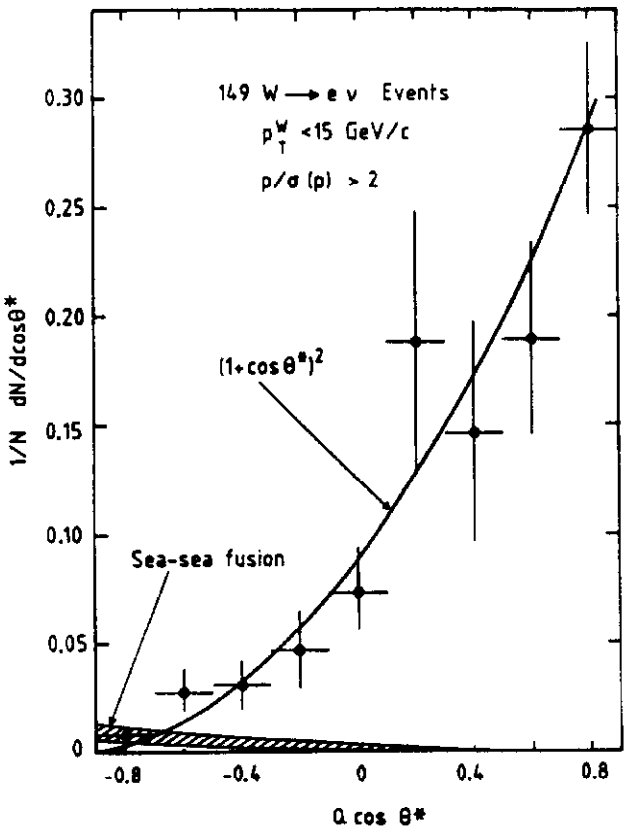

Figure 44: UA1 electron decay angular distribution of W-bosons. The shaded band shows the expected contribution from annihilation processes involving wrong polarity sea quarks only.

both the u and the d quarks contribute which have different vector and axial vector coupling constants. An uncertainty in the predicted asymmetry arises here because of the uncertainty in the relative contribution of the valence u and d quarks. Moreover, higher order QCD and QED corrections and background contributions all tend to dilute the asymmetry signal. The CDF collaboration has recently measured the electron decay angular distribution of Z^0-bosons and found the forward-backward charge asymmetry to be $A_{FB} = (5.3 \pm 5.9 \pm 0.4)\%$ [66]. This translates into a value for $\sin^2\vartheta_w$ of $\sin^2\vartheta_w = 0.228 \pm 0.016 \pm 0.002$. It should be noted that this determination of $\sin^2\vartheta_w$ is independent of the IVB masses.

7.5 IVB Transverse Momentum Distribution

Higher order QCD contributions lead to non-zero transverse momenta of the IVB's and the associated emission of gluons. Experimentally only the transverse momentum of the Z^0-boson, $\vec{p}_t^{\,Z}$, can be measured directly from the transverse momenta of the two final state leptons, whereas for an accurate measurement of $\vec{p}_t^{\,W}$ the transverse momentum of the recoil hadrons needs to be determined. The best precision on the p_t^Z measurement is obtained using the electron decay channel of the Z^0-boson. The accuracy reached by UA2 on the p_t^Z measurement is about ± 2 GeV/c, which is dominated by the uncertainty on the electron energy measurement. Figure 45 shows the UA2 p_t^Z measurement [67]. The average p_t^Z value of the distribution is

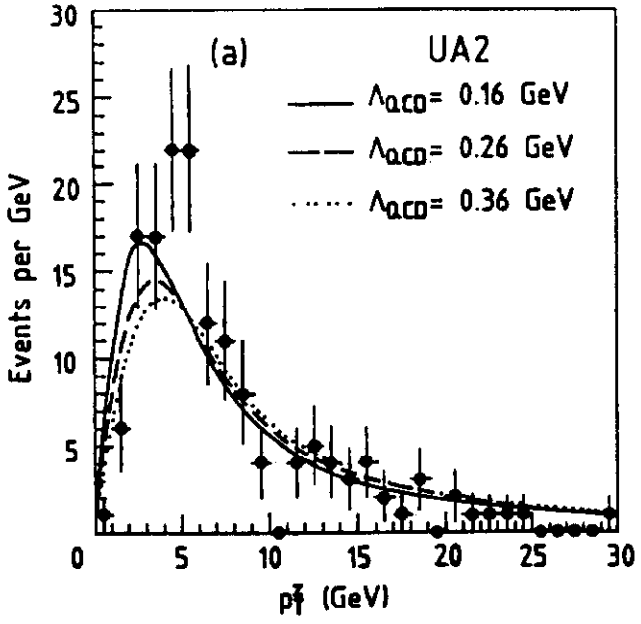

Figure 45: Spectrum of the transverse momentum of the Z^0-boson as measured by UA2, compared with the QCD predictions for three different values of Λ_{QCD}.

found to be $\langle p_t^Z \rangle = 7.0 \pm 0.4 \pm 0.1$ GeV/c. The theoretical predictions for different values of Λ_{QCD}, calculated using soft gluon resummation techniques [61], are superimposed on the data. The variation in the parameter Λ_{QCD} reflects the theoretical uncertainties in the p_t^Z calculation and does not constitute a measurement of Λ_{QCD}.

An accurate determination of the W transverse momentum is much more complex because the measurement of $\vec{p}_t^{\,\nu}$ is inferred from the measurement of the transverse momentum of the recoil hadrons:

$$\vec{p}_t^{\,\ell} + \vec{p}_t^{\,\nu} + \vec{p}_t^{\,rec} \approx \vec{0}$$
$$\vec{p}_t^{\,\ell} + \vec{p}_t^{\,\nu} = \vec{p}_t^{\,W} = -\vec{p}_t^{\,rec}$$

The determination of the transverse momentum of the W-boson thus implies an accurate measurement of the transverse momentum of the recoil jet. Since the p_t^W spectrum peaks at low p_t values, a good understanding of the low energy hadron response of the calorimeter needs to be acquired in order to arrive at an accurate determination of $\vec{p}_t^{\,rec}$. The nature of the $\vec{p}_t^{\,rec}$ measurement requires a careful study of both the detector resolution and the systematic effects.

The energy balance of W-events has a finite resolution due to the finite resolution of the calorimeters. The resolution is studied by looking at the $\not{p}_t$ resolution in two-jet events and minimum bias events, which are expected to be the boundaries for the resolution in W-events. The $\not{p}_t$ resolution is parametrized, as discussed in conjunction with equation 33, as function of the total scalar E_t in the event.

The energy balance in W-events can be systematically offset from zero. Three sources can be identified which contribute to this effect: *i*) initial state radiation produced at very small angles which escapes detection, *ii*) the fact that for slow particles, the energy measured in the calorimeter is smaller than their momentum, *iii*) calorimeter non-linearities and read-out thresholds.

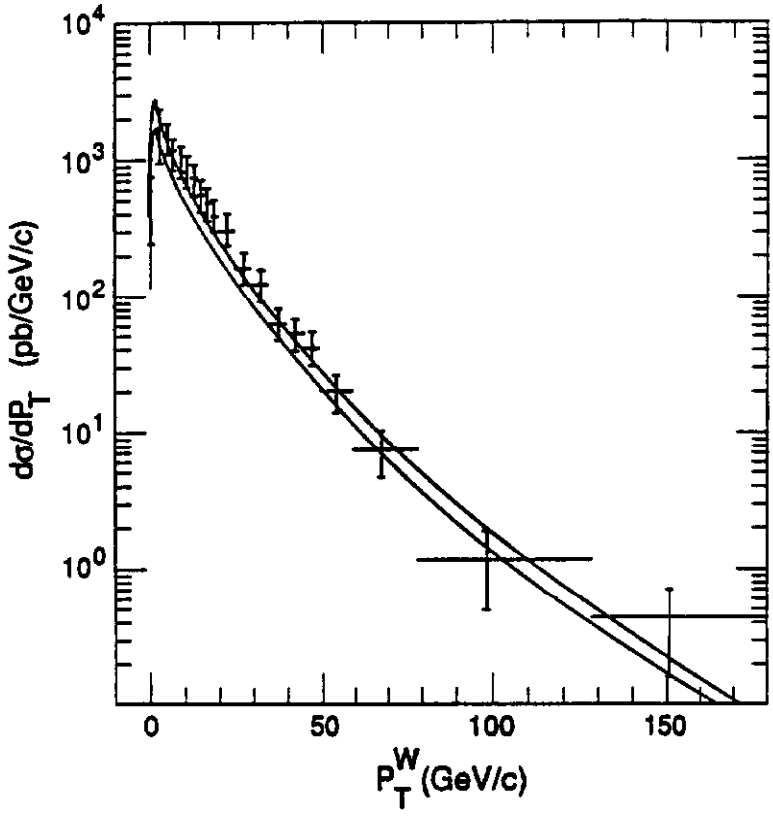

Figure 46: Differential cross section $d\sigma/dp_t^W$ for W-production as measured by CDF. The band indicated by the solid lines is the next to leading order theoretical prediction using $\Lambda_{QCD} = 190\ MeV$.

Because of the similarity of the production mechanism for W- and Z^0-events the best method to obtain a quantitative estimate on $\vec{p}_t^{\,rec}$ is to examine $Z^0 \rightarrow e^+e^-$ events. With the data collected to date, the statistics of Z^0-events prevents an accurate determination of the systematic biases on $\vec{p}_t^{\,rec}$ using this method. Rather, the effects are modelled in a Monte Carlo, cross checked with the Z^0-data, and applied to the model for W-production, taking into account the small differences predicted by theory. The determination of the W transverse momentum is an intricate study requiring a thorough understanding of many aspects of the detector. A much more detailed discussion can be found in the references [67, 68, 69].

Figure 46 shows the differential cross section, $d\sigma/dp_t^W$, as measured by CDF, of their data sample of 2496 $W^{\pm} \rightarrow e^{\pm}\nu$ events based on an integrated luminosity of $4.05 \pm 0.28\ pb^{-1}$ [68]. The band indicated by the solid lines is the next-to-leading order QCD calculation [70] with $\Lambda_{QCD} = 190\ MeV$ using the MRS structure functions. Besides providing a sensitive test of QCD, deviations from the QCD prediction at large p_t could indicate new physics beyond the standard model. The data is in good agreement with the theory and no significant deviation from the standard model prediction is observed. Perhaps the most important reason for an accurate measurement of the W transverse momentum is because it is needed for the determination of the W transverse mass, and thus affects the accuracy of the W-mass measurement.

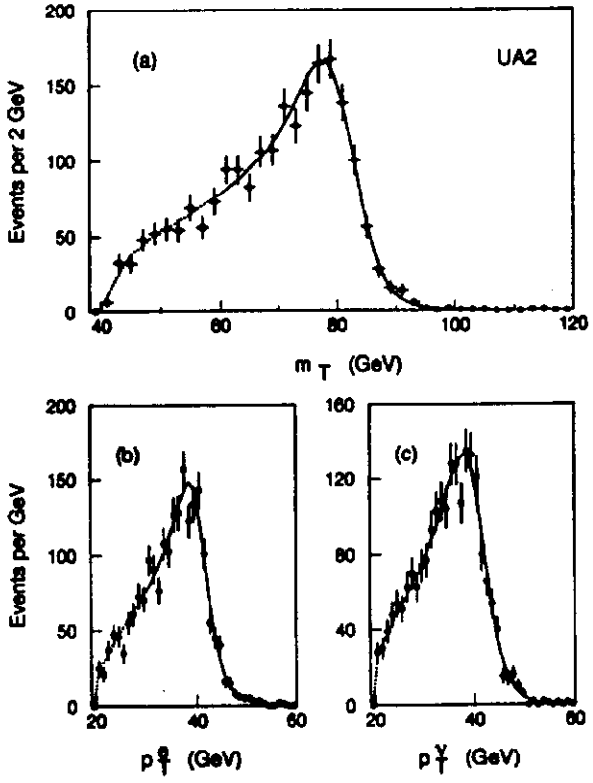

Figure 47: Spectra of (a) the transverse mass, (b) the electron transverse momentum, (c) the neutrino transverse momentum of the UA2 $W^{\pm} \rightarrow e^{\pm}\nu$ data sample. The curves show the results of the fit, with the solid sections indicating the range over which the fit is performed.

7.6 IVB Mass Determination

The Z^0-boson mass can be determined in a straightforward way from the lepton-pair invariant mass distribution. The invariant mass distribution is fitted to a relativistic Breit-Wigner shape, taking into account the detector resolution and the parton luminosity, leaving the Z^0-mass and width as free parameters. The W-boson mass cannot be determined directly from its leptonic decay products because the longitudinal component of the neutrino momentum is unknown. Only the transverse component of the mass, as defined in equation 31, can be measured directly. In order to correctly account for the W longitudinal and transverse motion and the detector characteristics, Monte Carlo simulations are relied on to extract the W-mass. Since the mass of the W-boson and its decay width are correlated, probability density functions are generated in the variables p_t^e, $\not{p}_t$ and m_t using a Monte Carlo simulation for a grid of W-masses and widths. In general a maximum likelihood fit is then performed in these variables to extract the W-mass and width. The most accurate measurement is obtained from the transverse mass distribution since this quantity uses the p_t of both the electron and neutrino and is least sensitive to the W transverse momentum. Figure 47 shows the UA2 transverse mass distribution (a), and the p_t^e (b) and p_t^ν (c) spectra for their $W^{\pm} \rightarrow e^{\pm}\nu$ data sample of 2065 events [71]. The current W- and Z^0-mass measurements are summarized in table 2. The third error quoted in several cases is the error on the absolute energy scale.

Exp.	Channel	M_{IVB} (GeV)
UA1	$Z^0 \to e^+e^-$	$93.1 \pm 1.0 \pm 3.0$
	$Z^0 \to \mu^+\mu^-$	$90.7\ ^{+5.2}_{-4.8} \pm 3.2$
UA2	$Z^0 \to e^+e^-$	$91.74 \pm 0.28 \pm 0.12 \pm 0.92$
CDF	$Z^0 \to e^+e^-$	$91.1 \pm 0.3 \pm 0.4$
	$Z^0 \to \mu^+\mu^-$	$90.7 \pm 0.4 \pm 0.2$
UA1	$W^\pm \to e^\pm\nu$	$82.7 \pm 1.0 \pm 2.7$
	$W^\pm \to \mu^\pm\nu$	$81.8\ ^{+6.0}_{-5.3} \pm 2.6$
	$W^\pm \to \tau^\pm\nu$	$89.0 \pm 3.0 \pm 6.0$
UA2	$W^\pm \to e^\pm\nu$	$80.35 \pm 0.33 \pm 0.17$
CDF	$W^\pm \to e^\pm\nu$	$79.91 \pm 0.35 \pm 0.24 \pm 0.19$
	$W^\pm \to \mu^\pm\nu$	$79.90 \pm 0.53 \pm 0.32 \pm 0.08$

Table 2: Intermediate vector boson masses.

7.7 IVB Masses and Standard Model Parameters

A precision measurement of the mass of the intermediate vector bosons probes the higher order corrections in the standard model. In the standard model the masses of the intermediate vector bosons are given by

$$m_W^2 = m_Z^2 \cos^2\vartheta_w \tag{38}$$

$$m_W^2 = \frac{A^2}{(1-\Delta r)\sin^2\vartheta_w} \tag{39}$$

with $A^2 = \pi\alpha/\sqrt{2}\,G_F$. Here G_F is the Fermi constant and α the electromagnetic coupling constant. Using the Marciano-Sirlin convention for the renormalized parameters [72], the first equation relating the W-mass to the Z^0-mass holds to all orders. The value for Δr is generated by higher order corrections in the standard model, with the dominant contributions coming from vacuum polarization diagrams. In leading-log approximation the contribution of the photon vacuum polarization to Δr is given by

$$\Delta r \approx \frac{\alpha}{3\pi} \sum_{m_f < m_Z} N_c Q_f^2 \ln\frac{m_Z^2}{m_f^2} \tag{40}$$

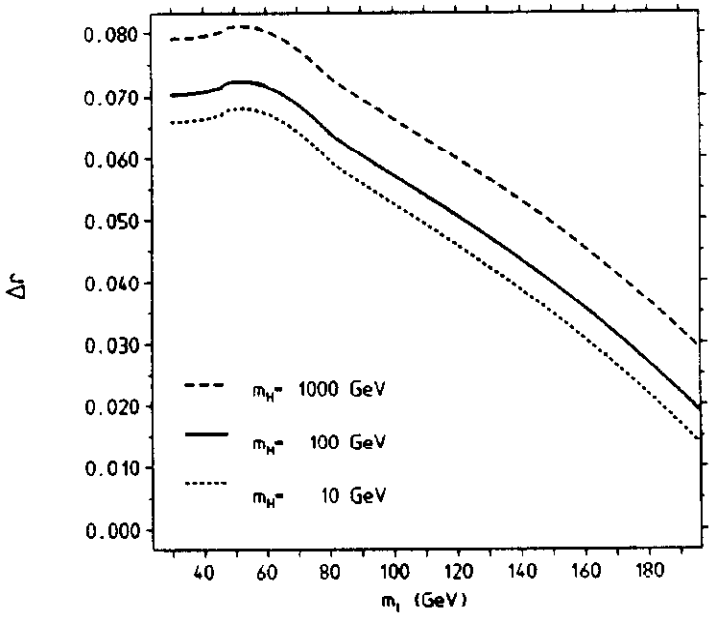

Figure 48: Δr as function of the top quark mass for various Higgs masses.

N_c indicates the number of color degrees of freedom, 3 for quarks and 1 for leptons. Simply inserting the known values for the fermion charges and masses gives that $\Delta r \approx 0.07$. There are, however, additional contributions to Δr that are not small. The main contribution comes from the top quark of which the dominant correction term to Δr is quadratic in the top quark mass and carries a negative sign. Thus, if the top quark is heavy the value for Δr is reduced. For a top quark mass of 250 GeV/c^2, for example, the additional contribution from the top quark is about -0.07, so that Δr is reduced to its tree level value 0. The Higgs boson, new generations and possible extensions of the standard model also contribute but those contributions are generally less than 0.01. The relation between Δr and m_t is given graphically in figure 48 for three different values of the mass of the Higgs boson [73]. The current value for Δr, based on the world average W-boson mass, is $\Delta r = 0.048 \pm 0.025$. It is clear that the current measurements do not yet provide a significant test of the higher order corrections in the standard model.

Since the mass of the W-boson depends on Δr figure 48 can be recast in a dependence of m_W on m_t, shown in figure 49. The horizontal dotted lines indicate the error on the current CDF measurement of m_W; the vertical dotted line is the limit on m_t from a direct top quark search. If the W-boson mass is measured to an accuracy of 100 MeV/c^2, indicated by the dashed lines in the figure, the window on standard model parameters is clearly narrowed down and a relatively stringent bound on the range of the top quark mass can be set. The situation becomes very interesting when the top quark has been discovered because the mass of the Z^0-boson, W-boson and top quark should form a set of self-consistent measurements within the framework of the standard model. With an integrated luminosity of 25 pb^{-1}, which both CDF and DØ expect to collect during the next collider run, the DØ experiment expects to be able to measure the W-mass to a precision of

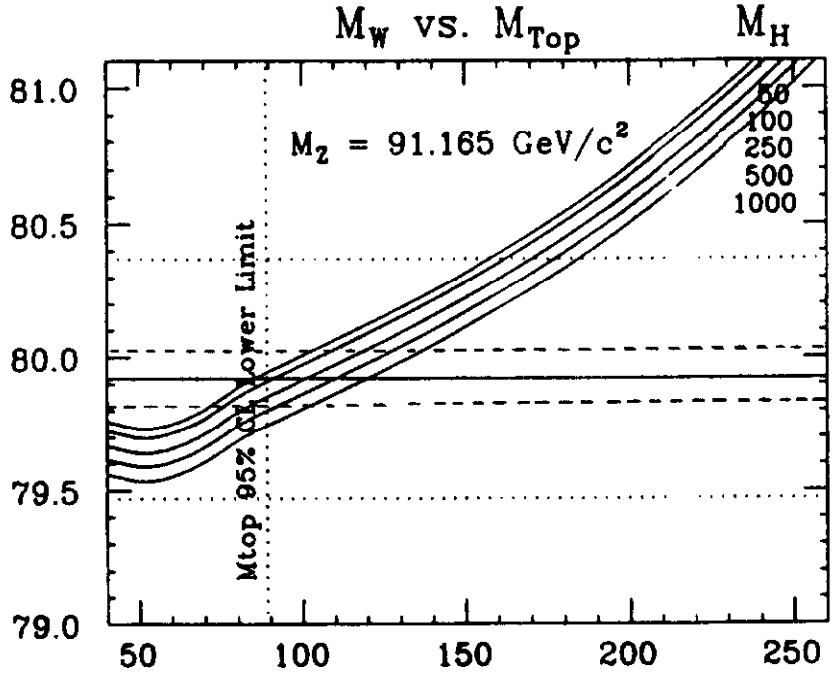

Figure 49: Dependence of m_W on m_t for various masses of the Higgs boson. The dotted lines indicate the precision of the current CDF measurement of the W-boson mass and the limit on the top quark mass. The dashed lines indicate the window on m_t set by a 100 MeV/c^2 accurate measurement of m_W.

about 150 MeV/c^2, resulting in an error on Δr of about 0.008. The error on Δr approximately scales with the error on the W-mass.

One should realize that the study of the W-bosons and W-like objects becomes increasingly difficult with increasing $\sqrt{s}$. Although, for example, the W-production cross section increases by about a factor 3 going from $\sqrt{s} = 0.63\ TeV$ to $\sqrt{s} = 1.8\ TeV$ (see figure 50a) [61], the QCD 2-jet production increases by a factor 10, resulting in a worse signal to background ratio. In addition, the mean p_t increases, which broadens the Jacobian peak of the W-decay and thus affects the precision of the W-mass determination. Moreover, the gain in cross section is partly undone because of a less central production of the W's, illustrated in figure 50b. It is clear that the LHC and SSC are not the right machines to do precision studies in the W, Z sector.

8 Heavy Flavors

8.1 Heavy Flavor Production

One of the high priority searches of the collider experiments is the search for the top quark. In order to have a reliable prediction of the production cross section for top quark production, it is essential to test our understanding of the production rates of known heavy particles such as the bottom quark. The study of the b-system has also many other particularly interesting aspects. Since its production cross section

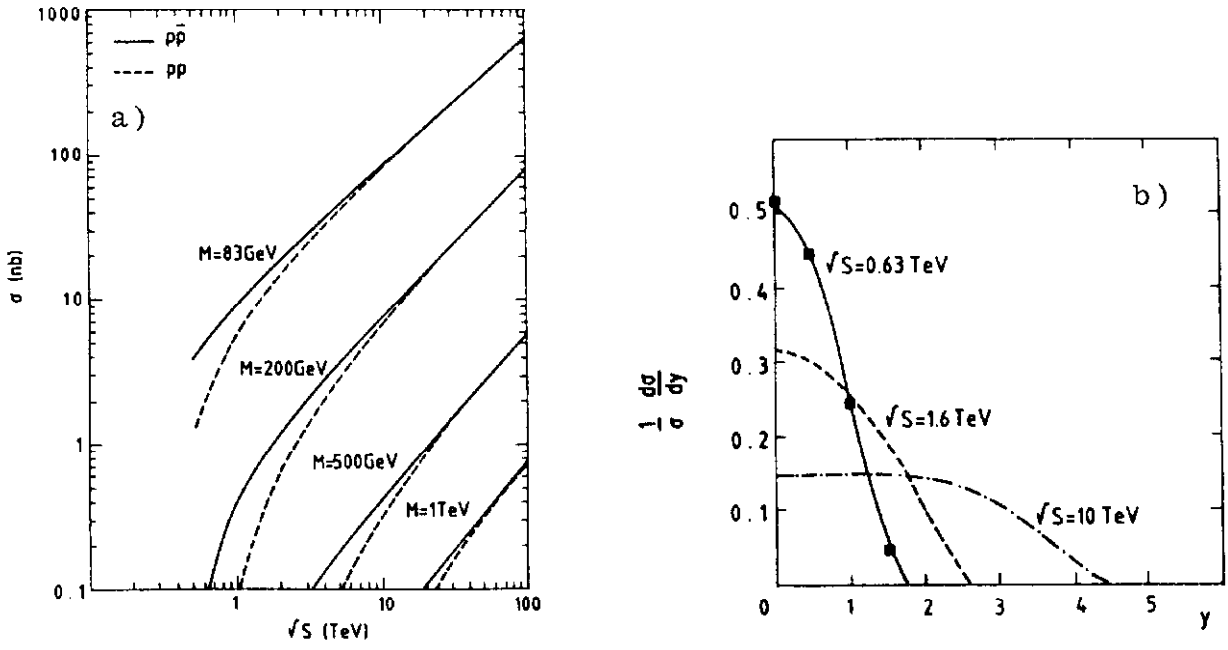

Figure 50: a) Total production cross section as function of $\sqrt{s}$ for W-bosons and for hypothetical W's with higher mass. b) Normalized rapidity distributions for W-boson production at various $\sqrt{s}$.

is very large, it offers the possibility to study specific decay channels of the b-quark in great detail without suffering in rate from a small branching ratio.

The production of heavy flavors proceeds through the three major processes of flavor creation, flavor excitation and gluon splitting. Some representative lowest order Feynman diagrams of the three classes of processes are shown in figure 51. Since the mass of the heavy quark provides a natural limit for the lowest momentum transfer, these processes can be calculated in perturbative QCD, and a full $\mathcal{O}(\alpha_s^3)$ calculation exists [74]. There are, however, rather large uncertainties in the theoretical predictions due to the uncertainties in the choice of parton distribution functions, the choice of the renormalization scale μ and the quark masses, to name a few. The study of the process $\bar{p}p \rightarrow \bar{b}b$ could thus provide stringent tests for the QCD calculations.

The differential cross section $d\sigma/dp_t^2$ for production of a heavy quark with transverse momentum p_t has a $1/m_t^4$ dependence, where the transverse mass of the heavy quark is defined as $m_t = \sqrt{m_q^2 + p_t^2}$. It peaks at transverse momenta of the order of the heavy quark mass m_q. It should be noted that at high transverse momenta the cross section for $\bar{c}c$ and $\bar{b}b$ production are the same, this in contrast to heavy quark production at e^+e^- colliders where the b-quark yield is suppressed by a factor of 4 because of the coupling of the b-quarks to the photon.

The standard techniques for identifying heavy flavors are *i*) tagging on prompt leptons from the b-decay, *ii*) reconstruction of the decay vertex, *iii*) identification of explicit decays, *iv*) broadening of jets. Tagging on prompt leptons, especially muons, has been the most successful technique so far in identifying heavy flavors. Since muons can be identified easily within a jet and only need a relatively

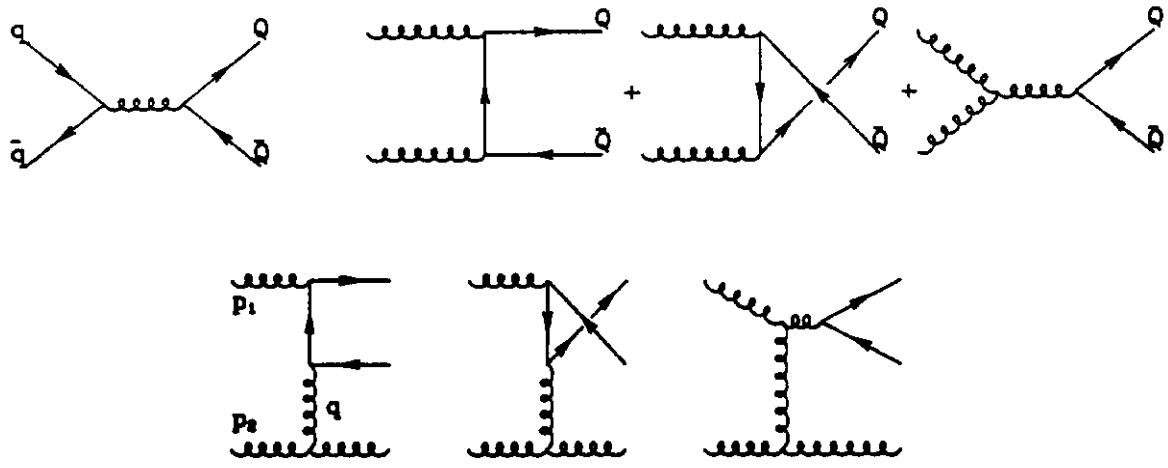

Figure 51: Lowest order Feynman diagrams for heavy quark production.

low p_t trigger threshold, muons are superior to electrons for the study of heavy flavor production. For most experiments b-physics is thus synonymous with muon-physics. It is the challenge for CDF and DØ to enlarge the scope of the b-physics program to include the electron channel.

Since b-quarks are measured through their leptonic decay products, the measurement of the prompt leptons needs to be deconvoluted for the two effects which govern the transition from heavy quark to prompt lepton, *viz.* the effects of heavy quark fragmentation and the decay of the hadron containing the heavy quark. The fragmentation of heavy quarks is described by fragmentation functions which give the probability for a heavy quark to pick up a light quark, forming a meson carrying a fraction z of the original heavy quark energy. The decay of the meson is determined simply by its decay kinematics, the weak coupling constants and the Cabibbo-Kobayashi-Maskawa matrix elements. The effects of the fragmentation and decay are illustrated in figures 52a and 52b for bottom and charm production at 630 GeV, respectively [75]. Although the cross sections for b- and c-quark production are almost equal at large p_t, muons from b-decays are the main source of prompt muons due to the harder b-fragmentation function. At $\sqrt{s} = 1.8\ TeV$ about 70% of muons with a p_t above 3 GeV/c come from b-decay.

8.2 Bottom Quark Production Cross Section

The beauty production cross section can be measured through many different independent decay channels, some of which are

$$
\begin{array}{lllll}
\bar{p}p & \rightarrow & \bar{b}b & \rightarrow & \mu X \\
\bar{p}p & \rightarrow & \bar{b}b & \rightarrow & J/\psi X \quad \rightarrow \quad \mu^+\mu^- X \\
\bar{p}p & \rightarrow & \bar{b}b & \rightarrow & c\mu X \\
 & & & & \quad \hookrightarrow \mu X \\
\bar{p}p & \rightarrow & \bar{b}b & \rightarrow & \mu^- X \\
 & & \hookrightarrow \mu^+ X & &
\end{array}
$$

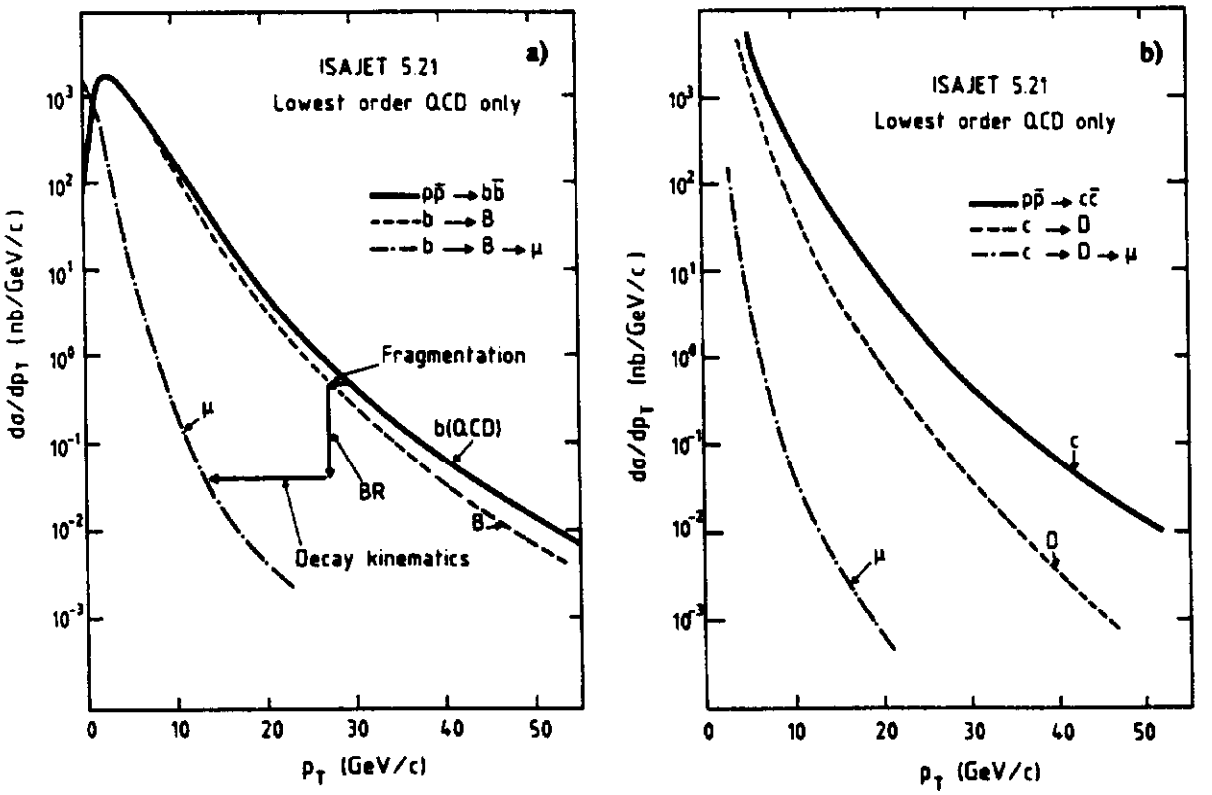

Figure 52: Differential cross sections at the quark, hadron and muon level for a) bottom quark production and b) charm quark production.

Besides these four channels there are of course the reconstructed exclusive b-decays. For the study of the b-production cross section, as carried out by UA1, the inclusive muon data sample was used. This choice was motivated by the thick hadron absorber of the UA1 calorimeter, allowing the detection of muons in and close to hadron jets. The experimental difficulty is the separation of prompt leptons from misidentified hadrons and the determination of the charm contribution. Figure 53 shows the muon p_t spectrum of the UA1 inclusive muon data sample in the pseudorapidity range $|\eta| < 1.5$, based on a total integrated luminosity of 4.7 pb^{-1}. At low p_t^μ the dominant source of background is the decay of pions and kaons in flight. To optimize the signal to background ratio, only muons with $p_t^\mu > 10\ GeV/c$ are selected. In the final data sample the decay of pions and kaons in flight still represents about 38% of the muons [76, 77].

Knowing the luminosity and acceptance for this process, the b-quark production cross section can be determined immediately from the rate of inclusive muon events, if the relative b-quark contribution is known. In order to discriminate between b-quarks and c-quarks, UA1 uses the variable p_t^{rel}, defined as the transverse momentum of the muon with respect to the axis of the jet containing the muon. The harder fragmentation function for b-quarks results in a larger p_t^{rel} for b-quarks than for c-quarks. Figure 54 shows the UA1 p_t^{rel} distribution for the data together with a Monte Carlo fit of the $\bar{b}b$, $\bar{c}c$ and π/K background contribution to the data. By fitting a weighted sum of the predicted p_t^{rel} distributions for the $\bar{b}b$ and $\bar{c}c$ contribution to the data sample, the $\bar{b}b$ fraction has been determined to be $0.33 \pm 0.03 \pm 0.03$

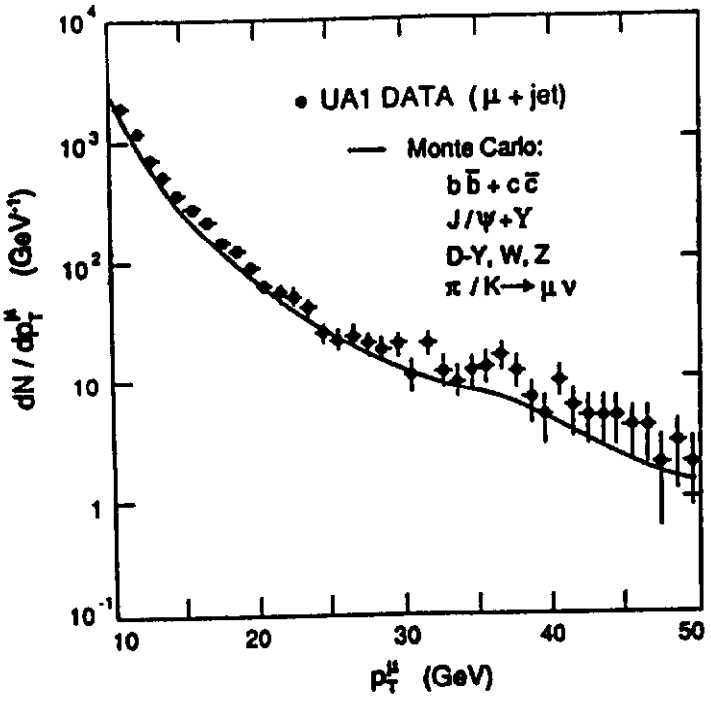

Figure 53: Muon p_t spectrum of the UA1 inclusive muon sample.

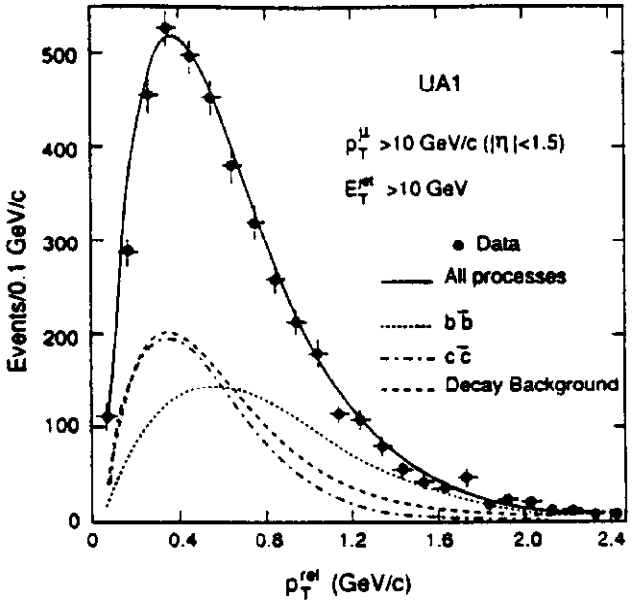

Figure 54: Muon p_t^{rel} distribution for the UA1 inclusive muon data sample. The fitted contributions from the various processes and the sum of all processes are indicated.

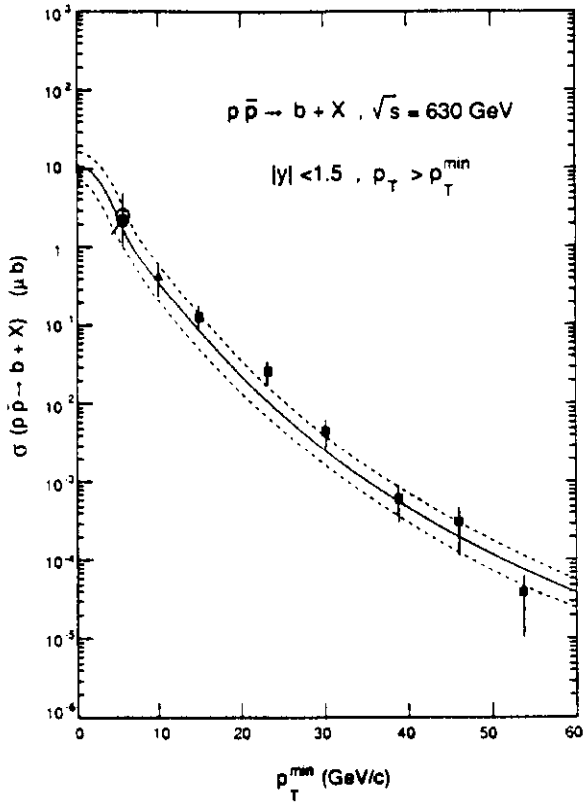

Figure 55: UA1 inclusive b-quark production cross section for $|\eta| < 1.5$ versus the b-quark transverse momentum threshold. The curves indicate the $\mathcal{O}(\alpha_s^3)$ QCD prediction with its uncertainty.

with a ratio of $N(\bar{b}b)/(N(\bar{b}b) + N(\bar{c}c)) = 0.54 \pm 0.10$ [77]. In the determination of this fraction the background contribution, estimated from di-jet events, was fixed.

Since the production cross section for b-quarks is large, the decay of b-quarks into J/ψ-mesons, which subsequently decay into $\mu^+\mu^-$-pairs, can also be used to determine the production cross section even though the combined branching ratio for this channel is rather small: $BR(b \to J/\psi) \cdot BR(J/\psi \to \mu^+\mu^-) = 0.012 \cdot 0.069 = 8.3\,10^{-4}$. One of the advantages of this channel is the very clear di-muon signal from the J/ψ-decay with little background. The only significant background comes from radiative χ_c decays, $\chi_c \to \gamma J/\psi$, where the χ_c is mainly produced through gluon fusion, $gg \to g\chi_c$ [78]. The measurement of the partial inclusive J/ψ production cross section gives the b-quark production cross section if the fraction of J/ψ's from b-decays is known. This fraction is easily determined using the event topology. One should recall that the J/ψ's coming from b-decays are non-isolated, in contrast to those which are directly produced or which come from radiative χ_c decays. Using the charged multiplicity around the J/ψ direction as a discriminant, UA1 has determined the fraction of J/ψ's coming from b-decays to be $0.31 \pm 0.02 \pm 0.12$. At the Tevatron this fraction increases to about 0.64 as indicated by preliminary CDF results.

To convert the measured muon differential cross section, $d\sigma/dp_t^\mu$, to the b-quark production cross section, $d\sigma/dp_t^b$, a Monte Carlo simulation is used which

uses the b-quark fragmentation parameters, decay kinematics and branching ratios as measured in e^+e^- collisions. Figure 55 shows the measured UA1 b-quark production cross section for producing b-quarks with transverse momentum $p_t^b > p_t^{min}$, integrated over a pseudorapidity range $|\eta| < 1.5$. Here, p_t^{min} is defined such that 90% of the muon events have $p_t^b > p_t^{min}$ [77]. The data agrees well with the $\mathcal{O}(\alpha_s^3)$ QCD calculation, indicated by the solid line. The dashed lines give the error on the theoretical prediction. Extrapolating the data to $p_t^{min} = 0$, a total production cross section of $\sigma(\overline{p}p \rightarrow b + X) = 12.8 \pm 4.7 \pm 6\ \mu b$ for $|\eta| < 1.5$ at $\sqrt{s} = 0.63\ TeV$ is obtained, where the first and second error are the experimental and theoretical error, respectively. In the plot are also shown the results obtained by measuring the production cross section using the direct di-muon and the single cascade di-muon decay channel indicated at the beginning of this section. The measurements of all four independent production channels are in very good agreement.

8.3 Flavor Oscillations

Like in the $K^0 - \overline{K}^0$ system, transitions between B^0- and $\overline{B}^0$-mesons are allowed by second order weak interactions (see Fig. 56). In the approximation that the weak interaction conserves CP, the mass eigenstates are given by the CP eigenstates $|B_1^0\rangle = \frac{1}{\sqrt{2}}(|B^0\rangle + |\overline{B}^0\rangle)$ and $|B_2^0\rangle = \frac{1}{\sqrt{2}}(|B^0\rangle - |\overline{B}^0\rangle)$. These states will in general differ in mass and width, giving rise to a time dependent phase difference between the two states. The probability to observe a B^0- or $\overline{B}^0$-meson thus oscillates. To measure the time evolution of these states would require vertex detectors with extremely high resolution, which at the moment are not available in a $\overline{p}p$ environment. Rather, the $\overline{p}p$ collider experiments measure time integrated quantities like the probability that a B^0-meson decays into a "wrong" sign lepton. Denoting the difference in mass and decay width between the two mass eigenstates as $\Delta m = m_1 - m_2$ and $\Delta\Gamma = \Gamma_1 - \Gamma_2$, the parameters x and y are defined as

$$x = \frac{\Delta m}{\Gamma} \qquad y = \frac{\Delta\Gamma}{2\Gamma}$$

where $\Gamma = \frac{1}{2}(\Gamma_1 + \Gamma_2)$. Ignoring CP violation, the time averaged mixing probability is given by [79]

$$\chi = \frac{Prob(B^0 \rightarrow \overline{B}^0)}{Prob(B^0 \rightarrow B^0) + Prob(B^0 \rightarrow \overline{B}^0)} = \frac{x^2 + y^2}{2 + 2x^2} \tag{41}$$

So, if $x \gg 1$, that is, if the decay time is much larger than the oscillation time, χ approaches 0.5, *i.e.* there is a 50% probability to observe a B^0 or $\overline{B}^0$-meson. This is the case when there is full mixing.

The dominant contribution to x, the ratio of the mass difference and the average decay width, comes from the double t-quark exchange diagram and is ap-

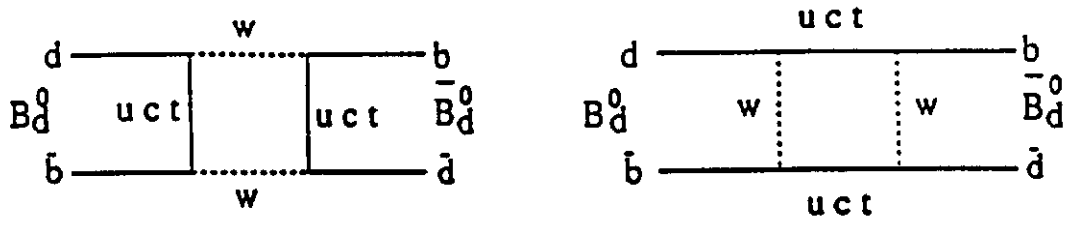

Figure 56: Box diagrams responsible for the transition of a B_d^0 into a $\overline{B}_d^0$ meson.

proximated by [80]

$$x_q \approx \frac{G_F^2}{6\pi^2}\,\tau_{B_q}\,K_{B_q}\,f_{B_q}^2\,m_{B_q}\,m_W^2\,\eta_q^{QCD}\,|V_{tb}^*\,V_{tq}|^2\,\frac{m_t^2}{m_W^2} \qquad q = s, d \qquad (42)$$

Here τ_{B_q} is the decay time of the B_q-meson, f_{B_q} its decay constant and m_{B_q} its mass. K is a model dependent parameter ($0.5 < K < 1.5$) and η_q^{QCD} takes into account QCD corrections. The main difference between the B_d^0 and B_s^0 meson is thus due to the difference in the CKM-matrix elements V_{td} and V_{ts}. A very handy parametrization of the CKM-matrix that can be used to evaluate quantities involving CKM-matrix elements is [81]

$$V = \begin{pmatrix} V_{ud} & V_{us} & V_{ub} \\ V_{cd} & V_{cs} & V_{cb} \\ V_{td} & V_{ts} & V_{tb} \end{pmatrix} = \begin{pmatrix} 1-\frac{\lambda^2}{2} & \lambda & \lambda^3 \\ -\lambda & 1-\frac{\lambda^2}{2} & \lambda^2 \\ \lambda^3 & -\lambda^2 & 1 \end{pmatrix}$$

with $\lambda \approx 0.22$. Under the assumption that, except for the relevant CKM-matrix elements, all parameters in equation 42 are the same for B_d and B_s mesons, the ratio of mixing in the B_s and B_d system is given by

$$\frac{x_s}{x_d} = \frac{|V_{tb}^*\,V_{ts}|^2}{|V_{tb}^*\,V_{td}|^2} \approx \frac{\lambda^4}{\lambda^6} = \lambda^{-2}$$

Since V_{td} is much smaller than V_{ts}, mixing in the B_s^0 system is expected to be about 20 times larger than for B_d^0.

Since in high energy $\bar{p}p$ collisions both B_d and B_s mesons are produced, the mixing probability measured is the sum of the mixing probabilities weighted by the relative production factors f_d and f_s for B_d and B_s mesons, respectively

$$\chi = f_d\,\chi_d + f_s\,\chi_s \qquad (43)$$

Using the current limits on the CKM matrix elements

$$0.029 < |V_{ts}| < 0.058 \qquad 0.003 < |V_{td}| < 0.019$$

based on three generation unitarity of the matrix, an upper limit on χ_d as function of χ_s can be given. Assuming again that all parameters in equation 42 are the same for B_d and B_s mesons it follows that

$$\frac{x_d}{x_s} = \frac{|V_{td}|^2}{|V_{ts}|^2} < 0.43$$

Using equation 41 and taking y to be negligibly small, it is straightforward to write this as

$$\chi_d < \frac{0.43^2\,\chi_s}{1-2\chi_s(1-0.43^2)} \tag{44}$$

that is, an upper limit on χ_d as function of χ_s can be placed based on the known limits on the CKM-matrix elements.

Since the sign of the decay lepton identifies the parent meson, the experimental signature for $B^0-\overline{B}^0$ mixing is the observation of an excess of like sign di-leptons. The quantity directly measured is

$$R = \frac{N(\ell^+\ell^+) + N(\ell^-\ell^-)}{N(\ell\ell)}$$

The relation between R and χ can be written down by recalling that χ denotes the probability for a B-meson to oscillate. The probability for a $B^0-\overline{B}^0$ system, with both b-quarks decaying directly into leptons, to contribute to the like sign di-lepton sample is simply given by $2\chi(1-\chi)$, *i.e.* one b-quark oscillates and the other one does not. The expression for R can thus be written as

$$\begin{aligned} R \;&= (f_{bb} + f_{(bc)(bc)} + f_{b(b\bar{c})})\,2\chi(1-\chi) + \\ &\quad f_{b(bc)}\,[1-2\chi(1-\chi)] + f_{back}P_{\pm\pm} \end{aligned}$$

Here f_{bb}, $f_{b(bc)}$, $f_{(bc)(bc)}$ and $f_{b(b\bar{c})}$ denote the relative contribution to the data sample from the direct b-decay, the single and double cascade decay and the $b\to\bar{c}\to\ell$ decay, respectively. The probability of the background fraction, f_{back}, to contribute to the like sign di-lepton sample is denoted by $P_{\pm\pm}$. For π/K decays in flight this is generally taken to be 50%. Note that $\bar{c}c$, Drell-Yan and Υ-production does not constitute a background for the like sign di-lepton sample. Also note that $D^0\overline{D}^0$ mixing has been neglected. This can be justified by drawing the box diagrams for $D^0-\overline{D}^0$ oscillation and by writing down the corresponding contributions to x following equation 42. It can then be seen that the dominant contribution comes from the s-quark exchange diagram which is suppressed by a factor $m_s^2/(\lambda^2 m_t^2)$ compared to the corresponding contribution for B_s-mesons.

The relative contributions of the different decay chains, $f_{(\alpha)(\beta)}$, are determined by Monte Carlo simulations for the kinematic cuts used in the analysis. The uncertainty in these fractions constitutes the dominant error on the mixing measurement. The measured UA1 value of the mixing parameter is $\chi = 0.148\pm0.029\pm0.017$ and is shown in figure 57a in the χ_d versus χ_s plane [82]. Assuming that the inclusive muonic branching ratio is equal for all b-mesons and b-baryons, equation 43 holds and a value for χ_s can be extracted. The relative production fractions f_d and f_s have been estimated using ISR, UA2 and UA5 data to be 0.36 and 0.18, respectively [83]. Mixing in the B_d system has been measured by the CLEO and ARGUS collaboration at e^+e^- colliders from data taken at the $\Upsilon(4S)$ resonance

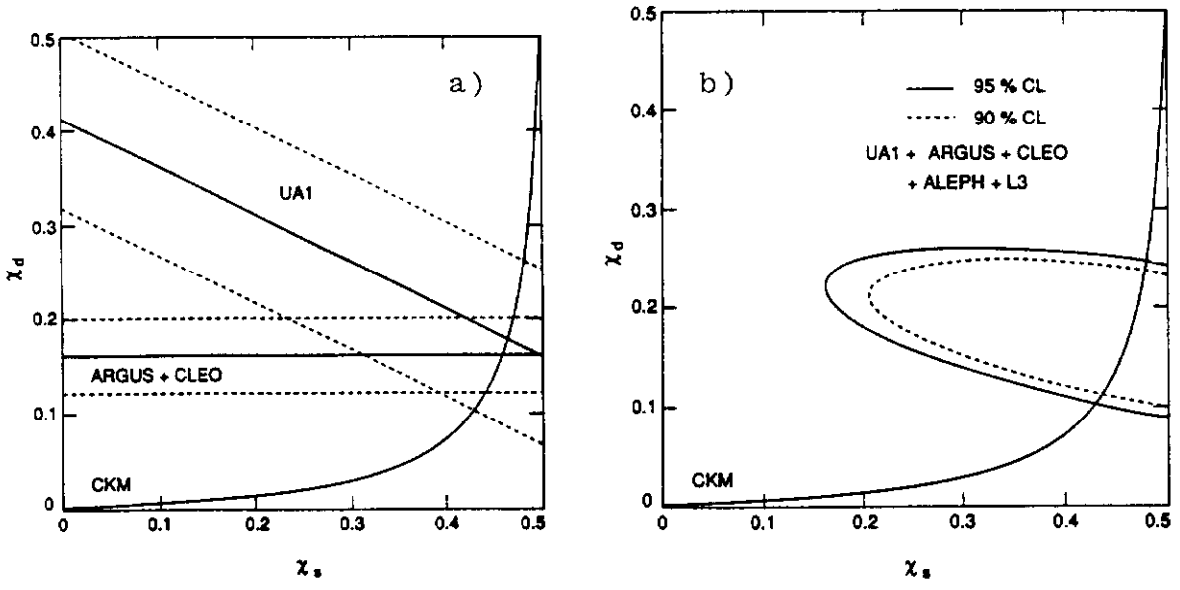

Figure 57: a) B^0-mixing result from UA1 and the weighted average of the ARGUS and CLEO measurement of χ_d. The dotted lines indicate the 1σ bands on the measurements. b) Allowed region in the (χ_d, χ_s)-plane for the combined UA1, ARGUS, CLEO, Aleph and L3 results.

where only production of the B_d is kinematically allowed [84]. The weighted average of these two measurements, $\chi_d = 0.162 \pm 0.039$, is indicated by the horizontal line in figure 57a. Combining both measurements yields $\chi_s = 0.50 \pm 0.20$, indicating full mixing for $B_s^0 - \overline{B}_s^0$. This result again points in the direction of a heavy top quark (cf. eq. 42). The line labeled "CKM" in the figure is the upper limit on χ_d as function of χ_s as given by equation 44. Figure 57b shows the 90% and 95% confidence level contours in the (χ_s, χ_d)-plane when the published LEP results are included [85]. The region allowed by the standard model will be narrowed down considerably by the LEP experiments with the event samples they expect to collect in the near future.

8.4 Top Quark

The search for the "ever elusive" sixth quark, the top quark, has been and still is one of the high priority searches for the $\bar{p}p$ collider experiments. In $\bar{p}p$ collisions there are two major top quark production mechanisms: single t-quark production through W-decay and pair production through gluon fusion. For low top quark masses the dominant production mode is through W-decays. When the mass of the top quark is greater than the W-mass, only the pair production channel contributes. Figure 58 shows the production cross section for single t-quark production through W-decay and for t-quark pair production separately. The cross sections are evaluated for a center of mass energy of 0.63 TeV, the CERN S$\bar{p}p$S operating center of mass energy, and for 1.8 TeV, the Fermilab Tevatron $\sqrt{s}$. Because of the higher center of mass energy, the Fermilab collider experiments have a clear advantage over the CERN

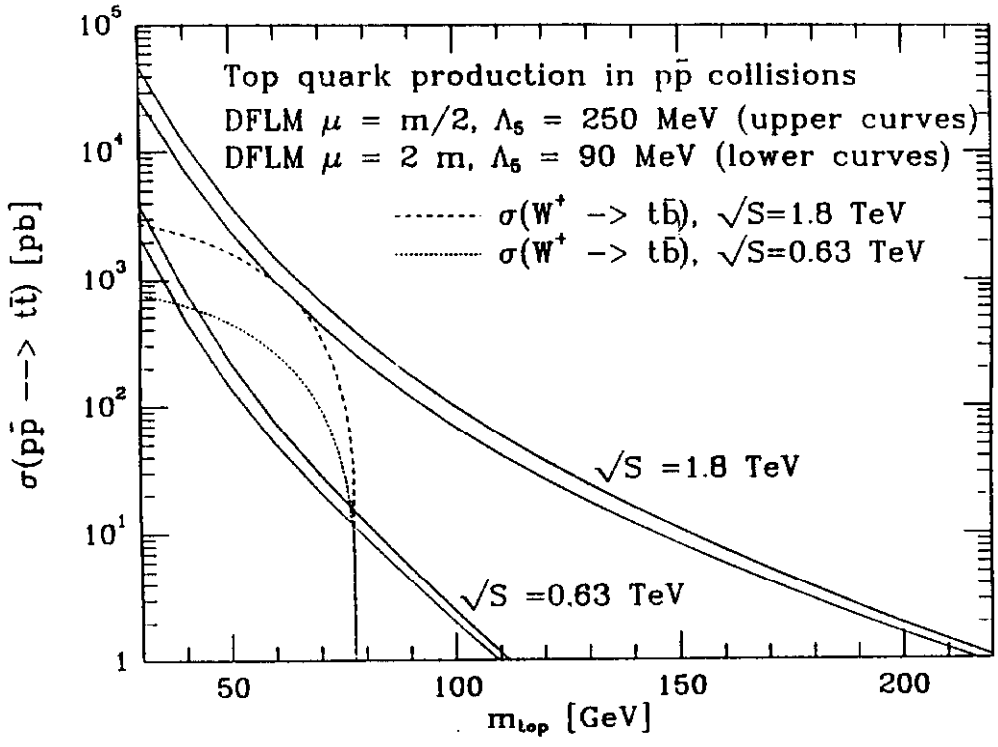

Figure 58: Cross section for top quark production as function of the top quark mass for $\sqrt{s} = 0.63\ TeV$ and $\sqrt{s} = 1.8\ TeV$. The solid lines are for $t\bar{t}$ production and the dashed lines for $W \rightarrow t\bar{b}$.

experiments. Figure 59 shows the total production cross section, *i.e.* the sum of single top production through W-decay and pair production, for $\sqrt{s} = 0.63\ TeV$ and $\sqrt{s} = 1.8\ TeV$. In the lower half of the figure the ratio of the two cross sections is plotted. One can see that for high top quark masses the cross section is about two orders of magnitude larger at $\sqrt{s} = 1.8\ TeV$ than at $\sqrt{s} = 0.63\ TeV$.

In the framework of the standard model, t-quarks decay almost exclusively into a W-boson and a b-quark, $t \rightarrow Wb$, where, depending on the t-quark mass, the W is either virtual or real. As seen in section 7.1, W-bosons have a branching ratio of approximately $\frac{1}{9}$ for decay into each of the three generations of leptons, and a branching ratio of $\frac{3}{9}$ each for decay into $u\bar{d}$ or $c\bar{s}$. Although the all hadronic decay has the largest branching ratio, the top quark signal of this decay channel would be buried in the QCD background. To get a good signal to background ratio, it is required that at least one W decays into leptons.

The UA1 and UA2 experiments have concentrated their search on single t-quark production through W-decay, with the t-quark decaying semi-leptonically. Because of the large mass of the top quark, the lepton from the t-quark decay is expected to be isolated and to carry a lower transverse momentum than leptons from direct W-decays. Moreover, the presence of the b-quark will reduce the total $\not{p}_t$ in top quark events compared to W-events. To discriminate top quark events from the QCD and W background, the UA1 experiment, concentrating on the decay of top quarks into muons, employed a likelihood function. They first constructed the

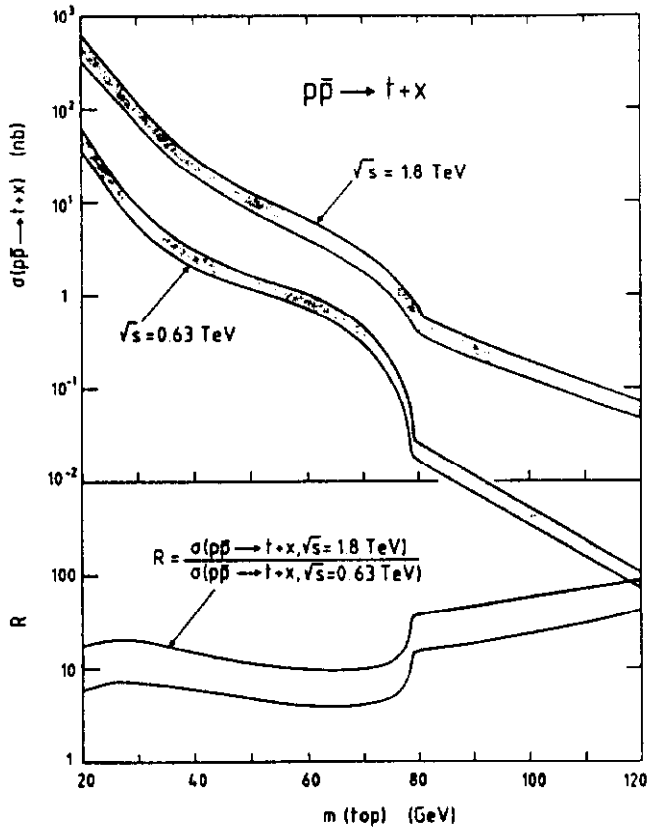

Figure 59: Total top quark production cross section in $\bar{p}p$ collisions as function of m_t for $\sqrt{s} = 0.63\ TeV$ and $\sqrt{s} = 1.8\ TeV$. The lower half shows the ratio of the production cross section at the two center of mass energies.

ratio of the probability density function of a variable x_i for top quark events and the corresponding distribution for the standard processes: $R_i(x_i) = P_{t;i}(x_i)/P_{b;i}(x_i)$. The product of the functions $R_i(x_i)$ for different variables x_i then defines the likelihood function, $\mathcal{L} = \prod_i R_i(x_i)$ [86]. The variables x_i used in their search in the data sample consisting of events with a single muon plus jets were the isolation of the muon, the muon transverse momentum, the missing transverse energy and the difference in azimuthal angle between the muon and the highest p_t jet. A limit on the top quark mass of 52 GeV/c^2 at 95% confidence level has been set using this sample of signal events. Combining all data samples, UA1 arrives at a lower limit of $m_t > 60\ GeV/c^2$ [86]. The UA2 experiment, looking at an excess of events at low transverse mass in the m_t distribution for W-events has set a lower limit of $m_t > 69\ GeV/c^2$ at 95% confidence level [87].

The most stringent limit on the top quark mass comes from CDF [88]. Since the dominant production channel at $\sqrt{s} = 1.8\ TeV$ is the t-quark pair production, the most unambiguous channel to look for the top quark is the electron-muon decay channel

$$t\bar{t} \rightarrow W^+ b\, W^- \bar{b} \rightarrow e\nu\mu\bar{\nu}b\bar{b} \tag{45}$$

The only significant background comes from $\bar{b}b$ production, with both b-quarks decaying semileptonically, and from Z^0-production with the subsequent decay of the Z^0 into a pair of τ-leptons. The soft p_t spectrum of the b-decay leptons and the low

mass of the τ-lepton still allow a clear separation between the signal and background events. The $e\mu$ di-lepton final state can be extended by including the e^+e^-- and $\mu^+\mu^-$-channels, while paying the price of a potential higher background contribution from Drell-Yan and Z^0 production. The CDF limit on the top quark mass from the combined di-lepton and single lepton searches, assuming the standard model decay modes and branching ratios, is $m_t > 91\ GeV/c^2$ [88].

A very challenging decay channel is the decay of the t-pair into a single lepton and jets, $t\bar{t} \rightarrow W^+ b\, W^- \bar{b} \rightarrow \ell\nu q\bar{q}b\bar{b}$ which has a branching ratio 12 times higher than the $e\mu$-final state. Although the experimental difficulties are not to be underestimated, both the CDF and DØ collaboration have developed sophisticated algorithms to search for the top quark in this channel. Since the search for the top quark is not a closed chapter, I would like to refrain from discussing this topic here in detail, but encourage the reader to be on the lookout for future papers on the top quark (search), which will certainly be many and intriguing!

8.5 Outlook

Since the shut down of the CERN S$\bar{p}p$S collider, there are only two $\bar{p}p$ collider experiments operational, CDF and DØ. In view of the total integrated luminosity that will be collected by these two experiments, their physics program looks very bright and challenging. With an integrated luminosity of over 100 pb^{-1}, which should be collected by each experiment by the end of 1993, both the standard model for electroweak interactions and QCD can be subjected to precision tests. This will be possible in part because each experiment will have large enough data samples of different physics channels so that internally consistent measurements and cross calibrations can be made using different event samples. For example, with large enough event samples a measurement of α_s can be obtained using the $W + 1$-jet over $W + 0$-jets ratio, the $W + 2$-jets over $W + 1$-jet ratio, the 3-jet over 2-jet ratio and perhaps even the $Z^0 + 1$-jet over $Z^0 + 0$-jets ratio. The large integrated luminosities will furthermore enable the experiments to set stringent limits on supersymmetric particles, to look for quark substructures and possible extensions of the standard model and to start really exploring the b-quark sector.

To illustrate the possibly exciting times ahead of us at the Tevatron collider, let me conclude these notes with a short discussion of the prospects for top quark discovery and its potential implications. Based on the current Fermilab operating schedule each experiment will have collected a total integrated luminosity of 100 pb^{-1} by the end of 1993, with an additional 100 pb^{-1} collected during the 1995 run. Assuming that the Main Injector becomes operational in 1997, beam-beam collisions will deliver an additional luminosity of 600 pb^{-1} to each experiment of which DØ expects to collect about 400 pb^{-1}. Defining the discovery of the top quark as the observation of 10 events in the $e\mu$-channel, it is clear that the discovery range at the Tevatron spans the full allowed standard model region, which implies that at

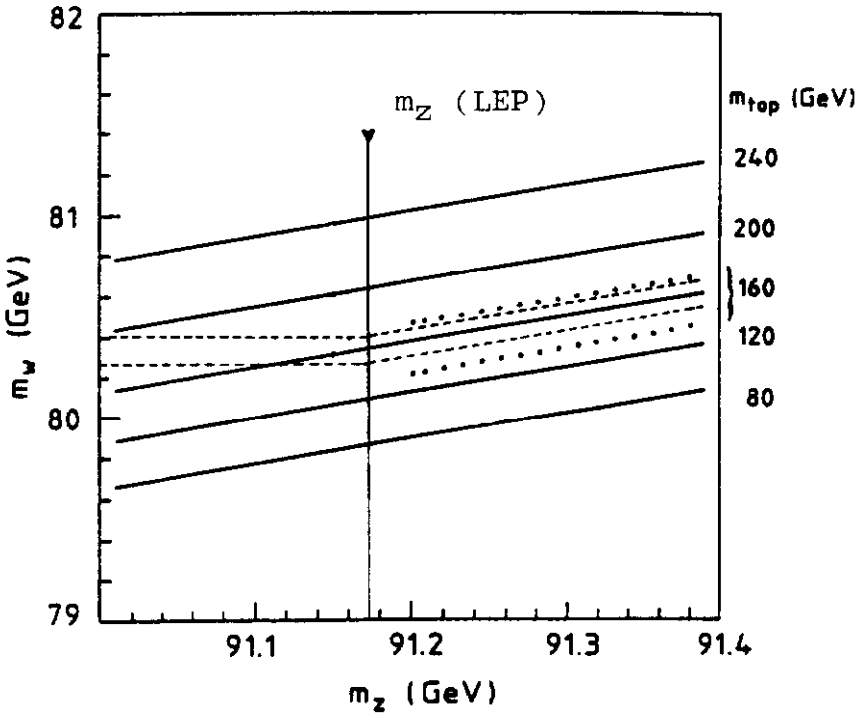

Figure 60: Measurement of the mass of the top quark of $m_t = 160 \pm 10\ GeV/c^2$ within the framework of the standard model.

the end of the decade either the top quark has been discovered or that the standard model is flawed.

Now suppose that three years from now, in the year 1995, the top quark has been discovered and its mass has been measured to be $m_t = 160 \pm 10\ GeV/c^2$. Figure 60 shows the relation between the W- and Z-mass for different values of the top quark mass. The dashed lines indicate the error on the measurement of the top quark mass of $160 \pm 10\ GeV/c^2$. In the year 1995 the measurement of the mass of the Z^0-boson will not have improved much from the current measurement and is known to be $m_Z = 91.175 \pm 0.020\ GeV/c^2$. Intersecting the lines corresponding to the top quark mass measurement with the measurement of the Z^0-boson mass shows that measuring the top quark mass to an accuracy of $\pm 10\ GeV/c^2$ is equivalent in precision to a measurement of the W-boson mass to an accuracy of about $\pm 100\ MeV/c^2$, that is, a measurement with a two orders of magnitude higher accuracy. By 1995 the W-boson mass will indeed be determined to an accuracy of 100 MeV/c^2 and one might hope for inconsistencies between the mass measurements of these three fundamental particles. Moreover, one should note that a precision measurement of the top quark mass gives insight in the Higgs sector well before the turn on of the SSC and LHC. The dotted lines in the figure indicate the prediction for a top quark of mass $m_t = 160\ GeV/c^2$ when varying the Higgs boson mass from 10 GeV/c^2 to 1 TeV/c^2. An accurate measurement of the mass of the top quark can clearly constrain the mass of the Higgs boson.

Acknowledgments

It is a pleasure to thank the organizers of the school for giving me the opportunity to lecture on this subject at such an interesting summer school. Many thanks are due to Paul Grannis for his continuous support and encouragement. I would also like to thank Shekhar Shukla and all my DØ colleagues for useful discussions.

References

1. UA4 Collaboration, D. Bernard *et al.*, Phys. Lett. **B198** (1987) 583.

2. E710 Collaboration, N. Amos *et al.*, Fermilab-Pub-91/267 E710, submitted to Phys. Rev. Lett;
   S. Shukla, Fermilab-Conf-91/216, to be published in "Proceedings of the fourth International Conference on elastic and diffractive scattering", La Biodola, Elba, Italy, May 22-25 (1991).

3. UA4 Collaboration, M. Bozzo *et al.*, Phys. Lett. **B147** (1984) 385.

4. UA5 Collaboration, G.J. Alner *et al.*, Z. Phys. **C32** (1986) 153.

5. E710 Collaboration, N. Amos *et al.*, Phys. Lett. **B243** (1990) 158.

6. CDF Collaboration, S. White, Fermilab-Conf-91/268-E, to be published in "Proceedings of the fourth International Conference on elastic and diffractive scattering", La Biodola, Elba, Italy, May 22-25 (1991).

7. UA5 Collaboration, G.J. Alner *et al.*, Z. Phys. **C33** (1986) 1.

8. CDF Collaboration, F. Abe *et al.*, Phys. Rev. **D41** (1990) 2330

9. UA5 Collaboration, G.J. Alner *et al.*, Phys. Rep. **154** (1987) 247.

10. CDF Collaboration, F. Abe *et al.*, Phys. Rev. Lett. **61** (1988) 1819.

11. UA1 Collaboration, G. Arnison *et al.*, Phys. Lett. **B118** (1982) 167.

12. B. Alper *et al.*, Nucl. Phys. **B87** (1975) 19.

13. D. Antreasyan *et al.*, Phys. Rev. **D19** (1979) 764.

14. UA1 Collaboration, C. Albajar *et al.*, Nucl. Phys. **B335** (1990) 261.

15. A. Breakstone *et al.*, Phys. Lett. **B132** (1983) 463; Phys. Lett. **B183** (1987) 227.

16. L. van Hove, Phys. Lett. **B118** (1982) 138.

17. G. Baym *et al.*, Nucl. Phys. **A407** (1983) 541;
    M. Kataja *et al.*, Phys. Rev. **D34** (1986) 2755;
    G. Bertsch *et al.*, Phys. Rev. **D37** (1988) 1202.

18. A. Astbury *et al.*, UA1 Proposal, CERN/SPSC **78/06** (1978);
M. Calvetti *et al.*, IEEE Trans. Nucl. Sci. **NS-30** (1983) 71;
C. Cochet *et al.*, Nucl. Instr. & Meth. in Phys. Res. **A243** (1986) 45;
M.J. Corden *et al.*, Nucl. Instr. & Meth. in Phys. Res. **A238** (1985) 273;
K. Eggert *et al.*, Nucl. Instr. & Meth. in Phys. Res. **176** (1980) 217 and 223;
G. Bauer *et al.*, Nucl. Instr. & Meth. in Phys. Res. **A253** (1987) 179 and 189;
M. Albrow *et al.*, Nucl. Instr. & Meth. in Phys. Res. **A265** (1988) 303;
UA1 Collaboration, C. Albajar *et al.*, CERN/SPSC **89/23** (1989).

19. B. Mansoulié, Proceedings 3rd Moriond Workshop on $\overline{p}p$ Physics (1983), 609;
A. Beer *et al.*, Nucl. Instr. & Meth. in Phys. Res. **A224** (1984) 360;
M. Dialinas *et al.*, LAL-RT/83-14 (Orsay, 1983);
C. Conta *et al.*, Nucl. Instr. & Meth. in Phys. Res. **224** (1984) 65;
K. Borer *et al.*, Nucl. Instr. & Meth. in Phys. Res. **227** (1984) 29;
R. Ansari *et al.*, Nucl. Instr. & Meth. in Phys. Res. **A263** (1988) 51;
R. Ansari *et al.*, Nucl. Instr. & Meth. in Phys. Res. **A279** (1989) 388;
F. Bosi *et al.*, Nucl. Instr. & Meth. in Phys. Res. **A283** (1989) 532;
R. Ansorge *et al.*, Nucl. Instr. & Meth. in Phys. Res. **A265** (1988) 33;
J. Alitti *et al.*, Nucl. Instr. & Meth. in Phys. Res. **A279** (1989) 364;
K. Borer *et al.*, Nucl. Instr. & Meth. in Phys. Res. **286** (1990) 128.

20. CDF Collaboration, F. Abe *et al.*, Nucl. Instr. & Meth. in Phys. Res. **A271** (1988) 387 and references therein.

21. D. Buchholz *et al.*, Nucl. Instr. & Meth. in Phys. Res. **A257** (1987) 556;
A. Clark *et al.*, Nucl. Instr. & Meth. in Phys. Res. **A261** (1987) 420;
J. Detoeuf *et al.*, Nucl. Instr. & Meth. in Phys. Res. **A265** (1988) 157;
A. Clark *et al.*, Nucl. Instr. & Meth. in Phys. Res. **A279** (1989) 243;
S. H. Aronson *et al.*, Nucl. Instr. & Meth. in Phys. Res. **A269** (1988) 492;
M. Abolins *et al.*, Nucl. Instr. & Meth. in Phys. Res. **A280** (1989) 36;
P. Franzini, Nucl. Instr. & Meth. in Phys. Res. **A289** (1990) 438;
R.D. Schamberger, "DØ Calorimeter Electronics", Proceedings of the Second International Conference on Advanced Technology and Particle Physics, Como, Italy, 11-15 June, 1990;
A. Spadafora, Proceedings of the First International Conference on Calorimetry in High Energy Physics, Batavia, IL, Oct 29 - Nov 1 (1990) 77 (eds. D. Anderson, M. Derrick, H.E. Fisk, A. Para, C. Sazama);
N. Amos *ibid.* p. 84; M. Demarteau *ibid.* p. 91; G. Blazey *ibid.* p. 101;
P. Franzini, *ibid.* p. 359;
H. Aihara, Proceedings of the 1990 IEEE Nuclear Science Symposium, Arlington, VA, Oct 23-26 (1990);
A. Spadafora, Proceedings of the 5th Pisa Meeting on Advanced Detectors, Elba, May 26-31 (1991);

S. Feher, to be published in "Proceedings of the Second International Conference on Calorimetry in High Energy Physics", Capri, Italy, Oct 14-18 (1991);
W. Guryn *ibid.* ; N. Roe *ibid.* ;
C. Brown, *et al.*, Nucl. Instr. & Methods in Phys. Res. **A279** (1989) 331.

22. ZEUS Calorimeter Group, A. Andresen *et al.*, Nucl. Instr. & Meth. in Phys. Res. **A290** (1990) 95.

23. G. Altarelli, Phys. Rep. **81** (1982) 1.

24. R.K. Ellis, N.J. Stirling, "QCD and Collider Physics", Proceedings of the 1988 CERN School of Physics, CERN Yellow Report, **CERN 91-01** (1991) 135.

25. G. Altarelli, G. Parisi, Nucl. Phys. **B126** (1977) 298.

26. E. Eichten, Proceedings of the Yale Theoretical Advanced Study Institute, High Energy Physics (1985) 709 (eds. M. Bowick, F. Gürsey)

27. E. Eichten, I. Hinchliffe, K. Lane, C. Quigg, Rev. Mod. Phys. **56** (1984) 579.

28. M. Diemoz, F. Ferroni, E. Longo, G. Martinelli, Z. Phys. **C39** (1988) 21.

29. A. Martin, R. Roberts, W. Stirling, Phys. Rev. **D37** (1988) 1161; Phys. Lett. **B206** (1988) 327.

30. J. Morfin, W.K. Tung, Z. Phys. **C52** (1991) 13.

31. I. Hinchliffe, M. Shapiro, Proceedings of the DPF Summer Study on High Energy Physics in the 1990's, June 27 - July 15 (1988) Snowmass, Colorado, p279 (ed. S. Jensen).

32. J. Huth, Proceedings of the workshop on calorimetry for the Superconducting Supercollider, University of Alabama, Tuscaloosa, Alabama, March 13-17, (1989) (eds. R. Donaldson, M. Gilchriese).

33. B. Combridge, C. Maxwell, Nucl. Phys. **B239** (1984) 428;
B. Combridge, J. Kripfganz, J. Ranft, Phys. Lett. **B70** (1977) 234.

34. B. Combridge, C. Maxwell, Nucl. Phys. **B239** (1984) 428.

35. UA1 Collaboration, G. Arnison *et al.* Phys. Lett. **B136** (1984) 294;
UA2 Collaboration, P. Bagnaia *et al.*, Phys. Lett. **B144** (1984) 283.

36. UA1 Collaboration, G. Arnison, *et al.*, Phys. Lett. **B158** (1985) 494.

37. CDF Collaboration, P. Giannetti, Fermilab-Conf-91/137-E, to be published in "Proceedings of Les Rencontres de la Vallée d'Aosta", La Thuile, Italy, March 4-9, 1991;
CDF Collaboration, N. Wainer, Fermilab-Conf-91/138-E, to be published in "Proceedings of the XXVth Rencontres de Moriond", Les Arcs, Savoie, France, March 17-24, 1991;
CDF Collaboration, E. Buckley-Geer, Fermilab-Conf-91/138-E, to be published in "Proceedings of the VIth Conference on Intersections of Particle and Nuclear Physics", Tucson, Arizona, May 24-29, 1991.

38. UA2 Collaboration, J. Appel, *et al.*, Z. Phys. **C30** (1986) 341.

39. Z. Kunszt *et al.*, Phys. Rev. **D40** (1989) 2188;
F. Aversa *et al.*, Nucl. Phys. **B327** (1989) 105; Phys. Rev. Lett. **65** (1990) 401; Z. Phys. **C46** (1990) 253.

40. UA2 Collaboration, J. Alitti *et al.*, Phys. Lett. **B257** (1991) 232.

41. E. Eichten, *et al.*, Phys. Rev. Lett. **50** (1983) 811.

42. CDF Collaboration, F. Abe, *et al.*, Fermilab-Pub-91/231-E, submitted to *Phys. Rev. Lett.*

43. CDF Collaboration, F. Abe *et al.*, Phys. Rev. Lett. **65** (1990) 968.

44. UA1 Collaboration, G. Arnison, *et al.*, Nucl. Phys. **B276** (1986) 253.

45. TASSO Collaboration, M. Althoff *et al.*, Z. Phys. **C22** (1984) 307.

46. CDF Collaboration, R. Harris, Fermilab-Conf-91/236-E, to be published in "Proceedings DPF Meeting", University of Vancouver, Vancouver, British Columbia, Canada, August 18-22, 1991.

47. UA2 Collaboration, J.A. Appel *et al.*, Phys. Lett. **B176** (1986) 239;
UA2 Collaboration, R. Ansari *et al.*, Z. Phys. **C41** (1988) 395;
UA2 Collaboration, J. Alitti *et al.*, Phys. Lett. **B263** (1991) 544.

48. P. Aurenche *et al.*, Phys. Lett. **B140** (1984) 87;
P. Aurenche *et al.*, Nucl. Phys. **B297** (1988) 661;
P. Aurenche *et al.*, Phys. Rev. **D42** (1990) 1440.

49. P. Aurenche *et al.* in "Physics at Fermilab in the 1990's", Breckenridge, Colorado, August 15-24 (1989) 212 (eds. D. Green, H. Lubatti).

50. S. Tkaczyk, W. Stirling, D. Saxon, Proceedings of the HERA workshop, Hamburg, Germany (1987) Vol. I, 265.

51. UA2 Collaboration, J. Alitti *et al.*, Z. Phys. **C49** (1991) 17;
K. Meier, Proceedings of the "8th Topical Workshop on Proton-Antiproton Collider Physics, Castiglione della Pescaia, Italy, September 1-5 (1989).

52. E.S. Abers and B.W. Lee Phys. Rep **9** (1973) 1;
For a nice review see also G. Altarelli in "Proceedings of the NATO Advanced Summer Institute on Particle Physics", Cargèse, France, July 18 - August 4 (1989) 97 (eds. M. Lévy *et al.*).

53. J. Smith, W. van Neerven, J. Vermaseren, Phys. Rev. Lett. **50** (1983) 1738.

54. UA2 Collaboration, J. Alitti *et al.*, Z. Phys. **C47** (1990) 11;
J. Alitti *et al.*, CERN-PPE/91-162, submitted to Phys. Lett. **B**.

55. UA1 Collaboration, C. Albajar *et al.*, Phys. Lett. **B253** (1991) 503.

56. CDF Collaboration, F. Abe *et al.*, Phys. Rev. **D44** (1991) 29.

57. CDF Collaboration, F. Abe *et al.*, Phys. Rev. Lett. **63** (1989) 720.

58. UA1 Collaboration, C. Albajar *et al.*, Phys. Lett. **B185** (1987) 233; Addendum *ibid.* **B191** (1987) 462;
UA1 Collaboration, C. Albajar *et al.*, Phys. Lett. **B185** (1987) 241; Addendum *ibid.* **B191** (1987) 463; Erratum *ibid.* **B197** (1987) 565;
UA1 Collaboration, C. Albajar *et al.*, Phys. Lett. **B198** (1987) 261.

59. UA2 Collaboration, J. Alitti *et al.*, Phys. Lett. **B235** (1990) 363.

60. CDF Collaboration, F. Abe *et al.*, Phys. Rev. **D43** (1991) 2070.

61. G. Altarelli, R.K. Ellis, M. Greco, G. Martinelli, Nucl. Phys. **B246** (1984) 12;
G. Altarelli, R.K. Ellis, G. Martinelli, Z. Phys. **C27** (1985) 617.

62. T. Matsuura, W.L. van Neerven, Z. Phys. **C38** (1988) 623;
T. Matsuura, S. van der Marck, W.L. van Neerven, Phys. Lett. **B211** (1988) 171;
T. Matsuura, S. van der Marck, W.L. van Neerven, Nucl. Phys. **B319** (1989) 570;
R. Hamberg, W.L. van Neerven, T. Matsuura, Nucl. Phys. **B359** (1991) 343.

63. UA1 Collaboration, C. Albajar *et al.*, Z. Phys. **C44** (1989) 15.

64. UA2 Collaboration, J. Alitti *et al.*, Z. Phys. **C52** (1991) 209.

65. J.C. Collins, D.E. Soper, Phys. Rev. **D16** (1977) 2219.

66. CDF Collaboration, F. Abe *et al.*, Phys. Rev. Lett. **67** (1991) 1502.

67. UA2 Collaboration, J. Alitti *et al.*, Z. Phys. **C47** (1990) 523;
J. Alitti *et al.*, CERN-PPE/91-163, submitted to *Phys. Lett.* **B**.

68. CDF Collaboration, F. Abe *et al.*, Phys. Rev. Lett. **66** (1991) 2951.

69. G. Unal, Thèse Université de Paris-Sud, Centre D'Orsay, LAL 91-13 (1991).

70. P. Arnold, R.K. Ellis, M. Reno, Phys. Rev. **D40** (1989) 912;
P. Arnold, M. Reno, Nucl. Phys. **B319** (1989) 37;
Erratum, Nucl. Phys. **B330** (1990) 284;
P. Arnold, R. Kauffman, Nucl. Phys. **B349** (1991) 381.

71. UA2 Collaboration, J. Alitti *et al.*, Phys. Lett. **B241** (1990) 150;
J. Alitti *et al.*, CERN-PPE/91-163, submitted to *Phys. Lett.* **B**.

72. W. Marciano, A. Sirlin, Phys. Rev. **D29** (1984) 945.

73. G. Burgers, F. Jegerlehner, in "Z Physics at LEP I", CERN 89-08, Volume 1, 55 (eds. G. Altarelli, R. Kleiss, C. Verzegnassi).

74. P. Nason, S. Dawson, R.K. Ellis, Nucl. Phys. **B303** (1988) 607, Nucl. Phys. **B327** (1989) 49, Nucl. Phys. **B335** (1990) 260;
G. Altarelli, M. Diemoz, G. Martinelli, P. Nason, Nucl. Phys. **B308** (1988) 724.

75. N. Ellis, "Heavy Flavor Production in UA1", Proceedings of the 7th Topical Workshop on Proton-Antiproton Collider Physics, Fermilab (1988), 661 (eds. R. Raja, A. Tollestrup, J. Yoh).

76. UA1 Collaboration, C. Albajar *et al.*, Z. Phys. **C48** (1990) 1.

77. UA1 Collaboration, C. Albajar *et al.*, Phys. Lett. **B256** (1991) 121.

78. E. Glover, A. Martin, W. Stirling, Z. Phys. **C38** (1988) 473.

79. Paula, J. Franzini, Phys. Rep. **C173** (1989) 1.

80. J. Hagelin, Nucl. Phys. **B193** (1981) 123.

81. L. Wolfenstein, Phys. Rev. Lett. **51** (1983) 1945;
L. Wolfenstein, Nucl. Phys. **B246** (1984) 45.

82. UA1 Collaboration, C. Albajar *et al.*, Phys. Lett. **B262** (1991) 171.

83. A. Breakstone *et al.*, Phys. Lett. **B135** (1984) 510;
UA2 collaboration, M. Banner *et al.*, Phys. Lett. **B122** (1983) 322;
UA5 collaboration, G. Alner *et al.*; Nucl. Phys. **B258** (1985) 505.

84. Argus Collaboration, H. Albrecht *et al.*, Phys. Lett. **B192** (1987) 246;
Cleo Collaboration, A. Bean *et al.*, Phys. Rev. Lett. **58** (1987) 183.

85. Aleph collaboration, D. Decamp *et al.*, Phys. Lett. **B122** (1991) 322,
L3 collaboration, B. Adeva *et al.*, Phys. Lett. **B258** (1991) 505.

86. UA1 Collaboration, C. Albajar *et al.*, Z. Phys. **C48** (1990) 1.

87. UA2 Collaboration, T. Åkesson *et al.*, Z. Phys. **C46** (1990) 179.

88. CDF Collaboration, F. Abe *et al.*, Phys. Rev. Lett. **63** (1989) 720;
CDF Collaboration, F. Abe *et al.*, Phys. Rev. Lett. **63** (1989) 1447;
CDF Collaboration, F. Abe *et al.*, Phys. Rev. **D43** (1991) 664;
CDF Collaboration, F. Abe *et al.*, FERMILAB-PUB-91-280-E, submitted to Phys. Rev. Lett.;
CDF Collaboration, M. Contreras, FERMILAB-CONF-91-294-E, to be published in the Proceedings of the Joint Int. Lepton-Photon Symp. and Europhysics Conference on High Energy Physics, Geneva, Switzerland, Jul 25 - Aug 1 (1991).